

© 2009 Mitrabhanu Sahu

SWITCHING CURRENT DISTRIBUTIONS OF SUPERCONDUCTING NANOWIRES:  
EVIDENCE OF QUANTUM PHASE SLIP EVENTS

BY

MITRABHANU SAHU

B.Sc., Indian Institute of Technology, Kharagpur, 2003  
M.S., University of Illinois at Urbana-Champaign, 2007

DISSERTATION

Submitted in partial fulfillment of the requirements  
for the degree of Doctor of Philosophy in Physics  
in the Graduate College of the  
University of Illinois at Urbana-Champaign, 2009

Urbana, Illinois

Doctoral Committee:

Professor James Eckstein, Chair  
Associate Professor Alexey Bezryadin, Director of Research  
Professor Paul Goldbart  
Professor John Stack

# Abstract

Phase slips are topological fluctuation events that carry the superconducting order-parameter field between distinct current carrying states. Owing to these phase slips low-dimensional superconductors acquire electrical resistance. In quasi-one-dimensional nanowires it is well known that at higher temperatures phase slips occur via the process of thermal barrier-crossing by the order-parameter field. At low temperatures, the general expectation is that phase slips should proceed via quantum tunneling events, which are known as quantum phase slips (QPS). However, experimental observation of QPS is a subject of strong debate and no consensus has been reached so far about the conditions under which QPS occurs. In this study, strong evidence for individual quantum tunneling events undergone by the superconducting order-parameter field in homogeneous nanowires is reported. This is accomplished via measurements of the distribution of switching currents—the high-bias currents at which superconductivity gives way to resistive behavior—whose width exhibits a rather counter-intuitive, monotonic increase with decreasing temperature. A stochastic model of phase slip kinetics which relates the basic phase slip rates to switching rates is outlined. Comparison with this model indicates that the phase predominantly slips via thermal activation at high temperatures but at sufficiently low temperatures switching is caused by individual topological tunneling events of the order-parameter field, i.e., QPS. Importantly, measurements show that in nanowires having larger critical currents quantum fluctuations dominate thermal fluctuations up to higher temperatures. This fact provides strong support for the view that the anomalously high switching rates observed at low temperatures are indeed due to QPS, and not consequences of extraneous noise or hidden inhomogeneity of

the wire. In view of the QPS that they exhibit, superconducting nanowires are important candidates for qubit implementations.

*To my family.*

# Acknowledgments

The work presented in this dissertation could not have been completed without the assistance of many people. Foremost, I would like to thank Alexey Bezryadin, my advisor, who walked me through every step in the process of learning how to conduct experiments, analyze data, and present results. Alexey is an excellent experimentalist and his guidance specific to my work and in general throughout my graduate years have been extremely beneficial. I have learned more from him than he probably knows.

I would like to thank the founding members of the Bezryadin group, Tony Bolinger, Ulas Coskun, David Hopkins and Andrey Rogachev for their help training me in everything from sample fabrication to data analysis. The past and present members of Alexey's research group have provided a continuous source of ideas, answers, and encouragement while keeping the atmosphere in the lab very open and enjoyable. These include Thomas Aref, Rob Dinsmore, Matthew Brenner, Jaseung Ku, Mikas Remeika, Bob Colby, C. J. Lo, Anil Nandyala, and Hisashi Kajiura. I am especially appreciative of the help and guidance I received from Myung-Ho Bae, a postdoctoral fellow in our group, for measurements and especially for the work on high- $T_c$  Josephson junctions.

I would like to thank Paul Goldbart and his students, in particular David Pekker, for their inputs and discussions. They, second to my advisor, have helped me understand the most about the underlying physics of my experiments.

Much of the nanowire fabrication was performed in the Microfabrication and Crystal Growth Facility and class 100 cleanroom of the Materials Research Laboratory. I thank Tony Banks for all of his hard work in maintaining this excellent resource and for his technical

advice). I am also grateful to Vania Petrova and Mike Marshall of the Center for Materials Microanalysis for instrument training and assistance.

Special thanks to Neet Priya Bajwa for her patience in proof reading my thesis and giving very insightful comments to improve the presentation. I would like to thank Jaseung Ku for his help in formatting the thesis in  $\text{\LaTeX}$ . I would like to thank my family and friends for always believing that I would succeed. Even though I cannot name them all here, I will always cherish their support and the time spent with them.

I would like to thank the University of Illinois Graduate College for awarding me a Dissertation Completion Fellowship, which allowed me to focus more on my research project. This work was supported by the U.S. Department of Energy under Grant No. DE-FG0207ER46453. This work was carried out in part in the Frederick Seitz Materials Research Laboratory Central Facilities, University of Illinois, which are partially supported by the U.S. Department of Energy under Grant Nos. DE-FG0207ER46453 and DE-FG0207ER46471.

# Table of Contents

<b>List of Tables</b> . . . . .	<b>ix</b>
<b>List of Figures</b> . . . . .	<b>x</b>
<b>Chapter 1 Introduction</b> . . . . .	<b>1</b>
<b>Chapter 2 Basics of superconductivity in one dimension</b> . . . . .	<b>5</b>
2.1 Phase slip in one dimension . . . . .	5
2.2 Free energy barrier for a phase slip . . . . .	9
2.3 Little's fit . . . . .	15
2.4 LAMH fit . . . . .	16
2.5 Comparisons with experiments . . . . .	21
2.6 Quantum phase slips . . . . .	24
<b>Chapter 3 Fabrication and measurements of superconducting nanowires</b>	<b>34</b>
3.1 Fabrication of superconducting nanowires on top of carbon nanotubes . . . . .	35
3.1.1 Preparation of the substrate . . . . .	35
3.1.2 Deposition of fluorinated single walled carbon nanotubes . . . . .	37
3.1.3 Sputtering of superconducting material . . . . .	39
3.1.4 Scanning electron microscopy . . . . .	41
3.1.5 Photolithography and etching . . . . .	43
3.2 Measurement of superconducting nanowires . . . . .	45
3.2.1 Mounting the sample . . . . .	45
3.2.2 Cryostats . . . . .	46
3.2.3 Filtering system of $^3\text{He}$ measurement setup . . . . .	48
3.2.4 Transport Measurements . . . . .	50
<b>Chapter 4 Low-bias measurements of superconducting nanowires</b> . . . . .	<b>53</b>
4.1 Resistance vs. temperature $R(T)$ curves . . . . .	53
4.2 Comparison with Little's and LAMH fits . . . . .	57
<b>Chapter 5 Switching current measurements of superconducting nanowires</b>	<b>61</b>
5.1 High-bias $V(I)$ measurements . . . . .	61
5.2 Stochasticity of switching currents . . . . .	64
5.3 Switching current distribution measurements . . . . .	66

5.4	Standard deviation of switching current distributions . . . . .	73
5.5	Switching rates from switching current distributions . . . . .	75
5.6	Dynamics of switching in superconducting nanowires . . . . .	80
5.7	Quantum phase slip and single phase-slip regime . . . . .	84
5.8	Details of the stochastic overheating model . . . . .	93
5.8.1	Model for heating by phase slips . . . . .	93
5.8.2	Input functions and parameters . . . . .	101
5.8.3	Comparison with experimental data . . . . .	105
<b>Chapter 6</b>	<b>Multiple-retrapping process in high-<math>T_c</math> Josephson junctions . . . . .</b>	<b>116</b>
6.1	Introduction . . . . .	116
6.2	Experiments . . . . .	118
6.3	Results and discussion . . . . .	120
6.4	Summary . . . . .	127
<b>Appendix A</b>	<b>MQT in high-<math>T_C</math> intrinsic Josephson junctions . . . . .</b>	<b>129</b>
<b>References</b>	<b>. . . . .</b>	<b>133</b>
<b>Author's Biography</b>	<b>. . . . .</b>	<b>139</b>

# List of Tables

3.1	Properties of MeGe: Measured and derived physical parameters of MoGe . . .	40
5.1	Nanowire sample parameters for the five measured MoGe wires. . . . .	93
6.1	Fitting parameters for the switching events for selected temperatures . . . .	127

# List of Figures

2.1	Little’s phase slip diagram from his paper . . . . .	7
2.2	Depiction of a phase slip event . . . . .	8
2.3	Gibbs free-energy barrier . . . . .	18
2.4	Data from Lukens <i>et al.</i> and Newbower <i>et al.</i> . . . . .	21
2.5	Data from Rogachev <i>et al.</i> and Chu <i>et al.</i> with TAPS fits . . . . .	23
2.6	Data from Rogachev <i>et al.</i> and Bollinger <i>et al.</i> . . . . .	24
2.7	Data from Giordano <i>et al.</i> with fits to his model of MQT . . . . .	25
2.8	Data from Lau <i>et al.</i> with fits to the Giordano’s model . . . . .	26
2.9	Data from Zgirski <i>et al.</i> for Al wire . . . . .	29
2.10	Data from Zgirski <i>et al.</i> for Al wire with fit to GZ model . . . . .	30
2.11	Data from Zgirski <i>et al.</i> for Al wire with progressive reduction of diameter . . . . .	31
2.12	Data from Altomare <i>et al.</i> with fits to Giordano’s model . . . . .	33
3.1	Preparation of the substrate . . . . .	36
3.2	Deposition of Fluorinated single walled carbon nanotube . . . . .	38
3.3	Deposition of metal . . . . .	41
3.4	Scanning Electron Microscope (SEM) images of nanowires . . . . .	42
3.5	Photolithography process . . . . .	44
3.6	The shape of the Cr mask used in photolithography . . . . .	45
3.7	Attenuation of high frequency signal in the $^3\text{He}$ setup . . . . .	49
3.8	Schematic of the measurement setup for transport measurement of nanowires . . . . .	51
4.1	$R(T)$ curve for a MoGe nanowire sample . . . . .	54
4.2	$R(T)$ curves for 9 different MoGe nanowires representing SIT . . . . .	56
4.3	Little’s fit to the $R-T$ data for a nanowire . . . . .	57
4.4	LAMH fit to the $R-T$ data for a nanowire . . . . .	59
5.1	$V(I)$ curves for a MoGe nanowire . . . . .	62
5.2	$V(I)$ curves for several temperatures illustrating the “voltage tails” . . . . .	63
5.3	$I_{SW}$ and $I_R$ measured as the sample temperature is decreased . . . . .	65
5.4	Switching current distribution data for three different temperatures . . . . .	67
5.5	Switching current distributions for wire S1 . . . . .	68
5.6	Switching current distributions for wire S2 . . . . .	70
5.7	Switching current distributions for wire S3 . . . . .	71
5.8	Switching current distributions for wire S4 . . . . .	72

5.9	Switching current distributions for wire S5 . . . . .	73
5.10	Standard deviation of switching current distributions for five samples . . . . .	74
5.11	Switching current distribution to rate conversion . . . . .	76
5.12	Switching rates for wire S1 . . . . .	77
5.13	Switching rates for wire S2 . . . . .	78
5.14	Switching rates for wire S3 . . . . .	78
5.15	Switching rates for wire S4 . . . . .	79
5.16	Switching rates for wire S5 . . . . .	79
5.17	Simulated “temperature bumps” in the nanowire due to phase-slips events . . . . .	81
5.18	Switching rates and fit to the stochastic overheating model . . . . .	82
5.19	Single QPS regime . . . . .	85
5.20	Effective quantum temperature . . . . .	87
5.21	Different attempt frequency for TAPS . . . . .	89
5.22	Mean switching current . . . . .	90
5.23	High-bias $V(I)$ data and TAPS fit . . . . .	91
5.24	Sketch of the overheating model . . . . .	96
5.25	Simulated $I$ - $V$ hysteresis loops . . . . .	106
5.26	Comparison of switching current distributions with the overheating model . . . . .	108
5.27	Hierarchy of critical and switching currents . . . . .	109
5.28	Comparison of standard deviation with the overheating model . . . . .	110
5.29	Mean switching rates and fits . . . . .	111
5.30	Single phase slip induced switch regime . . . . .	113
6.1	$R$ vs $T$ curve of the sample stack . . . . .	119
6.2	Switching current distributions and switching rates . . . . .	121
6.3	Dependence of switching current distributions on impedance . . . . .	124
A.1	Standard deviation for switching current for two samples . . . . .	130
A.2	Switching rates obtained from the switching current distributions . . . . .	131
A.3	The escape temperature $T_{esc}$ obtained at various bath temperatures . . . . .	132

# Chapter 1

## Introduction

Quantum phenomena involving systems far larger than individual atoms are one of the most exciting fields of modern physics. Initiated by Leggett more than twenty-five years ago, the field of macroscopic quantum tunnelling (MQT) [1, 2, 3] has seen widespread development. Important realizations of this being furnished, for instance, by MQT of the phase in Josephson junctions [4, 5, 6, 7] and MQT of the magnetization in magnetic nanoparticles [8]. Martinis, Devoret and Clarke in 1987 showed that a macroscopic object can behave as a single quantum particle [5]. They used a microwave technique and showed that a micron sized superconducting device possesses a discrete energy spectrum in addition to showing MQT. More recently, the breakthrough recognition of the potential advantages of quantum-based computational methods has initiated the search for viable implementations of qubits, several of which are rooted in MQT in superconducting systems. In particular, it has been recently proposed by Mooij, Harmans and Nazarov that superconducting nanowires (SCNWs) could provide a valuable setting for realizing qubits [9]. In this case, the essential behavior needed of SCNWs is that they undergo quantum phase slip (QPS) [10], i.e., topological quantum fluctuations of the superconducting order-parameter field via which tunneling occurs between current-carrying states. At sufficiently low temperatures, QPS replaces the thermally activated phase slip (TAPS) [11] dominating at higher temperatures. It has also been proposed that QPS in nanowires could allow to build a current standard, and thus could play a useful role in aspects of metrology [12]. Additionally, QPS are believed to provide the pivotal processes underpinning the superconductor-insulator transition observed in nanowires [13, 14, 15, 16, 17]. Observations of QPS have been reported previously on wires having high

normal resistance (i.e.,  $R_N > R_Q$ , where  $R_Q = h/4e^2 \approx 6,450 \Omega$ ) via low-bias resistance ( $R$ ) vs. temperature ( $T$ ) measurements [10, 18]. Yet, low-bias measurements on short wires with normal resistance  $R_N < R_Q$  have been unable to reveal QPS [19, 20, 21, 14]. Also, it has been suggested that some results ascribed to QPS could in fact have originated in inhomogeneity of the nanowires. Thus, no consensus exists about the conditions under which QPS occur, and qualitatively new evidence for QPS remains highly desirable.

In this study, switching current distribution measurements of superconducting  $\text{Mo}_{79}\text{Ge}_{21}$  nanowires are presented [22]. This switching current is defined as the high-bias current at which the resistance exhibits a sharp jump from a very small value to a much larger one, close to  $R_N$ . A monotonic increase in the width of the distribution as the temperature decreases is observed. These findings are analyzed in the light of a new theoretical model [23], which incorporates Joule-heating [24] caused by stochastically-occurring phase slips. The switching rates yielded by the model are quantitatively consistent with the data, over the entire range of temperatures at which measurements were performed (i.e., 0.3 K to 2.2 K for sample S1), using both QPS and thermally-activated phase slip [11, 25, 26] (TAPS) processes. By contrast, if only TAPSs are included, the model fails to give qualitative agreement with the observed switching-rate behavior below 1.2 K. Thus in the SCNWs studied, the phase of the superconducting order-parameter field slips predominantly via thermal activation at high temperatures; however, at temperatures below 1.2 K it is quantum tunneling that dominates the phase-slip rate. It is especially noteworthy that at even lower temperatures (i.e., below 0.7 K) both the data in the present study and the model suggest that individual phase slips are, by themselves, capable of causing switching to the resistive state. Thus, in this regime, one has the capability of exploring the physics of *single quantum phase-slip events*. Furthermore, strong effects of QPS at high bias currents were observed even in wires with  $R_N < R_Q$ . Another crucial fact is that the observed quantum behavior is more pronounced in wires with larger critical currents. This fact allows to rule out the possibility that the observed behavior is caused by noise or wire inhomogeneity.

In Chapter 2, I will discuss the physics of phase slip phenomenon and derivation of an expression for the associated energy barrier for a phase slip event. This will be followed by discussions on models of TAPS by Little [11] and Langer-Ambegaokar [25] and McCumber-Halperin [26] (LAMH) and its experimental verification done by several groups. This chapter will conclude with discussion on theoretical models for QPS and outlining experimental work that claims observation of QPS.

In chapter 3, the method of molecular templating to fabricate the nanowires [13] used for this study is discussed. This method employs a suspended linear molecule as a template subjected to a thin layer of metal deposition to produce a *quasi*-one-dimensional system. For this study, using fluorinated single walled nanotubes (FSWNTs) as templates, homogeneous  $\text{Mo}_{79}\text{Ge}_{21}$  superconducting nanowires are fabricated. Various setups used to perform the measurements are also discussed. As these measurements are very sensitive to extraneous noise, the details of the filtering system that were implemented are provided.

In chapter 4, I will discuss low-bias  $R(T)$  measurements performed on single nanowire samples. By low-bias measurements it is meant that the applied currents are much smaller than the thermodynamic critical current, such that the current-voltage ( $V(I)$ ) characteristics show Ohmic behavior. It will be also shown that for the superconducting wires the resistive transitions can be well explained by theory of TAPS. To obtain the fits, two models of TAPS will be used, namely, Little's fit and Langer-Ambegaokar and McCumber-Halperin (LAMH) fit. The LAMH model is based on the assumption that the wire is homogeneous (i.e., free from granularity). Agreement of the resistance measured in an experiment with that predicted in LAMH model would thus indicate homogeneity of the measured wire. For the insulating wires the  $R(T)$  data will be shown for a few measured samples.

Switching current distributions provide a new method to overcome the difficulty in probing the superconductivity in nanowires at low temperatures associated with the small value of the linear resistance at low temperatures. The performed switching current measurements will be discussed in chapter 5. In these experiments, the current through the nanowire is

ramped up and down in time, via a triangular or sinusoidal protocol. As the current is ramped up, the state of the wire switches from superconductive to resistive (i.e., normal), doing so at a value of the current that is smaller than the depairing (i.e., equilibrium) critical current; and on ramping the current down, the state gets retrapped into a superconductive state, but at a value of current smaller than the current at which switching occurred. Hysteretic behavior such as this reflects the underlying bistability of the superconducting nanowire. By repeatedly ramping the current up and then down, for thousand of cycles at each temperature, thousands of values of switching and retrapping current that constitute distributions are generated. It is found that the retrapping current is characterized by an extremely sharp distribution, i.e., it does not vary much from run to run. In contrast, the switching current *does* vary from run to run, and thus yields a distribution. These widths of the distributions is found to increase with decrease in temperature. A stochastic overheating model is developed to explain this behavior. The main finding of this work is that below a crossover temperature  $T^*$  the fluctuations are dominated by QPS and at sufficiently low temperatures, every single QPS causes switching in the wire.

Finally in chapter 6, measurements of switching current distribution from a phase diffusion branch (PDB) to a quasiparticle tunneling branch (QTB) as a function of temperature in a cuprate-based intrinsic Josephson junction is reported. Contrary to the thermal-activation model, the width of the distributions increases and the corresponding switching rate shows a nonlinear behavior with a negative curvature in a semi-logarithmic scale with decreasing temperature, down to 1.5 K. Based on the multiple retrapping model, it is quantitatively demonstrated that the frequency-dependent junction quality factor, representing the energy dissipation in a phase diffusion regime, determines the observed temperature dependence of the widths of the distributions and the switching rates. It is also shown that a retrapping process from the QTB to the PDB is related to the low-frequency limit damping.

# Chapter 2

## Basics of superconductivity in one dimension

One interesting property of superconductivity in quasi-one-dimensional system is the phenomenon of phase slips. Phase slip processes are responsible for resistance in superconducting nanowires. At high temperatures (but below the transition temperature  $T_C$ ) this resistance is caused due to thermally activated phase slips (TAPS), in which the system makes transition across a potential barrier between two different metastable states. At sufficiently low temperatures the general expectation is that the system would tunnel through the barrier between two metastable states, constituting a quantum phase slip event (QPS). Until now there are several experimental observation of TAPS which is agreement with the predictions theoretical models. But observation of QPS remains a subject of strong debate.

In this chapter I will discuss the physics of phase-slip phenomenon and give derivation of an expression for the associated energy barrier for a phase slip event. This will be followed by discussions on models of TAPS and its experimental verification. This chapter will conclude with a discussion of theoretical models for QPS and by outlining experimental work that claims observation of QPS.

### 2.1 Phase slip in one dimension

According to the phenomenological model of superconductivity proposed by Ginzburg and Landau (GL) in 1950, a spontaneous symmetry breaking occurs at the superconducting

transition and the superconducting state emerges, described by the complex order parameter,

$$\psi = \psi_0 e^{i\phi} \quad (2.1)$$

where,  $\psi_0$  is the magnitude and  $\phi$  is the phase of the order parameter. The density of the superconducting electrons is given by,  $n_s = |\psi|^2 = \psi_0^2$ , which is non-zero, below the superconducting transition temperature  $T_C$ . The GL free energy functional is

$$F[\psi] = \int d^3r \left[ \alpha |\psi|^2 + \frac{\beta}{2} |\psi|^4 + \frac{\hbar^2}{2m} |\nabla\psi - i \frac{e^* A}{\hbar c} \psi|^2 + \frac{H^2}{8\pi} \right] \quad (2.2)$$

where  $\alpha$  strongly depends upon the temperature as,  $\alpha \propto (T - T_C)$  (Here,  $A$  is the magnetic vector potential). This parameter  $\alpha$  changes sign as the temperature changes through  $T_C$ , giving rise to superconductivity below  $T_C$ . In other words, by definition  $T_C$  is the highest temperature at which  $|\psi|^2 \neq 0$  gives a lower free energy than  $|\psi|^2 = 0$ .

For a superconducting nanowire, in the absence of magnetic field, the supercurrent is driven by phase gradients, with a velocity given by

$$v_s = \frac{\hbar}{2m} \nabla\phi, \quad (2.3)$$

where  $m$  is the mass of the electrons. The supercurrent through a wire of cross section  $A$  is

$$\begin{aligned} I_s &= J_s A \\ &= 2en_s v_s A \\ &= \frac{e\hbar}{2m} \psi_0^2 \nabla\phi A \end{aligned} \quad (2.4)$$

Due to conservation of current we also have that  $|\psi_0|^2 \nabla\phi = \text{constant}$ .

The process of phase slip was first introduced by Little in 1967 [11]. This theory was developed in order to understand the mechanism of the supercurrent decay in thin wires

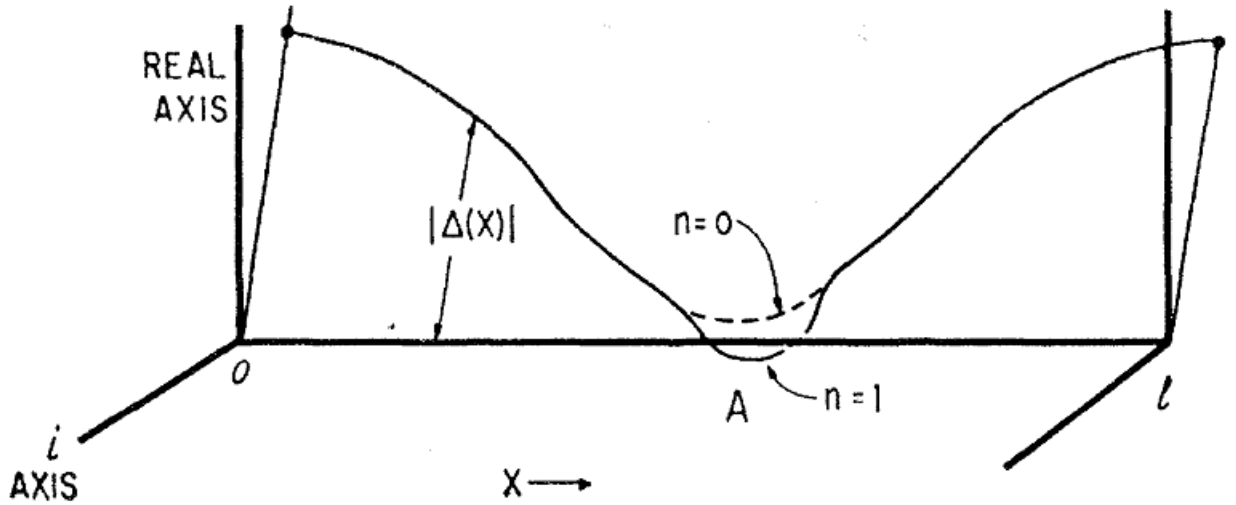


Figure 2.1: Little's phase slip diagram from his paper [11]. The superconducting order parameter is plotted as a function of position along a superconducting ring. The two possible configurations shown correspond to (i) order parameter  $\psi_0(x)$ , with no vortex present in the ring ( $n = 0$ ), (ii) order parameter  $\psi_1(x)$ , with one vortex present in the ring ( $n = 1$ ). Near the point A,  $\psi_1(x)$  makes an excursion around zero on the Argand plane, while  $\psi_0(x)$  does not. The transition from  $n = 1$  to  $n = 0$  constitutes a phase slip event. This event can be considered a vortex, with its normal core, passing across the wire. The transition between the  $n = 1$  and  $n = 0$  state can only occur if the order parameter reaches zero somewhere along the wire.

and to justify Little's earlier proposal of a superconducting macromolecule [27]. Little's argument is based on the assumption that the superconducting order parameter is defined locally as well as globally in a thin wire. The local amplitude of order parameter is subject to thermal fluctuations. Each time the order parameter becomes zero somewhere along the wire due to fluctuation, the "order parameter spiral", representing the supercurrent in the wire can unwind, as shown in Fig. 2.1. In the graph shown in Fig. 2.1 the complex order parameter  $\psi = |\psi(x)|e^{i\phi(x)}$  of a thin wire ring is plotted as a function of the position  $x$  along the ring. Two possible configurations,  $\psi_0$  (with no vortex,  $n = 0$ ) and  $\psi_1$  (with one vortex,  $n = 1$ ), are shown. As shown in the Fig. 2.1,  $\psi_1$  makes an excursion around zero in the Argand plane near the point A while  $\psi_0$  does not make such an excursion. The state  $\psi_1$  corresponds to a phase difference of  $2\pi$  along the ring and leads a nonzero supercurrent.

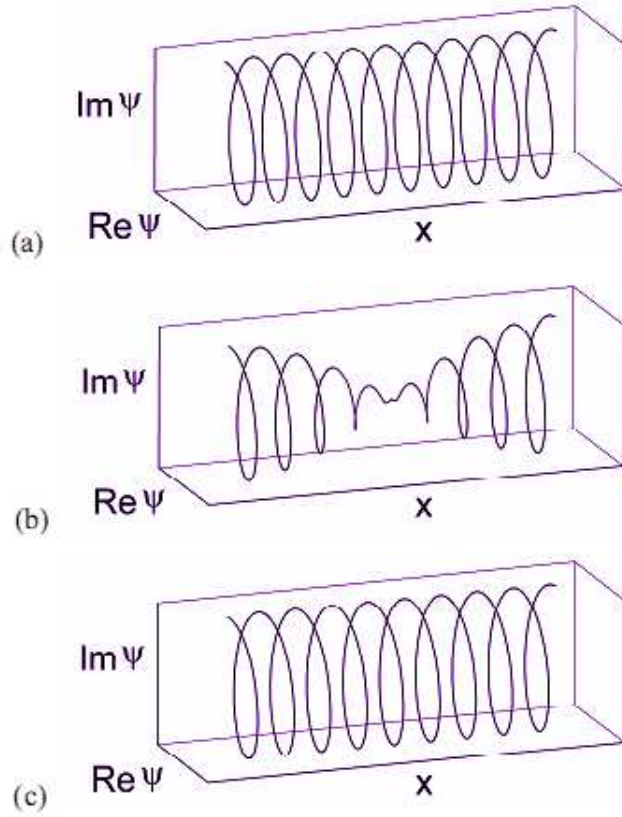


Figure 2.2: A phase slip event (a) Before the phase slip there are ten helical turns along the wire . (b) The order parameter goes to zero at some point along the wire, allowing the phase to slip by  $2\pi$ . (c) After the phase slip a helical turn has been subtracted by one. Picture taken from Ref. [29]

The state  $\psi_0$  , on the other hand, corresponds to zero phase difference and corresponds to zero net supercurrent. The transition from  $\psi_1$  to  $\psi_0$  constitutes a phase slip event that topologically requires the order parameter curve to cross the  $x$ -axis. Precisely the condition  $\psi = 0$  needs to be satisfied at some point in time along the wire. Hence, a phase slip event is equivalent to vortex core passing across the nanowire [28].

After each phase slip event, the phase difference between the ends of the wire can only change by an integer multiple of  $2\pi$  (see Fig. 2.2). This type of phase slippage by  $2\pi n$ , unlike phase change by any other value, does not require a voltage to be applied to the leads, since their phases are defined by modulo  $2\pi$ . The phase difference between the leads is defined by the number of times the order parameter goes around zero on the Argand plane. As this

phase revolution is reduced by one loop, the phase difference is reduced by  $2\pi$ .

Within Little's model, a finite resistance occurs at constant voltage bias, according to the following explanation. The voltage applied to the ends of the wires increases the phase difference between the wire, and thus tends to increase the supercurrent (as  $I_s \propto \nabla\phi$ ). Simultaneously, the phase slips occurring stochastically at any point along the wire tend to decrease the supercurrent. A dynamic non-equilibrium steady state is reached at a supercurrent value that is linearly dependent on the applied voltage (for small voltages). This leads to a finite resistance. By the processes of phase slips the energy supplied at a rate  $IV$  is dissipated as heat rather than converted into kinetic energy of the supercurrent, which would otherwise soon exceed the condensation energy [30].

Thus, as discussed above, the process of phase slip leads to dissipation and the wire acquires a non-zero electrical resistance. This resistance is defined by an Arrhenius type equation with temperature dependent energy barrier. This barrier is determined by the condensation energy required to locally suppress the order parameter to zero. The minimum energy barrier (the 'saddle' point) corresponds to fluctuations in which the order parameter is suppressed in wire segments with lengths of the order of coherence length  $\xi(T)$ . Hence TAPS causes nanowires to remain resistive at any nonzero temperature. In the following section the expression for the energy barrier for phase slip processes in a nanowire will be derived.

## 2.2 Free energy barrier for a phase slip

The calculation of the energy barrier for phase slips was done by Langer and Ambegaokar (LA) [25]. Using the time dependent GL theory, they found that the value of minimum free energy barrier that separates two stationary states of a one-dimensional superconductor that

differ in number of turns in the helix by one is

$$\Delta F(T) = \frac{8\sqrt{2}}{3} \frac{H_C^2(T)}{8\pi} A \xi(T), \quad (2.5)$$

where  $H_C$  is the thermodynamical critical field,  $A$  is the cross sectional area of the wire and  $\xi$  is the GL coherence length. This result can be understood reasonably by considering the condensation energy of minimum volume of the wire that is normal during a phase slip process. The minimum volume over which the phase slip can occur is  $\sim \xi(T)A$  and the condensation energy involved is  $\sim \xi(T)AH_C^2(T)/8\pi$ . Here, we have assumed that the diameter of the wire is smaller than (or of the order of) the coherence length  $\xi$  such that entire cross section of the wire is normal during a phase slip process. Near  $T_C$ , we also have

$$H_C(T) \propto \left(1 - \frac{T}{T_C}\right), \quad (2.6)$$

$$\xi(T) \propto \left(1 - \frac{T}{T_C}\right)^{-1/2}. \quad (2.7)$$

From Eq. 2.5 this leads to temperature dependence of the barrier as

$$\Delta F(T) = \Delta F(0) \left(1 - \frac{T}{T_C}\right)^{3/2} \quad (2.8)$$

Our goal now is to derive an expression for energy barrier that can be used to compare with the experimental data using the fitting parameters  $T_C$  and  $\xi(0)$ . This way we have two fitting parameters [ $T_C$  and  $\xi(0)$ ] instead of three fitting parameters [ $T_C$ ,  $\xi(0)$  and  $H_C(0)$ ]. To do this we begin with  $\Delta F(0)$  as

$$\Delta F(0) = \frac{8\sqrt{2}}{3} \frac{H_C^2(0)}{8\pi} A \xi(0), \quad (2.9)$$

and eliminate  $H_C^2(0)$ . This can be done by recognizing that GL coherence length is defined

by

$$\xi^2(T) = \frac{\hbar^2}{4m|\alpha(T)|}, \quad (2.10)$$

where

$$\alpha(T) = -\frac{2e^2}{mc^2} H_C^2(T) \lambda_{\text{eff}}^2(T). \quad (2.11)$$

$\lambda_{\text{eff}}$  is the effective penetration depth and  $c$  is the speed of light. We have for  $\xi(0)$

$$\begin{aligned} \xi^2(0) &= \frac{\hbar^2}{4m \frac{2e^2}{mc^2} H_C^2(0) \lambda_{\text{eff}}^2(0)} \\ &= \frac{\hbar^2 c^2}{8e^2 H_C^2(0) \lambda_{\text{eff}}^2(0)}. \end{aligned} \quad (2.12)$$

Thus we now have,

$$H_C^2(0) = \frac{\hbar^2 c^2}{8e^2 \xi^2(0) \lambda_{\text{eff}}^2(0)}. \quad (2.13)$$

Using this to eliminate  $H_C(0)$  from Eq. 2.9 we get

$$\begin{aligned} \Delta F(0) &= \frac{8\sqrt{2}}{3} \frac{H_C^2(0)}{8\pi} A \xi(0) \\ &= \frac{8\sqrt{2}}{3} \frac{1}{8\pi} \frac{\hbar^2 c^2}{8e^2 \xi^2(0) \lambda_{\text{eff}}^2(0)} A \xi(0). \end{aligned} \quad (2.14)$$

The next step is to eliminate the effective penetration depth term in the dirty limit, which is valid for  $M_{0.79}Ge_{0.21}$  since  $3\text{\AA} \approx l \ll \lambda_L(0) \approx 18.5 \text{ nm}$  (where  $\lambda_L$  is the London penetration depth). We thus have

$$\lambda_{\text{eff}}^2(T) = \lambda_L^2(T) \frac{\xi_0}{J(0, T) l} \quad (2.15)$$

where  $\xi_0$  is the Pippard coherence length and  $l$  is the mean free path. Thus, we have

$$\frac{1}{\lambda_{\text{eff}}^2(0)} = \frac{1}{\lambda_L^2(0)} \frac{J(0, 0) l}{\xi_0} = \frac{1}{\lambda_L^2(0)} \frac{l}{\xi_0} \quad (2.16)$$

where we have used for zero temperature,  $J(0,0) = 1$ . Now we would like to eliminate the effective penetration depth, so  $\Delta F(0)$  reduces to

$$\begin{aligned}
\Delta F(0) &= \frac{8\sqrt{2}}{3} \frac{1}{8\pi} \frac{\hbar^2 c^2}{8e^2 \xi^2(0) \lambda_{\text{eff}}^2(0)} A \xi(0) \\
&= \frac{\sqrt{2}}{3} \frac{A}{8\pi} \frac{\hbar^2 c^2}{e^2 \xi(0) \lambda_{\text{eff}}^2(0)} \\
&= \frac{\sqrt{2}}{3} \frac{A}{8\pi} \frac{\hbar^2 c^2}{e^2 \xi(0)} \frac{1}{\lambda_L^2(0)} \frac{l}{\xi_0}.
\end{aligned} \tag{2.17}$$

In the next step we will eliminate the London penetration depth, given by

$$\lambda_L^2(T) = \frac{mc^2}{4\pi n_s(T) e^2}, \tag{2.18}$$

so we get,

$$\frac{1}{\lambda_L^2(0)} = \frac{4\pi n_s(0) e^2}{mc^2} = \frac{4\pi n e^2}{mc^2}, \tag{2.19}$$

where  $n$  is the density of the normal electrons. At zero temperature, almost all the electrons are paired. Hence we are able to use  $n = n_s(0)$ . The free energy barrier now becomes,

$$\begin{aligned}
\Delta F(0) &= \frac{\sqrt{2}}{3} \frac{A}{8\pi} \frac{\hbar^2 c^2}{e^2 \xi(0)} \frac{1}{\lambda_L^2(0)} \frac{l}{\xi_0} \\
&= \frac{\sqrt{2}}{3} \frac{A}{8\pi} \frac{\hbar^2 c^2}{e^2 \xi(0)} \frac{l}{\xi_0} \frac{4\pi n e^2}{mc^2} \\
&= \frac{\sqrt{2}}{3} \frac{A}{2} \frac{\hbar^2}{e^2 \xi(0)} \frac{l}{\xi_0} \frac{n e^2}{m}
\end{aligned} \tag{2.20}$$

From the microscopic BCS theory,

$$\xi_0 = \frac{\hbar v_F}{\pi \Delta(0)}, \tag{2.21}$$

where  $v_F$  is the Fermi velocity and  $\Delta(0)$  is the superconducting gap at zero temperature, so

$$\begin{aligned}
\Delta F(0) &= \frac{\sqrt{2} A}{3} \frac{\hbar^2}{2 e^2 \xi(0)} \frac{l}{\xi_0} \frac{ne^2}{m} \\
&= \frac{\sqrt{2} A}{3} \frac{\hbar^2}{2 e^2 \xi(0)} l \frac{ne^2}{m} \frac{\pi \Delta(0)}{\hbar v_F} \\
&= \frac{\sqrt{2} \pi \hbar}{3} \frac{A}{2 e^2 \xi(0)} \frac{ne^2 l}{m v_F} \Delta(0).
\end{aligned} \tag{2.22}$$

From Drude theory, the force on a normal metal is modeled as

$$m \frac{dv}{dt} = eE - \frac{mv}{\tau} \tag{2.23}$$

where  $v$  is the electron velocity,  $E$  is the electric field and  $\tau$  is the elastic scattering time. In the steady state,  $dv/dt = 0$ , so we have

$$eE = \frac{mv}{\tau} \tag{2.24}$$

from which we get Ohm's law,

$$j = nev = \frac{ne^2 \tau}{m} E = \sigma E. \tag{2.25}$$

From conductivity we get the resistivity  $\rho$ :

$$\sigma = \frac{ne^2 \tau}{m} = \frac{ne^2 l}{m v_F} = \frac{1}{\rho}, \tag{2.26}$$

and using this in Eq. 2.22 we arrive at

$$\begin{aligned}
\Delta F(0) &= \frac{\sqrt{2} \pi \hbar}{3} \frac{A}{2 e^2 \xi(0)} \frac{ne^2 l}{m v_F} \Delta(0) \\
&= \frac{\sqrt{2} \pi \hbar}{3} \frac{A}{2 e^2 \xi(0)} \frac{1}{\rho} \Delta(0).
\end{aligned} \tag{2.27}$$

The BCS gap at zero temperature is given by  $\Delta(0) \cong 1.76k_B T_C$ . Thus, we get

$$\begin{aligned}\Delta F(0) &= \frac{\sqrt{2}}{3} \frac{\pi \hbar}{2e^2} \frac{A}{\xi(0)} \frac{1}{\rho} 1.76k_B T_C \\ &= 0.83 \frac{R_Q}{R_N} \frac{L}{\xi(0)} k_B T_C,\end{aligned}\tag{2.28}$$

where, the quantum resistance of Cooper pairs  $R_Q = \pi \hbar / 2e^2 = h / 4e^2$ , and the normal-state resistance of the wire is  $R_N = \rho L / A$  with length of the wire  $L$ . Now we define a parameter  $c$  which allows us to express the free energy barrier as a function of temperature given as

$$\begin{aligned}\delta F(T) &= \Delta F(0) \left(1 - \frac{T}{T_C}\right)^{3/2} \\ &= ck_B T_C \left(1 - \frac{T}{T_C}\right)^{3/2}\end{aligned}\tag{2.29}$$

where

$$c \equiv 0.83 \frac{R_Q}{R_N} \frac{L}{\xi(0)}.\tag{2.30}$$

Before concluding this section, I briefly discuss the solution of the order parameter for a phase slip in one-dimension. To find the exact value of the phase slip barrier we need to know the ‘‘shape’’ of the order parameter near the phase slip point [31]. In the limit of zero bias current (which is also good for low bias currents) and for zero magnetic field, the solution for the order parameter corresponding to a phase slip can be written as  $y_{PS}(x) = \tanh[(x - x_0) / \sqrt{2}\xi(T)]$ . It can be easily verified that this solution satisfies the normalized equation,

$$\xi^2(T) \frac{d^2 y}{dx^2} + y - y^3 = 0,\tag{2.31}$$

where  $\xi(T) = \hbar^2 / 4m|\alpha(T)|$  with  $\xi(T)$  being the GL coherence length,  $y = \psi / \psi_\infty$  is the normalized order parameter with  $\psi_\infty^2 = -\alpha / \beta > 0$ , and  $x_0$  is the position of the phase slip, at which order parameter goes to zero. Around the phase-slip point the order parameter reaches the equilibrium value  $y_{EQ} = 1$  over a length scale comparable to the coherence

length  $\xi(T)$ . From these solutions one can compute the barrier for a phase slip  $\Delta F(T)$ , by computing the difference between the GL free energy corresponding to  $y_{PS}(x)$  and  $y_{EQ} = 1$ . Thus, one can write,

$$\Delta F(T) = F[y_{PS}(x)] - F[y_{EQ}] \quad (2.32)$$

where  $F$  is the functional describing the GL free energy as in Eq. 2.2. Thus, it is possible to find the barrier for a phase slip simply by comparing exact static solutions of GL equation (one homogeneous and one going to zero at the position of phase slip) without referring to any equation describing the *dynamics* of the condensate.

## 2.3 Little's fit

According to Little's fit, the resistance of a nanowire is given as,

$$R_{Little}(T) = R_N \exp\left(-\frac{\Delta F(T)}{k_B T}\right) \quad (2.33)$$

which is based on the Arrhenius rate law. Here,  $R_N$  is the normal-state resistance of the wire,  $k_B$  is the Boltzmann's constant,  $T$  is the temperature, and  $\Delta F(T)$  is the barrier for phase slip, which is a function of temperature derived in the previous section. At temperatures close to  $T_C$  this expression is not accurate, as it gives  $R(T_C) = R_N$ , whereas the actual wire resistance should be less than  $R_N$ , due to superconducting fluctuations [28]. Based on Little's hypothesis [11], we assume that each segment of the wire can only exist in one of the two distinct states: superconducting, i.e., the zero resistance state that occurs between phase slip events, and the normal state that is realized during each phase slip event in the considered segment. The resistance of the segment in this case equals its normal state resistance. To justify Eq. 2.33 we assume that the phase-fluctuation attempt frequency  $\Omega_0$  and the relaxation time of the order parameter  $\tau$  are defined by the same energy scale and are related to each other by the relation  $\Omega_0 \approx 1/\tau$ . The number of phase slips occurring per

second, according to the Arrhenius law, is  $\Omega_{PS} = \Omega_0 \exp(-\Delta F/k_B T)$ . The time-fraction  $f$  during which each segment of the wire remains in the normal state is the product of the duration  $\tau$  and the number of times the order parameter reaches zero per second, which is  $\Omega_{PS}$ . Thus we get  $f = \tau \Omega_0 \exp(-\Delta F/k_B T) \approx \exp(-\Delta F/k_B T)$ . In this approximate model, during each unit of time, the wire stays normal during a time  $f$  and superconducting during a time  $(1 - f)$ . Since the fluctuations are very rapid, only the average value of the resistance can be detected. Now let us define a set of independent equivalent segments in the wire, each having length  $\xi(T)$  and the normal state resistance  $R_{1N} = R_N \xi(T)/L$ , where  $L$  is the total length of the wire. The time-averaged resistance of each segment is  $\bar{R}_1 \approx R_{1N} f + R_0(1 - f)$ , where  $R_0 \equiv 0$  represents the resistance of each segment in the superconducting state. Finally, the total resistance of the wire can now be written as a product of the average resistance of each independent segment  $\bar{R}_1$  and the total number of such segments  $L/\xi(T)$ . So we get Eq. 2.33 as

$$\begin{aligned}
R_{Little}(T) &= \left( \frac{L}{\xi(T)} \bar{R}_1 \right) \\
&= \left( \frac{L}{\xi(T)} \right) (R_{1N} f + R_0(1 - f)) \\
&= \left( \frac{L}{\xi(T)} \right) (R_{1N} f) \\
&= R_N \exp(-\Delta F(T)/k_B T)
\end{aligned} \tag{2.34}$$

## 2.4 LAMH fit

In the LAMH theory the normal-state resistance of the wire is not explicitly included, in contrast with Little's fit. In the LAMH model, the effective resistance is calculated by considering the time-evolution of the superconducting phase  $\phi(t)$ . To derive the LAMH resistance using the thermally activated phase slip (TAPS) model, we first include the effect of the bias current ( $I_S > 0$ ) in the wire. This makes the free energy landscape “tilted”,

compared to the zero-bias case (see Fig. 2.3). Due to thermal fluctuations, the phase jumps over the barrier constituting a phase slip event that changes the phase by  $2\pi$ . Due to the tilt the phase slip in one direction is more favorable than the other as the energy barrier is lowered in one direction and increased in the other. The amount by which the free energy is lowered or raised is  $\delta F$ . This is the work done by the source during a phase slip event and is given by,

$$\delta F = \int IV dt \quad (2.35)$$

where  $I$  is the current. Using the AC Josephson relation, we can write it as

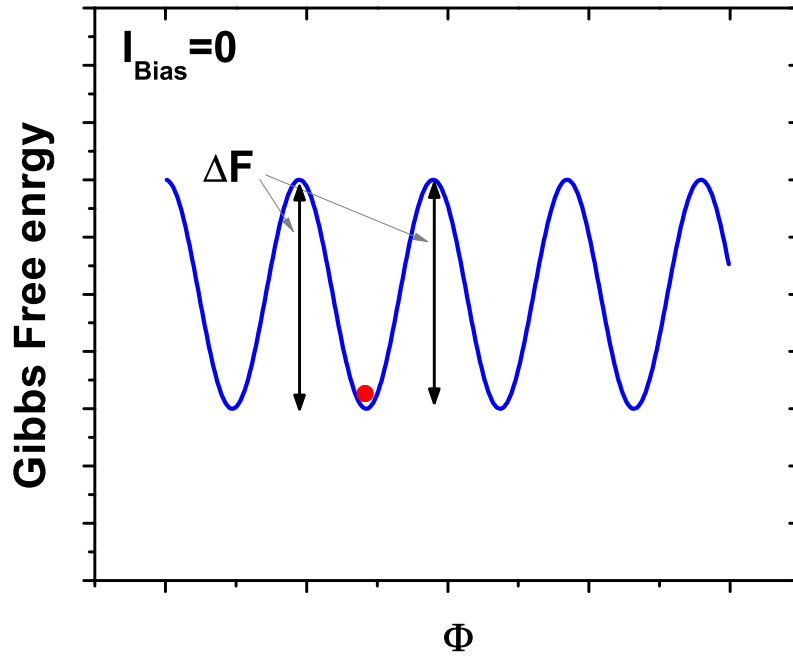
$$\begin{aligned} \delta F &= \int_0^{2\pi} IV dt \\ &= \frac{hI}{2e}. \end{aligned} \quad (2.36)$$

The events that change the phase by  $2\pi$  are called “phase slips”, and the events that change the phase by  $-2\pi$  are called “anti-phase slips”. The free-energy barrier for the phase slips and the anti-phase slips are given by,

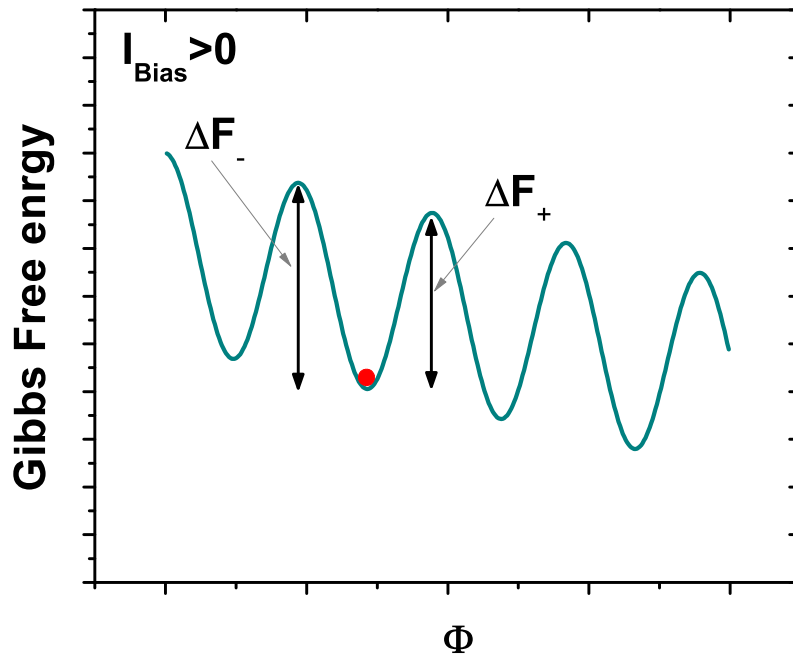
$$\Delta F_+ = \Delta F - (\delta F/2) = \Delta F - (hI/2e) \quad (2.37)$$

$$\Delta F_- = \Delta F + (\delta F/2) = \Delta F + (hI/2e) \quad (2.38)$$

If the system wants to go over this barriers with a frequency  $\Omega$ , it will be successfully excited with probability set by the Boltzmann factors  $\exp(-\Delta F_{\pm}/k_B T)$ . The phase of the system



(a)



(b)

Figure 2.3: Gibbs free energy barrier. (a) With no bias current the energy barriers for phase slips and anti-phase slips are the same. (b) With a bias current the free energy barrier for a phase slip ( $\Delta F_+$ ) is smaller than that for an anti-phase slip ( $\Delta F_-$ ). Hence, the rate of phase slips exceeds that for anti-phase slips.

will then be lost at a rate

$$\begin{aligned}
\frac{d\phi}{dt} &= \Omega_+ - \Omega_- \\
&= \Omega \exp(-\Delta F_+/k_B T) - \Omega \exp(-\Delta F_-/k_B T) \\
&= \Omega \left[ \exp\left(\frac{\Delta F - hI/4e}{k_B T}\right) - \exp\left(\frac{\Delta F + hI/4e}{k_B T}\right) \right] \\
&= \Omega e^{-\Delta F/k_B T} \left[ \exp\left(\frac{hI/4e}{k_B T}\right) - \exp\left(-\frac{hI/4e}{k_B T}\right) \right] \\
&= 2\Omega e^{-\Delta F/k_B T} \sinh\left(\frac{hI}{4ek_B T}\right). \tag{2.39}
\end{aligned}$$

Now, the resistance can be derived from this by using the Josephson relation:

$$\begin{aligned}
\frac{d\phi}{dt} &= \frac{2eV}{\hbar} = 2\Omega e^{-\Delta F/k_B T} \sinh\left(\frac{hI}{4ek_B T}\right) \\
V &= \frac{\hbar\Omega}{e} e^{-\Delta F/k_B T} \sinh\left(\frac{hI}{4ek_B T}\right). \tag{2.40}
\end{aligned}$$

Differentiating the expression for voltage we get the resistance as

$$\begin{aligned}
\frac{dV}{dI} &= \frac{d}{dI} \left[ \frac{\hbar\Omega}{e} e^{-\Delta F/k_B T} \sinh\left(\frac{hI}{4ek_B T}\right) \right] \\
&= \frac{h}{4e^2} \frac{\hbar\Omega}{k_B T} e^{-\Delta F/k_B T} \cosh\left(\frac{hI}{4ek_B T}\right) \tag{2.41}
\end{aligned}$$

When  $I \ll 4ek_B T/h$  (recall that  $4ek_B/h \cong 13.4 \text{ nA/K}$ ), the hyperbolic cosine is essentially equal to one, and the zero-bias resistance can then be given as

$$R = R_Q \frac{\hbar\Omega}{k_B T} e^{-\Delta F/k_B T}, \tag{2.42}$$

where  $R_Q = h/(2e)^2 = h/4e^2$  is the quantum resistance for Cooper pairs.

Now we would like to discuss about the attempt frequency  $\Omega$  for the phase slips. When

Langer and Ambegaokar formulated the theory for phase slips, they assumed for the attempt frequency the inverse of the elastic scattering time, multiplied by the number of electrons in the wire, i.e.,  $nAL/\tau$ . Later, McCumber and Halperin [26] revisited the problem, and using time dependent GL theory they found the temperature-dependent attempt frequency

$$\Omega = \frac{L}{\xi} \left( \frac{\Delta F}{k_B T} \right)^{1/2} \frac{1}{\tau_s}, \quad (2.43)$$

where  $1/\tau_s = 8k_B(T_C - T)/\pi\hbar$  is the GL relaxation time which characterizes the relaxation rate of the superconductor in the time dependent GL theory. In Eq. 2.43  $1/\tau_s$  sets the scale for  $\Omega$ ,  $L/\xi$  is the number of independent wire segments phase slip can attempt to occur, and  $\sqrt{\Delta F/k_B T}$  accounts for the overlap of these segments. The full dependence of the Langer-Ambegaokar-McCumber-Halperin (LAMH) resistance can now be written as

$$R_{LAMH}(T) = Dt^{-3/2}(1-t)^{9/4} \exp[c(1-t)^{3/2}/t] \quad (2.44)$$

where we have used the notation

$$t = T/T_C \quad (2.45)$$

$$c = 0.83(R_Q/R_N)(L/\xi(0)) \quad (2.46)$$

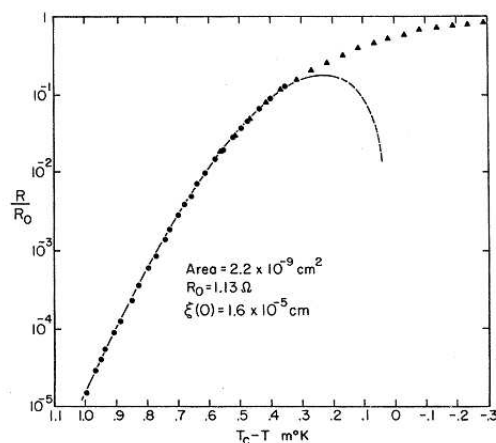
$$D = (8/\pi)(L/\xi(0))R_Q\sqrt{c} \quad (2.47)$$

The normal quasiparticles present in the wire at  $T \sim T_C$  provide a parallel conduction channel. Thus the net resistance can be approximated as

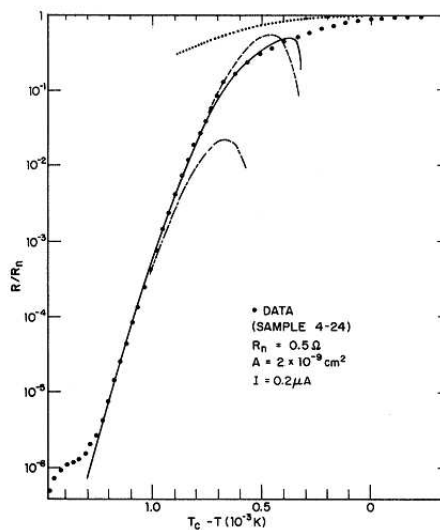
$$R^{-1} = R_{LAMH}^{-1} + R_N^{-1} \quad (2.48)$$

## 2.5 Comparisons with experiments

Early experiments in 1970s by Lukens, Warburton, and Webb [32] and Newbower, Beasley, and Tinkham [33] in separate measurements of single crystal tin “whiskers” (Fig.2.4) with diameters  $\sim 0.5\mu\text{m}$  confirmed LAMH theory. They both found that the resistance below



(a)



(b)

Figure 2.4: (a) Data (symbols) from Lukens, Warburton, and Webb [32] and their fit to LAMH theory (dashed line). (b) Data (symbols) from Newbower, Beasley, and Tinkham [33]. The various fits are to LAMH theory (dashed line), LAMH theory with parallel normal channel (solid line), LAMH theory with different attempt frequency (dot-dashed line), and Tucker-Halperin theory (dotted line). The deviation at lowest temperatures is attributed to contact effects.

$T$  of the wire is well described by the LAMH theory. However, both reports do show some deviation from the theory as  $T \rightarrow T_C$  but this is to be expected, as the theory is only valid when  $\Delta F \gg k_B T$  whereas as  $T \rightarrow T_C$ ,  $\Delta F \rightarrow 0$ . While the agreement between the LAMH theory and the data of Newbower, Beasley, and Tinkham is good, they further found that they could improve their fits by including a parallel normal channel such that  $R^{-1} = R_{LAMH}^{-1} + R_N^{-1}$ .

It has now been established by several experiments on ultra thin MoGe and Nb nanowires that LAMH and Little's fits explain the resistive transitions in homogeneous nanowires. Rogachev *et al.* [21] have shown that in the absence as well as presence of magnetic field the resistance of the nanowire follows the predictions of the LAMH theory up to 11 orders of magnitude (in the range of  $10^3 - 10^{-8}\Omega$ ). The data and the fit to the LAMH theory are shown in the Fig. 2.5a. In this experiment the resistance measured in the zero-bias-current limit is shown by open circles. At lower temperatures, the resistance is measured by fitting the non-linear portion of the  $dV/dI$  curve to the LAMH theory (shown by black squares). The expression used to get these fits is  $dV/dI = R(T) \cosh(I/I_0)$ , where  $R(T)$  is the zero-bias resistance given by Eq. 2.40 and  $I_0 = 4ekT/h$ . The analysis of LAMH model and Little's model were done with the data obtained from measurements on superconducting bridges as in Ref. [34]. The  $R(T)$  curves for these measurements are shown in Fig. 2.5b. The direct low bias transport measurement is shown as open circles. The solid black squares represent the resistance determined by extrapolating the high bias (nonlinear)  $V(I)$  measurements to zero bias. The Little's fit is shown as a solid curve and LAMH fit is shown as a dashed curve. Both curves exhibit a good agreement with the data points at low temperatures where the resistance drops rapidly. This agreement is observed over a range of 11 orders of magnitude of the resistance.

Rogachev and Bezryadin [19] have shown that sub-10 nm thin continuous Nb nanowires show resistive transitions that is well explained by the LAMH model of thermally activated phase slip. The data and the fits are shown in Fig. 2.6a. Also, the generic fits to a model of

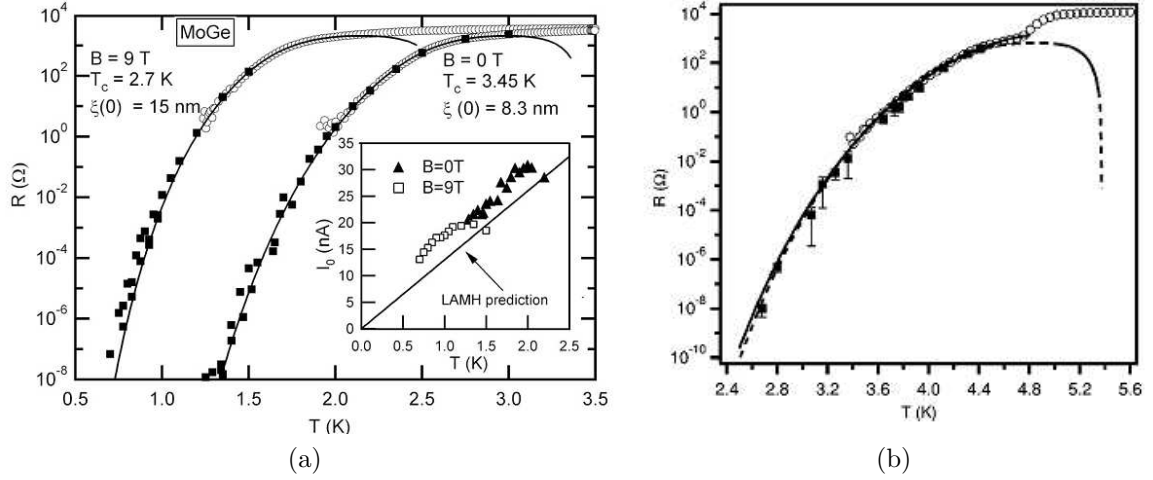


Figure 2.5: (a) Resistance versus temperature for the MoGe nanowire in magnetic fields 0 and 9 T [21]. Open circles represent zero-bias-current measurements and black squares indicate the resistance values obtained from the fit of the non-linear portion of  $dV/dI$  curves. Solid lines are the fits to the LAMH theory. Extracted fitting parameters  $T_C$  and  $\xi(T)$  are indicated. The inset shows the experimental dependence of the parameter  $I_0$  on temperature (solid and open symbols) and the theoretical value  $I_0 = 4ekT/h$  (solid line). (b) Resistance vs temperature curve for sample B2 from Ref. [34]. Open circles represent data that have been directly measured while filled boxes give the resistance values determined by fitting the  $dV/dI$  curves using the formula  $dV/dI = R(T) \cosh(I/I_0)$ . The solid and the dashed curves give the best fits generated by the Little's and LAMH formulas, respectively.

quantum phase slips (from Ref. [18]) is also shown, which clearly deviates from the data. The TEM studies on these wires revealed that these are polycrystalline and consist of randomly oriented grains of size 3-7 nm. More recently, Bollinger *et al.* [14] have shown that a large set of homogeneous superconducting MoGe nanowires follow the the prediction of Little's model. This data is shown in Fig.2.6b from Ref. [14]. The measured zero-bias resistance and the fits (solid lines) to it with the Little's formula (Eq. 2.32) are shown. In all these zero-bias measurements on Nb and MoGe nanowires there is no evidence of quantum phase slips (QPS) in the  $R$  vs.  $T$  data that is obtained down to the smallest resistance measured in the setup. The entire wire transition can be explained by LAMH or Little's fits that incorporates only TAPS.

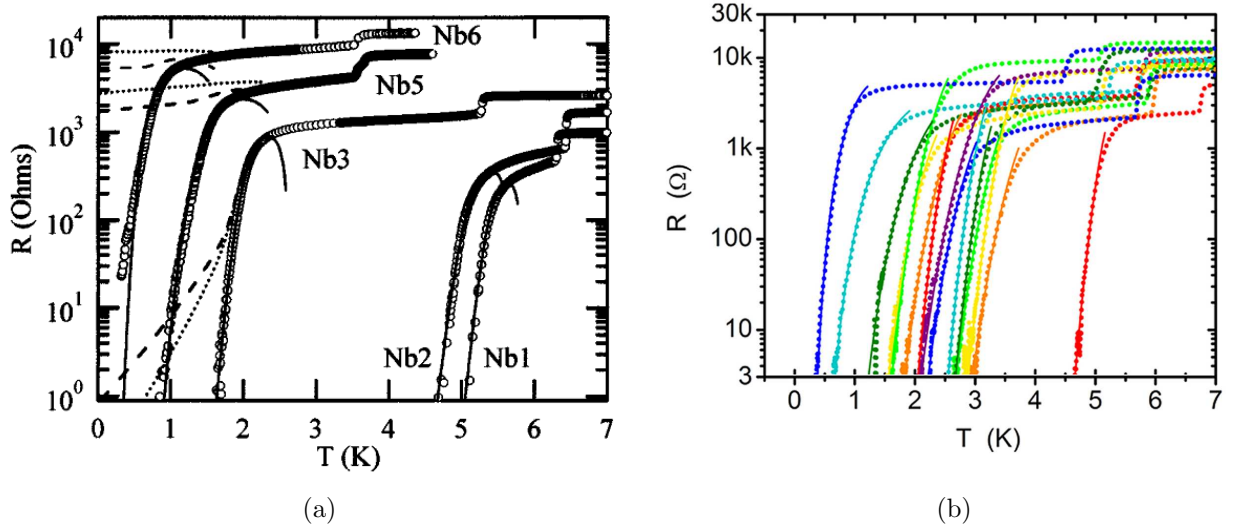


Figure 2.6: (a) Temperature dependence of the resistance of superconducting Nb nanowires (from Ref. [19]). Solid lines show the fits to the LAMH theory. The samples Nb1, Nb2, Nb3, Nb5, and Nb6 have the following fitting parameters. Transition temperatures in K are  $T_C = 5.8, 5.6, 2.7, 2.5,$  and  $1.9$ , respectively. Coherence lengths in nm are  $\xi(0)=8.5, 8.1, 18, 16,$  and  $16.5$ , respectively. The dashed lines are theoretical curves that include the contribution of quantum phase slips into the wire resistance [18], with generic factors  $a = 1$  and  $B = 1$ . The dotted lines are computed with  $a = 1.3$  and  $B = 7.2$ . (b)  $R$  vs  $T$  data for superconducting wires and the fits (solid lines) to the Little formula (from Ref. [14]).

## 2.6 Quantum phase slips

At sufficiently low temperatures, it is expected that quantum tunneling would dominate over thermally activated phase slips in nanowires. In other words, at sufficiently low temperatures quantum fluctuations of the order parameter would lead to phase slips, i.e. quantum phase slips (QPS). Observation of QPS was first reported by Giordano [35] in late 1980's. The experiments were done on In wires of diameter  $\sim 50$  nm. It was found that within  $0.2$  K of  $T_C$  the results agreed well with the TAPS model where the phase slips occur when the phase passes over the free energy barrier (see Fig. 2.7a). But at low temperatures the model failed qualitatively to explain the weak temperature dependent resistance "tails". These tails were interpreted as resistance appearing due to macroscopic quantum tunneling (MQT) of the phase *through* the barrier. In another study by Giordano *et al.* [10], the

superconducting state of PbIn wires were studied. The smallest samples which had diameters below  $200\text{\AA}$  showed significant dissipation below  $T_C$  (see Fig. 2.7b). They also found that the voltage-current characteristics showed oscillatory behavior which were more pronounced as the temperature decreased. They proposed that the observed behavior is due to quantum tunneling of the order parameter and due to existence of discrete energy levels.

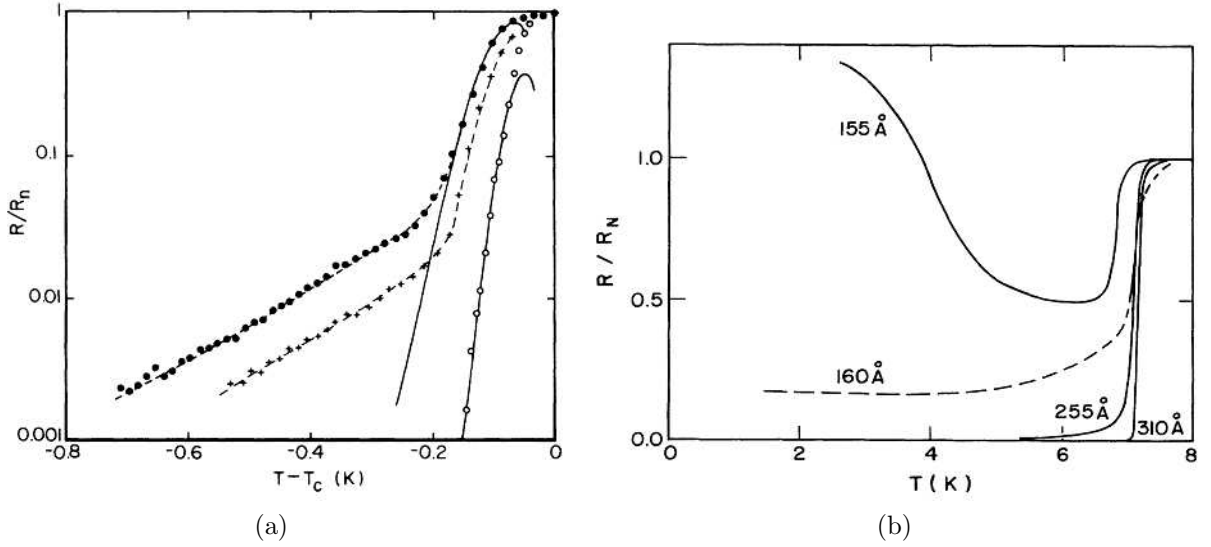


Figure 2.7: (a) Resistance normalized by their normal state resistance as a function of temperature for three In wires from Ref. [35]. The sample diameters were  $410\text{\AA}$  ( $\bullet$ ),  $505\text{\AA}$  ( $+$ ),  $720\text{\AA}$  ( $\circ$ ). The solid lines are fits according to the thermal activation model and dashed lines are the fits to a QPS model (to be discussed later). When the solid and dashed curves overlap only the former is shown for clarity. The wire lengths were 80, 150, 150  $\mu\text{m}$  and the normal-state resistance were 5.7, 7.1, 1.2  $\text{k}\Omega$  respectively. (b) Resistance as a function of temperature for several PbIn samples from [10]. The sample diameters are indicated in the figure.

Giordano proposed a heuristic argument that the resistance from MQT follows a form similar to that of LAMH model (Eqn. 2.42), except that the appropriate energy scale is  $\hbar/\tau_{GL}$  instead of  $k_B T$  [10, 18]. Hence the expression for the resistance due to QPS is given by,

$$R_{QPS} = B \frac{\pi \hbar^2 \Omega_{QPS}}{2e^2 (\hbar/\tau_{GL})} e^{-a\Delta F/(\hbar/\tau_{GL})} \quad (2.49)$$

where,

$$\Omega_{QPS} = \frac{L}{\xi(T)} \sqrt{\frac{\Delta F}{(\hbar/\tau_{GL}) \tau_{GL}}} \frac{1}{\tau_{GL}} \quad (2.50)$$

and  $a$  and  $B$  are possible numerical factors of the order of unity. Due to QPS we expect that sufficiently narrow wire would have resistance even as  $T \rightarrow 0$ . If we just consider TAPS alone we would expect the resistance to approach zero as  $T \rightarrow 0$ , since the thermal fluctuations scale with temperature. The total resistance of the superconducting channel at any temperature is given by the the sum of the resistance due to thermal fluctuations and quantum fluctuations, i.e,  $R_{fluc} = R_{LAMH} + R_{QPS}$ . Unless  $R_{fluc}$  is small compared to  $R_N$ , the resistance measured will be significantly reduced due to the current carried by the parallel normal channel. Lau *et al.* [36] proposed taking this effect into account to predict the total resistance as,

$$R = [R_N^{-1} + (R_{LAMH} + R_{QPS})^{-1}]^{-1} \quad (2.51)$$

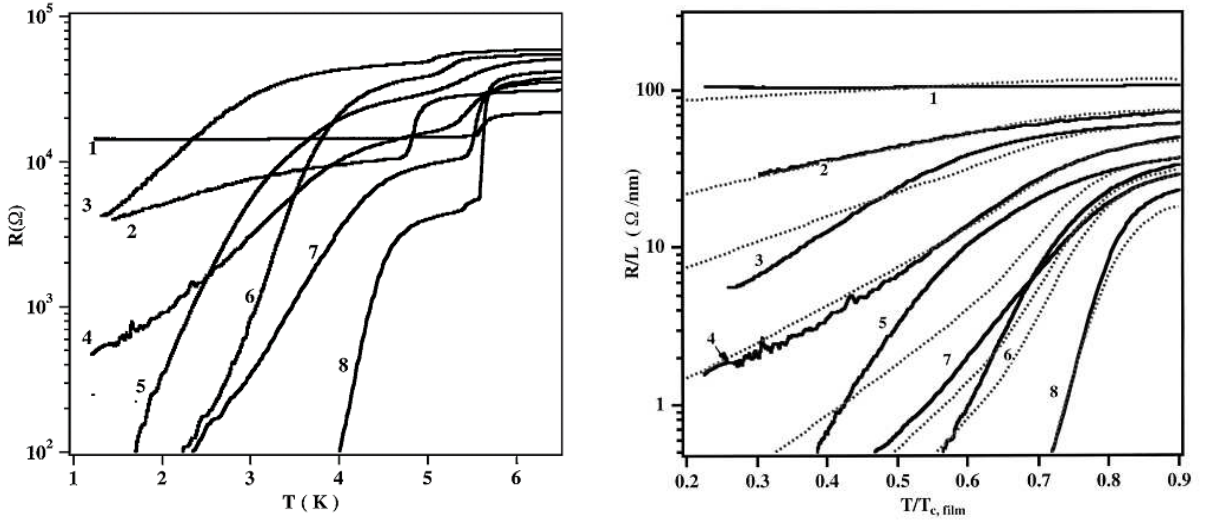


Figure 2.8: (a) Resistance as a function of temperature for eight different samples from Ref. [36]. The samples' normal resistance and lengths are 1: 14.8 k $\Omega$ , 135 nm; 2: 10.7 k $\Omega$ , 135 nm; 3: 47 k $\Omega$ , 745 nm; 4: 17.3 k $\Omega$ , 310 nm; 5: 32 k $\Omega$ , 730 nm; 6: 40 k $\Omega$ , 1050 nm; 7: 10 k $\Omega$ , 310 nm; 8: 4.5 k $\Omega$ , 165 nm. (b) Resistance per unit length vs. normalised temperature data (solid lines) for the same eight samples as shown in Fig. 2.8a from Ref. [36]. The dotted lines are fits using Eq. 2.51 and sample parameters. The two free parameters used are  $a = 1.3$  and  $B = 7.2$  for the whole family of curves.

The group also performed measurements of a large number of amorphous MoGe wires with various widths and lengths. They found a systematic broadening of the superconducting transition with decreasing cross-sectional areas, which can be described quantitatively by a combination of thermally activated phase slips close to  $T_C$  and QPS at low temperatures. Using a simple model with only two free parameters of order unity for the entire family of curves, they found good agreement with the data over a wide range of samples. These nanowires were formed by method of molecular templating using carbon nanotubes (to be discussed in the next chapter). In this work over 20 samples were measured and a representative set showing the resistance vs temperature data for eight different wires was obtained (Fig. 2.8a from Ref. [36]). In contrast to this apparent simple dichotomy the R-T curves in Fig. 2.8a display a broad spectrum of behaviors, including some superconducting samples with resistance as high as  $40 \text{ k}\Omega$  ( $\gg R_Q$ ). It indicates that the relevant parameter controlling the superconducting transition is not the ratio of  $R_Q/R_N$  (as indicated by Ref.[13]), but appears to be the resistance per unit length or equivalently, the cross-sectional area. This is illustrated by the solid lines in Fig. 2.8b, which plots  $R_L$  vs  $t \equiv T/T_{C, \text{film}}$ . Here  $t$  is the temperature normalized to film  $T_C$ . The resistances of wider wires ( $R_N/L < 20 \text{ }\Omega/\text{nm}$ ) drop relatively sharply below  $T_{C, \text{film}}$ . The transition widths broaden with increasing values of  $R_N/L$ , and resistances of the narrowest wires ( $R_N/L > 80 \text{ }\Omega/\text{nm}$ ) barely change with temperature down to 1.5 K.

They found that the broad resistive transitions observed in the wires can not be described by LAMH theory (Eq. 2.44) alone. To add the contribution of QPS they used the expression for  $R$  of wire given by Eq. 2.51. To get the resistance due QPS the Eq. 2.49 was used. This fits are shown as dotted lines in Fig. 2.8b. The most significant fact was that the entire family of curves could be fitted with only one set of values for  $a$  and  $B$  ( $a = 1.3$  and  $B = 7.2$ ).

A microscopic theory of QPS in nanowires was proposed by Golubev and Zaikin [37, 15] using the renormalization theory. Within this model if the wire is short enough so that only

one phase slip event can happen at a time, we can neglect the effects of interaction of the phase slips [38]. In this limit the QPS rate is given by,

$$\Gamma_{QPS} = \frac{S_{QPS} L}{\tau_0 \xi} \exp(-S_{QPS}) \quad (2.52)$$

where the action  $S_{QPS}$  is

$$S_{QPS} = A_{GZ} \left( \frac{R_Q}{\xi} \right) \left( \frac{R_N}{L} \right) \quad (2.53)$$

with  $A_{GZ}$  being a numerical constant,  $R_Q = h/4e^2$ , and  $\tau_0 \sim h/\Delta$  is the characteristic response time of a superconducting system that roughly determines the duration of each QPS,  $\xi$  is the superconducting coherence length [15, 37]. The effective time averaged voltage  $V_{\text{eff}}$ , due to fluctuations, can be calculated from the QPS rate using the Josephson relationship. Thus the effective resistance for nanowire due to QPS can be given by the expression,

$$R_{QPS} \equiv \frac{V_{\text{eff}}}{I} = \frac{h\gamma_{QPS}}{2eI} \quad (2.54)$$

Zgirski *et al.* (Ref. [39]) found reasonable agreement of the data obtained from measurement Al nanowires with the Golubev and Zaikin model. In their experiment, they started with an Al nanowire with diameter  $\sqrt{\sigma} = 71$  nm, fabricated conventional e-beam lithography. The diameter of the wire was subsequently reduced by  $Ar^+$  ion sputtering (reduced down to  $\sqrt{\sigma} = 8$  nm). The resistance vs. temperature data for a Al nanowire whose diameter was reduced after each measurement is shown in Fig. 2.9. They found that for thicker wires for larger effective cross section diameters from  $\sqrt{\sigma} > 17$  nm), the  $R(T)$  dependencies follow the same qualitative behavior: relatively narrow transition with quasi-linear slope in logarithmic scale. These experimental data can be fitted with a reasonable accuracy by theoretical calculations within the model of thermally activated phase slips (fits not shown). But for thinner wires with diameters  $\sim 11$  nm or smaller, the transitions become wider and the data can not be fitted alone the theory of TAPS with ant reasonable set of parameters

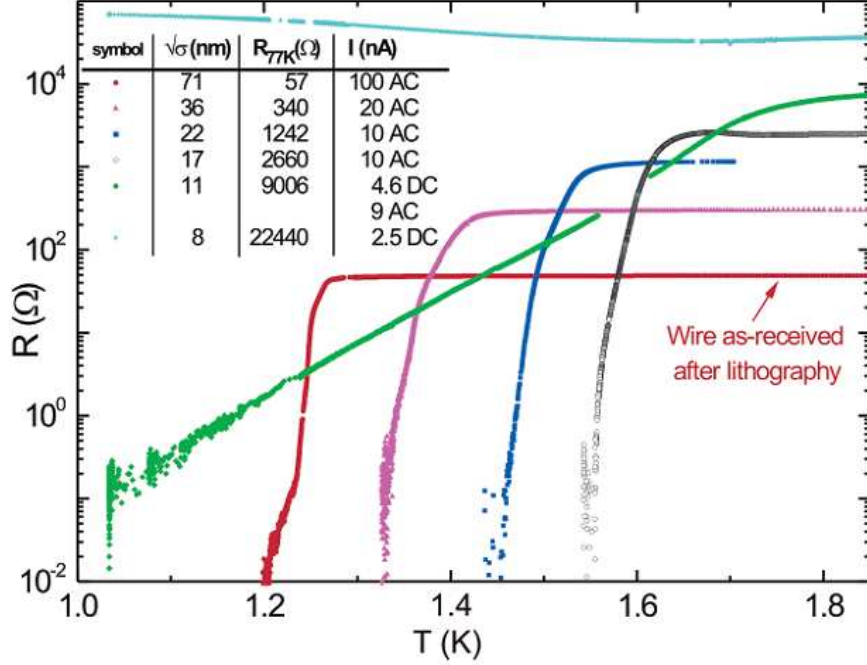


Figure 2.9: Resistance vs temperature for the same wire of length  $L = 10 \mu\text{m}$  after several sputtering sessions from Ref. [39]. The sample and the measurement parameters are listed in the table. For low-Ohmic samples, lock-in AC measurements with the front-end preamplifier with input impedance  $100 \text{ k}\Omega$  were used; for resistance above  $500 \Omega$  they used DC nanovolt preamplifier with input impedance  $1 \text{ G}\Omega$ . The absence of data for the  $\sigma = 11 \text{ nm}$  sample at  $T = 1.6 \text{ K}$  was due to switching from DC to AC setup. There is a qualitative difference of  $R(T)$  dependencies for the two thinnest wires from the thicker ones.

(see Fig. 2.10). But they got agreement with the model of QPS proposed by Golubev and Zaikin (Eq. 2.52) as shown in Fig. 2.10.

In their subsequent work, Zgirski *et al.* (Ref. [38]) showed that with the progressive reduction on a particular Al nanowire, the gradual broadening of the resistive transition that could be explained with the model of Golubev-Zaikin (using Eq. 2.52 and Eq. 2.54). The resistance vs temperature data for the thinnest samples for the same Al nanowire obtained by progressive reduction of the diameter is shown in Fig. 2.11. The length of the nanowire  $L$  is  $10 \mu\text{m}$ . The best fit with LAMH model is shown in for 2 nanowire samples. Clearly, LAMH model can not explain the data, however the fitting done using Eq. 2.52 and Eq. 2.54, gives reasonable agreement.

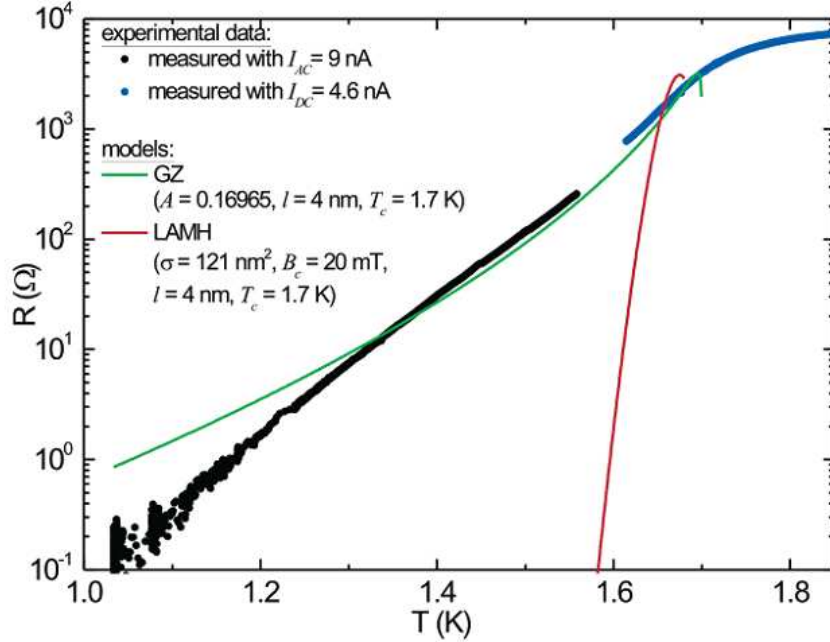


Figure 2.10:  $R(T)$  dependence for the  $\sqrt{\sigma} = 11$  nm sample from ref. [39]. Green line shows the result of fitting to the Golubev-Zaikin model with  $A$ ,  $l$ , and  $T_c$  being fitting parameters. The same set of parameters together with the critical magnetic field  $B_C$  measured experimentally was used to show corresponding effect of thermally activated phase slips on the wires  $R(T)$  transition (red line). The parameter  $\sigma$  is obtained from the normal state resistance value and the known sample geometry.

Recently, Altomare *et al.* (Ref. [40]) have found evidence for quantum phase slip in long Al nanowires with lateral dimensions  $\sim 5$  nm. The lengths of the two wires measured were 10 and 100  $\mu\text{m}$ . They studied the residual resistance deduced from the nonlinear  $I$ - $V$  characteristics in the superconducting state below the critical current. Their main finding is that the  $I$ - $V$  dependence and residual resistance are inconsistent with the classical LAMH behavior, but instead are well described by quantum expressions. The data from Ref. [40] is shown in Fig. 2.12. The measured non-linear  $I$ - $V$  curves and the linear resistance at magnetic field  $H = 0$  T and  $H = 0.45$  T for various temperatures is shown. For TAPS, the

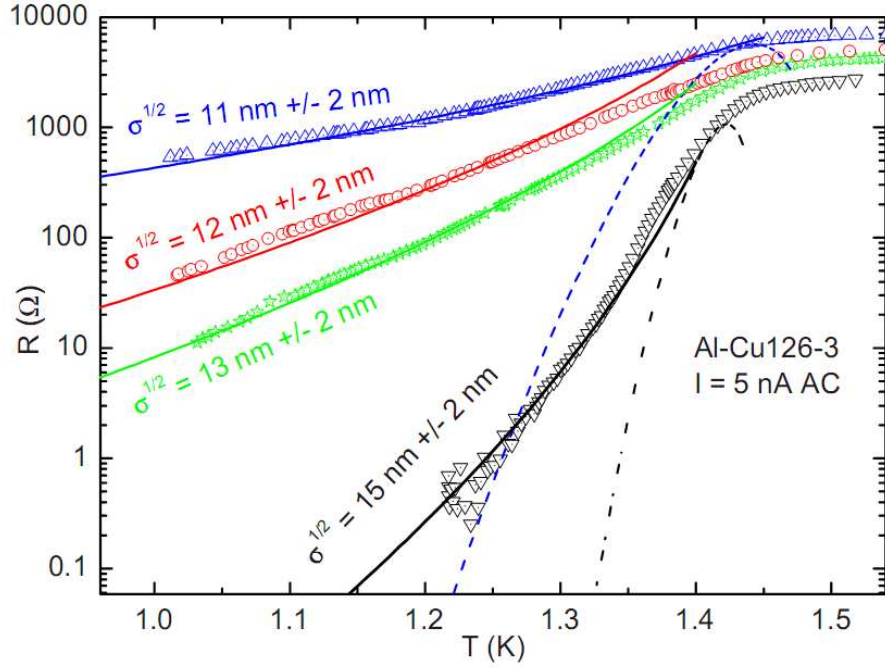


Figure 2.11: Resistance vs temperature for the thinnest samples obtained by progressive reduction of the diameter of the same aluminum nanowire Al-Cu126-3 with length  $L=10 \mu\text{m}$  from Ref. [38]. The Langer-Ambegaokar-McCumber-Halperin (LAMH) model fitting is shown with dashed lines for 11 and 15 nm samples with the best-fit mean free path  $l = 3$  and 10 nm, correspondingly,  $T_C = 1.46 \text{ K}$  and critical magnetic field  $B_C = 10 \text{ mT}$ . Fitting using a simplified short-wire model Eq. 2.52 and Eq. 2.54 is shown with solid lines. For 11-, 12-, 13-, and 15-nm wires the fitting parameters are  $T_C = 1.5 \text{ K}$ ;  $A = 0.15$ , mean free path  $l = 5.4, 5.8, 7.3, 7.5 \text{ nm}$ ; and the normal-state resistance  $R_N = 7200, 5300, 4200, \text{ and } 2700 \text{ k}\Omega$ .

expression for linear resistance and high-bias residual voltage are,

$$R_{LAMH} = R_Q \frac{\Omega}{k_B T} \exp\left(\frac{\Delta F}{k_B T}\right) \quad (2.55)$$

$$V_{TAPS} = I_0 R_{LAMH} \sinh\left(\frac{I}{I_0}\right) \quad (2.56)$$

where,

$$\begin{aligned}R_Q &= h/4e^2 \\ \Omega &= (L/\xi)(\Delta F/k_B T)^{1/2}(\hbar/\tau_{GL}) \\ \Delta F &= (8\sqrt{2}/3)(H_{th}^2/8\pi)A\xi \\ \tau_{GL} &= (\pi/8)[\hbar/k_B(T - T_C)] \\ I_0 &= 4ek_B T/h\end{aligned}$$

and  $L$  is the wire length,  $A$  is the cross-sectional area,  $\xi$  is the GL coherence length of the wire,  $H_{th}$  is the thermodynamical critical field.

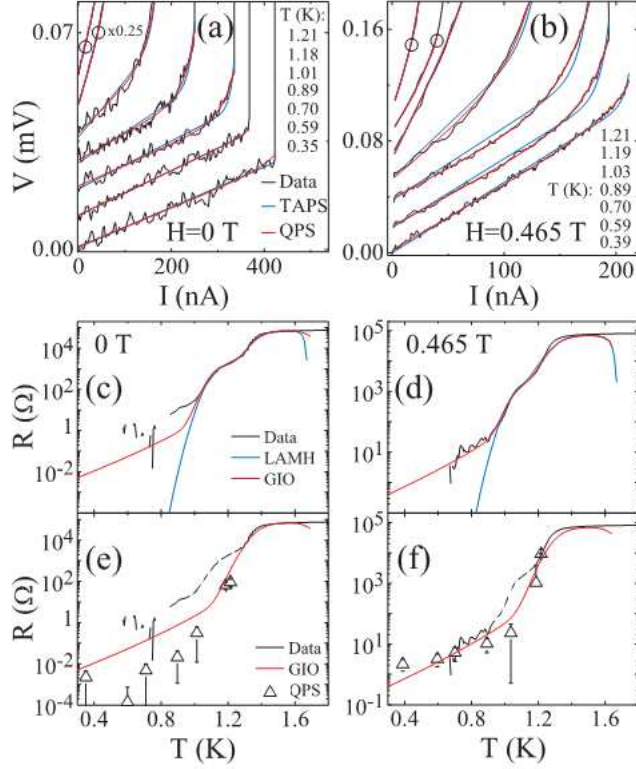


Figure 2.12: Nonlinear  $I$ - $V$  curves and linear resistance for a Al wire sample from Ref.[40] at different magnetic fields ( $H$ ): Black curves-data; red curves-fits to the GIO( $\equiv$  GIO+LAMH) expressions for QPS( $\equiv$  TAPS+QTPS), and blue curves- fits to the LAMH expressions for TAPS alone. (a)-(b)  $I$ - $V$  curves offset for clarity.(c)-(d) Linear resistance after background subtraction. The LAMH fits are poor at low temperatures. (e)-(f) The resistance contribution due to phase slips ( $R_{QPS}$ ) extracted from (a)-(b) from fits to the  $I$ - $V$  curves using GIO expressions.

For QPS they have used the model proposed by Giordano and the corresponding expressions for linear resistance and residual voltage is,

$$R_{GIO} = R_Q \left( \frac{L}{\xi} \right) \sqrt{a_{GIO} \left( \frac{\Delta F}{\hbar/\tau_{GL}} \right)} \exp \left( -a_{GIO} \frac{\Delta F}{\hbar/\tau_{GL}} \right) \quad (2.57)$$

$$V_{QTPS} = I_{GIO} R_{GIO} \sinh \left( \frac{I}{I_{GIO}} \right) \quad (2.58)$$

where  $a_{GIO}$  is the order of unity and  $I_{GIO} = 2e/\pi\tau_{GL}a_{GIO}$ .

# Chapter 3

## Fabrication and transport measurements of superconducting nanowires

We fabricate our nanowires using the method of molecular templating [13]. This method employs a suspended linear molecule as a template subjected to a thin layer of metal deposition to produce a *quasi*-one-dimensional system. Superconducting wires have been fabricated in the past by a number of different means. Some of the earliest work relied on using single crystals of tin, known as whiskers, to study one-dimensional superconductivity [32, 33]. These whiskers were of the order of  $\sim 50 \mu\text{m}$ , which make them one-dimensional at temperatures close to  $T_C$ . As fabrication technology improved, wires of increasingly smaller cross-sectional area were made using step edge [35] and stencil mask techniques [41]. These methods hinted at possible quantum effects, such as quantum phase slips [35] and quantum phase transition, such as metal-insulator transition [41], which may exist in superconducting wires of reduced dimensions.

To make wires with diameters that are small enough [15] ( $< 10 \text{ nm}$ ) to explore these quantum effects we have used the method of molecular templating which has been extensively developed in our group [13, 42, 28]. The basic idea behind this technique is to deposit superconducting metal onto a free-standing molecule. Several molecules used as templates include carbon nanotubes [13, 36], fluorinated carbon nanotubes [43, 44], DNA molecules [42, 45], and  $\text{WS}_2$  nanorods [46]. Since the width of a molecule is on the order of a nanometer, the wire formed on top of the molecule will have a comparable width. The molecule should be rigid, straight and stable enough to withstand the metal deposition process. The molecule should have good adhesion property with the metal to produce homogeneous nanowires free from defects such as granularity. This method has the advantage that the diameter of the

wire depends on the amount of deposited material, which is a quantity that is easily controlled during the sputtering process. Also, many wires are fabricated on the same substrate, allowing us to choose the best (based on apparent homogeneity, desired dimensions, etc.) for measurement. It should be noted that this technique is not limited to making superconducting wires – by using different metals (and perhaps an appropriate sticking layer) normal metal and ferromagnetic wires can also be fabricated [47].

## **3.1 Fabrication of superconducting nanowires on top of carbon nanotubes**

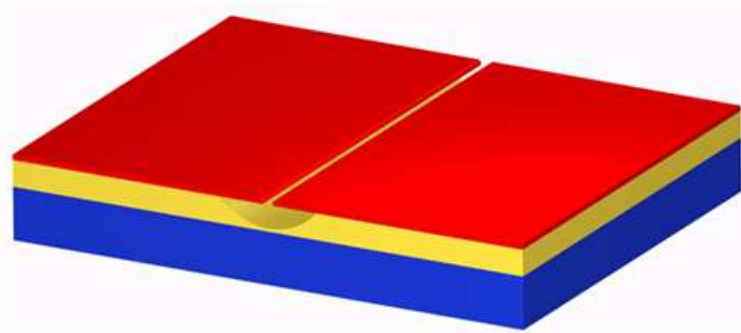
### **3.1.1 Preparation of the substrate**

In our method for fabricating superconducting nanowires, the first step is to prepare a substrate that has a trench of  $\sim 100$ - $500$  nm wide for deposition of free-standing molecules as templates. We begin with a 4 inch in diameter and  $500 \mu\text{m}$  thick Si-100 wafer. On the wafer a layer constituting of a  $0.5 \mu\text{m}$   $\text{SiO}_2$  grown by dry ( $0.1 \mu\text{m}$ ) and wet ( $0.4 \mu\text{m}$ ) oxidation. On top of it,  $60$  nm low stress SiN layer is deposited by low-pressure chemical vapor deposition. The wafer is coated with an e-beam sensitive resist (PMMA). The entire wafer is written with fine lines (widths of  $\sim 100$  nm) spaced at a distance of  $4.8$  mm. To locate the nanowires on the trench during the fabrication process, numbered markers are placed off to the side the lines that can be easily seen in an optical microscope. In order to explore the properties nanowires with different lengths, patterns with line widths of  $50$ ,  $100$ , and  $450$  nm were used. The numbered markers are spaced  $20 \mu\text{m}$  apart, so we have  $\sim 240$  markers in a  $4.8$  mm long chip.

After developing the patterns parts of the SiN layer are exposed and the pattern is transferred into this SiN layer by reactive ion etching(RIE) using a  $\text{SF}_6$  plasma in Uniaxis 790 series reactive ion etching system. The e-beam resist is subsequently removed with



(a)



(b)

Figure 3.1: Preparation of the substrate: (a) Si(0.5 mm)-SiO<sub>2</sub>(500 nm)-SiN(60 nm) substrate with 50-500 nm wide trench defined by e-beam lithography and etch in SF<sub>6</sub> plasma. (b) Substrate with a under-cut in the SiO<sub>2</sub> layer produced by HF dip which etches SiO<sub>2</sub> faster than SiN.

acetone and the entire wafer is coated with photoresist (AZ5214). An automated dicing saw is used to cut the wafer into individual 4.8 mm × 4.8 mm patterned chips. The previous photoresist deposition ensures that the SiN layer is protected from the silicon “dust” created by the dicing. After dicing, this silicon dust can be easily removed along with the photoresist. To remove the photoresist we sonicate the chip in acetone for 5 min. followed by rinsing in deionized water for ~30 sec. The chip is then sonicated in nitric acid for 5 min. followed by another rinse in deionized water for ~30 sec. At this point (Fig. 3.1a) the chip is immersed in hydrofluoric acid for 10 sec. which creates an undercut in the SiO<sub>2</sub> layer due to the much greater etching rate of SiO<sub>2</sub> compared to SiN (Fig. 3.1b). This is followed by rinsing in deionized water for ~30 sec., soaking in nitric acid for 2 min. to remove any residual organics, rinsing in deionized water for ~30 sec, rinsing in isopropanol for ~30 sec., and

then blowing the chip dry with forced nitrogen gas.

### 3.1.2 Deposition of fluorinated single walled carbon nanotubes

We have used fluorinated single walled carbon nanotubes (FSWNTs) as templates for fabrication of our nanowires. These molecules are ideal templates for wires as they are known to be insulating [48], which eliminates any possible conduction channel in parallel with the nanowire. The insulating nature of the FSWNTs insures that we do not place any dissipative environment in close proximity with the wires that could affect any quantum phase slip processes. The FSWNTs can also be easily dissolved in isopropanol, which makes depositing them from solution rather simple. These nanotubes are commercially available (Carbon Nanotechnologies, Inc.) to be easily acquired and do not need to be grown by the user. When starting with FSWNTs as received from the manufacturer the first step is to make a “master” solution. This is prepared by sonicating a small piece (about 1 mm<sup>3</sup>) of bulk FSWNTs in isopropanol (about 12 ml) for 20 min. The sonication will help to break up the FSWNT clusters and promote their dissolving. After sonication the master solution should be nearly transparent with a slight grey color to it. If any visible clusters of FSWNTs remain, the solution should be further sonicated before using.

A separate diluted solution can be obtained from the master solution for depositing FSWNTs. If the master solution has been stored for some time it is recommended that the solution be sonicated for about 5 min. to ensure the FSWNTs are well dispersed before making the diluted solution. A typical dilution is 1:5 to 1:20 parts master solution to isopropanol by volume, though this can vary somewhat depending on how rich the master solution was made. The dilution is tested by making a diluted solution, depositing a drop of it onto a chip with a trench in it, letting the drop sit for 1 min., blowing the excess off with forced nitrogen gas, and then examining the chip under an SEM. We ideally want one nanotube crossing the trench about every 20  $\mu\text{m}$  or one marker. This allows for an easier alignment during photolithography steps. Once we have calibrated the proper dilution we

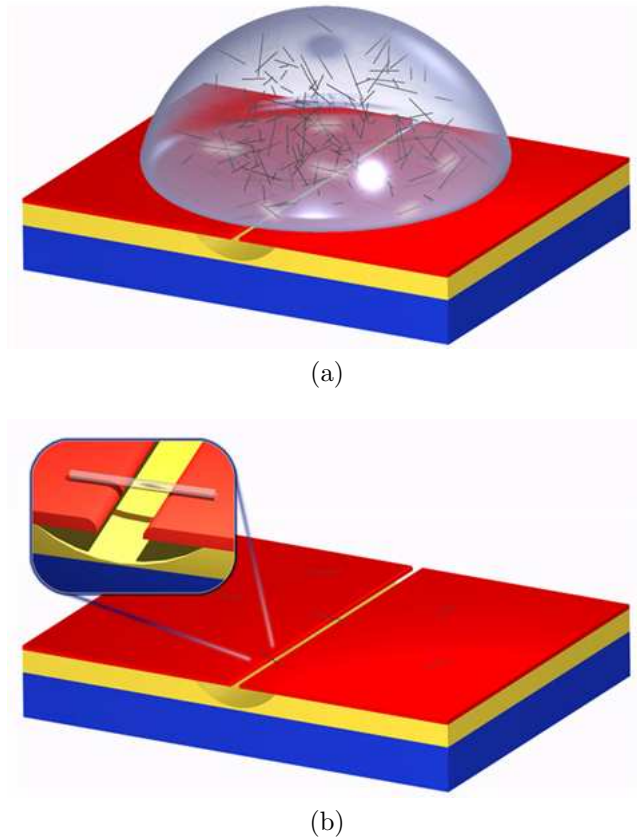


Figure 3.2: Deposition of Fluorinated single walled carbon nanotube: (a) Carbon nanotubes are deposited in solution of isopropanol onto the substrate. The nanotubes are allowed to settle and stick to the surface of the substrate. (b) The substrate is dried off with forced nitrogen gas, and those nanotubes that settled onto the surface of the substrate adhere to the surface. Some of these nanotubes may span the trench.

can use it each time for the same master solution. It should be noted the dilution of the master solution has to be tuned according to the width of the trench on which the FSWNTs are to be deposited. The narrower is the trench, the more diluted should be the solution. Care must be taken not allow any isopropanol to evaporate from the solution (which would change the concentration) while the solution is being stored.

To deposit FSWNTs as template on a chip with a trench, we proceed as before: carefully placing one drop of diluted solution from a pipette onto the surface of a freshly undercut and cleaned chip(Fig.3.2a), waiting for 1 min., and blowing the excess off with forced nitrogen gas. It is important not attempt to clean the chip any further with isopropanol as this will

remove the FSWNTs that we have just deposited. Since the length of the FSWNTs is of the order of a few microns or more some will be deposited to one side or the other of the trench but some will be found across the trench providing templates for the nanowires(Fig.3.2b).

### 3.1.3 Sputtering of superconducting material

One of the goals of our fabrication technique is make superconducting wires that were as thin as possible and yet still continuous and homogeneous. We also preferred them to have a critical temperature that is high enough, so that we could easily measure their properties using standard liquid and  $^4\text{He}$  and  $^3\text{He}$  cryostats.

The specific choice of the MoGe alloy used in this experiment was heavily influenced by the work of others in our research group working on fabricating superconducting nanowires using carbon nanotubes as a template (esp. A. T. Bollinger and A. Rogachev [28, 43, 21, 49]) and using DNA molecules as templates (D. Hopkins [42, 45]). From previous studies on  $\text{Mo}_{1-x}\text{Ge}_x$ , it has been shown that the  $T_C$  of  $\text{Mo}_{1-x}\text{Ge}_x$  increases linearly as the concentration of Ge is reduced until  $x < 0.2$ , when there is a structural change in the MoGe from an amorphous state to a body-centered-cubic (BCC) crystalline structure [50, 51]. We have decided to use  $\text{Mo}_{79}\text{Ge}_{21}$  to obtain the maximum possible  $T_C$  while avoiding the structural transition. Some typical parameters of this material relevant to this work are presented in Table 3.1.

We sputter this alloy using the AJA ATC 2000 custom four gun co-sputtering system located in the Frederick Seitz Materials Research Laboratory's Microfabrication and Crystal Growth Facility. This system is equipped with a liquid nitrogen cold trap that is essential for reducing oxygen impurities in the sputtered films, which can heavily reduce or eliminate superconducting properties. By using the cold trap, the main chamber base pressures were typically below  $\sim 10^{-7}$  Torr before sputtering. The MoGe target was always pre-sputtered for  $\sim 5$  min before any sample was placed in the chamber to reduce contamination from other materials sputtered by other users. Then, without breaking vacuum, the samples can be

Resistivity ( $\rho$ )	180 $\mu \Omega$ cm
Mean Free Path ( $l$ )	3 Å
Fermi Velocity $v$	10 <sup>6</sup> m/s
Diffusion Constant D	5 × 10 <sup>-5</sup> m <sup>2</sup> /s
Transition Temperature $T_C$	7.36 K (bulk)* 5.62 K (film)*
Energy Gap ( $\Delta(0)$ )	1.1 meV (bulk)* 1.0 meV (film)*
Zero Temperature Coherence length ( $\xi(0)$ )	4.4 nm (bulk)* 4.9 nm (film)*
Pippard (BCS) Coherence Length ( $\xi_0$ )	210 nm (film)
Magnetic Penetration Depth ( $\lambda_{eff}(0)$ )	424 nm (film)*
Lower Critical Field ( $H_{C1}$ )	2 mT (film)
Upper Critical Field ( $H_{C2}$ )	12.2 T (bulk)* 6.7 T (film)*
Debye Temperature ( $\Theta_D$ )	266 K

Table 3.1: Properties of MeGe: Measured and derived physical parameters of MoGe  
\* from [51]

inserted into the main chamber from the load lock chamber. During the sputtering process, the sample is rotated  $\sim 20$  rpm to aid in the uniformity of the deposited films. The films were sputtered using a DC power source set at 150 W and a pressure of 3 mT of argon gas with a flow rate of 20 sccm into the chamber. This procedure results in a deposition rate of 1 nm per 8 seconds as determined by profilometry. We typically sputter 8-15 nm of MoGe to make wires, because we consistently want to find wires that are superconducting but are not so wide that a two-dimensional fluctuation (i.e. a vortex) can reside in the wire. The thicker is the wire, higher is its critical current. We would like to mention that once the MoGe target was replaced with another new target (SCM Inc.), the previous sputtering conditions did not produce superconducting films. This problem was rectified by using higher sputtering

power (300–350 W) and lower chamber pressure ( $\sim 1$  mTorr). With these conditions the new sputtering rate was  $\sim 2.7$  Å/s. It should be noted that high power while sputtering can damage the target if it has Indium bonding to the back gate as the Indium can melt and leak towards the MoGe target at such high powers. Since the top of MoGe films is heavily affected by oxidation over time ( $\sim 2.5$  nm becomes oxidized after initial exposure to air, and the oxidation is slow thereafter), we always store the sputter-coated chips in a dessicator until we are ready to perform other processes on the chip. After the sputtering process the substrate and the nanotubes spanning the trench are coated with a thin layer of the superconducting material.

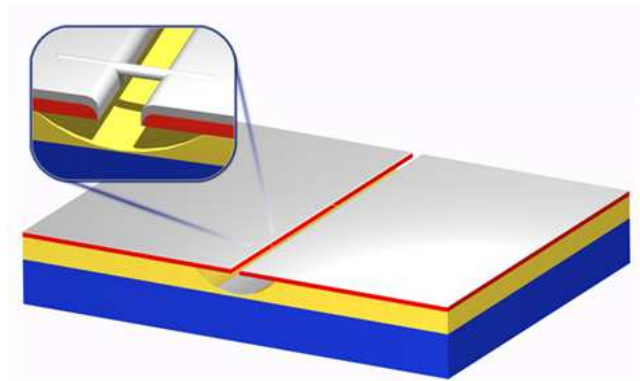


Figure 3.3: Deposition of metal: The surface of the substrate including the nanotubes are sputter coated with several nanometers of superconducting metal.

### 3.1.4 Scanning electron microscopy

After sputtering, the thin superconducting film sections on either side of the trench are connected by several nanowires which span the trench. For our measurement on single nanowire, we need a only one wire on a chip somewhere along the 4.8 nm of the trench. To do this, we search the whole length of the trench of each chip using a Hitachi S-4700 scanning electron microscope (SEM) located in the Center for Microanalysis of Materials. A few representative SEM images to illustrate what the wires look like at this point in the process are shown in Fig. 3.4 .

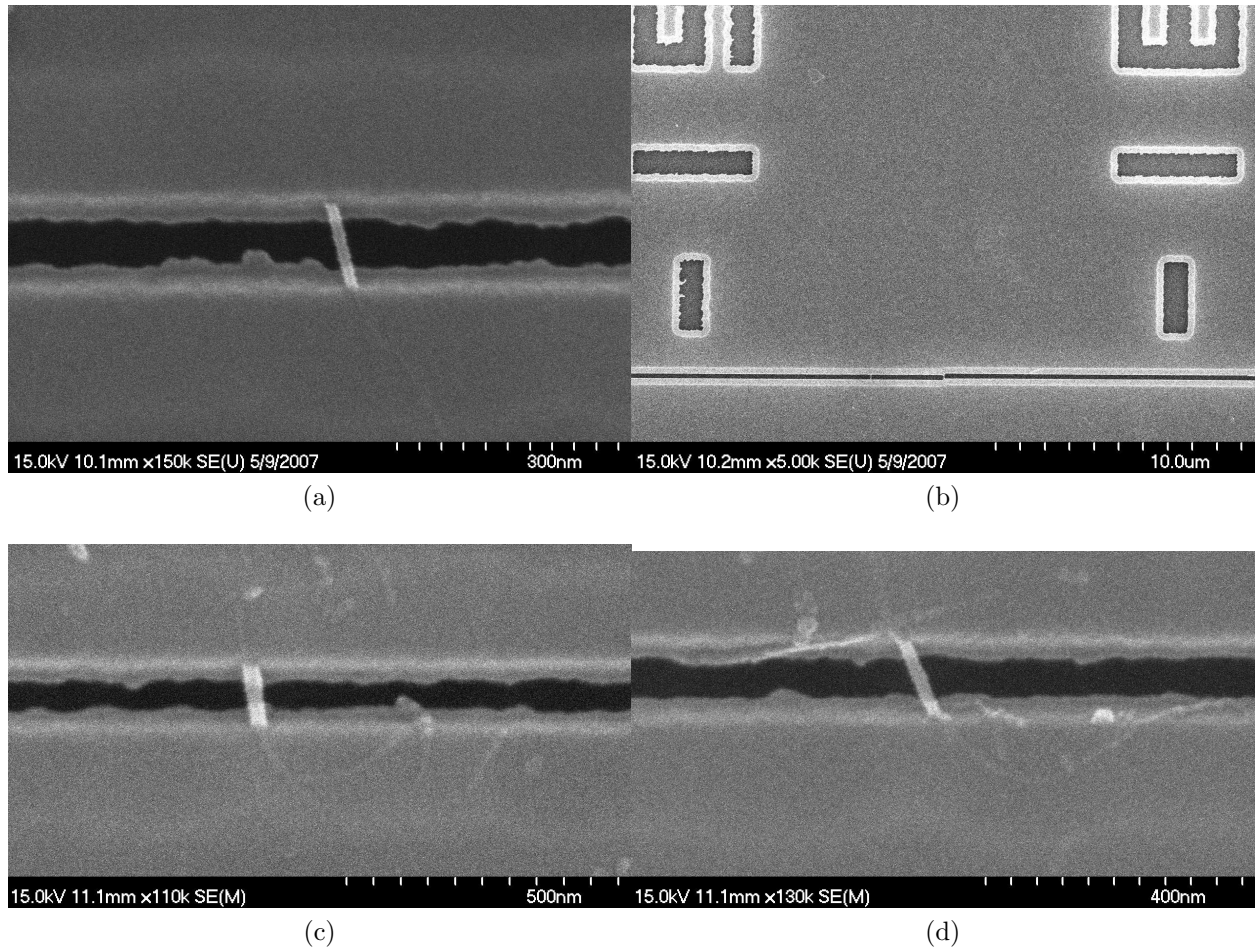


Figure 3.4: Scanning Electron Microscope (SEM) images of nanowires. (a) A nanowire of length  $L = 120$  nm on a  $\sim 100$  nm wide trench. (b) A trench of width  $\sim 100$  nm with markers that are  $20 \mu\text{m}$  apart. The wire position is noted with respect to these markers. The markers are large enough to be seen with an optical microscope during the photolithography process. (c) A nanowire of length  $L = 80$  nm on a  $\sim 50$  nm wide trench. (d) A nanowire of length  $L = 120$  nm on a  $\sim 100$  nm wide trench.

The goal is to identify wires that are visibly homogeneous, are visibly thin, and have no visible breaks or granularity. If possible, we try to find wires that are relatively isolated from other wires. The isolation is necessary since our photolithography mask (discussed later) has a width of  $\sim 10 \mu\text{m}$  near the pattern for the leads, and all wires under the mask (within  $\sim 10 \mu\text{m}$ ) will be measured unless destroyed by some other process. One additional difficulty for some applications is that the markers used for recording locations of wires may cause defects in the film, which becomes important when the magnetic screening current profile

in the leads has observable effects. Whenever possible, wires nearly halfway in between the markers were chosen as they are the easiest to pattern during photolithography. After all of the locations for wires have been imaged and recorded, the SEM images are compared and the best location on each sample is chosen. The SEM images of the wires are used to get estimates for the lengths (and widths) of the wires.

### 3.1.5 Photolithography and etching

Once the desired wires have been chosen and the positions on the trench are recorded during SEM process, each chip is taken to the class 100 clean room located in the Materials Research Laboratorys Microfabrication and Crystal Growth Facility for photolithography. A hot plate in the clean room is covered with Aluminum foil to help generate a uniform temperature on the surface. A glass microscope slide is placed on the aluminum foil, and the hot plate is turned on to 120 °C. After a couple of minutes when the desired temperature is attained, the chip is placed on the glass slide and heated for ~5 min to evaporate any water vapor that may be on the surface. The chip is then placed in a flow of dry nitrogen for ~5 min to cool down. After a drop of photoresist (Shipley 1805, a positive resist) is placed on top of the chip, it is spun for ~20 seconds at 8000 rpm. After this step the top surface of the chip is uniformly coated with ~5  $\mu\text{m}$  of photoresist 3.5a.

The relatively fast speeds are necessary for our small chips to get an even thin coat of resist as opposed slower speeds used for larger wafers. The chip is then placed back on the glass slide of the hot plate and soft-baked for 2 min at 120 °C. We use a Karl Suss MJB3 Mask Aligner to transfer the image of our mask onto the chip. The wavelength of the UV light used is 365 nm.

After aligning our mask (Cr on glass shaped as in 3.6) by using the markers together with the SEM records, we expose the chip to UV light for 7.5 sec. After exposure, the resist is developed by rinsing in a developer (1 part by volume Shipley 351 Microposit Developer to 4 parts by volume DI water) for ~30 sec (10 seconds after the pattern becomes fully

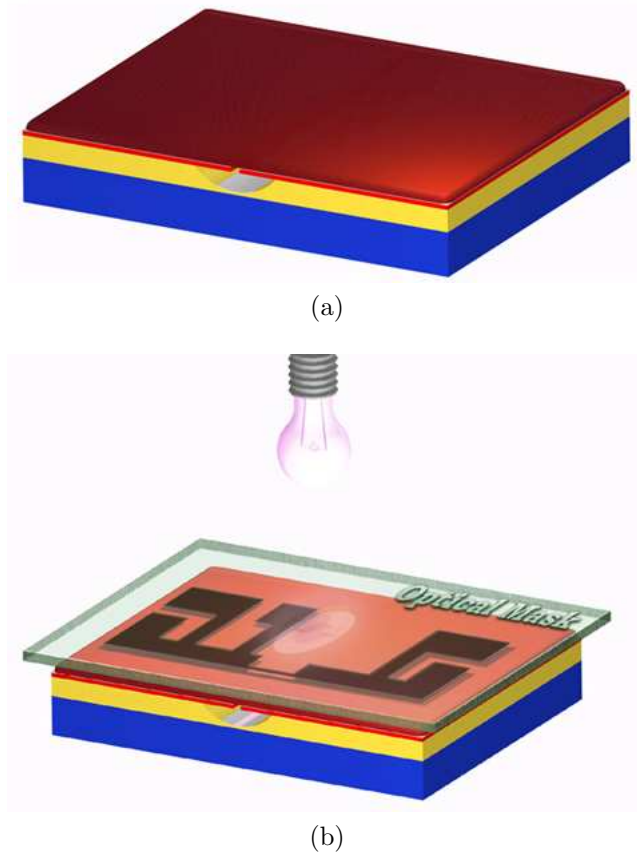


Figure 3.5: Photolithography process: (a) Photoresist is spin-coated onto the entire surface of the substrate. (b) An optical mask is aligned over the substrate and the sample is exposed to UV light. The mask is designed to isolate a single nanowire and simultaneously create an electrode pattern for later measurements.

visible). The chip is then rinsed in DI water for  $\sim 30$  sec to remove all developer. The chip is then dried in a flow of nitrogen, and the chip is viewed under a microscope to inspect the quality and location of the mask. If the mask appears free of major defects (i.e. lines are straight, the width of the thinnest portion does not vary significantly, and the mask has no holes in it, etc.), the chip is placed in 6 %  $\text{H}_2\text{O}_2$  for 10-15 seconds to remove the portions of the MoGe film and MoGe wires that are not protected by the mask. The etch rate of MoGe with 3 %  $\text{H}_2\text{O}_2$  is  $\sim 1$  nm/sec. The photoresist mask is removed by placing the chip in acetone for  $\sim 2$  min. After the mask has been removed, the chip is rinsed in isopropanol for  $\sim 30$  sec and dried in a flow of nitrogen gas. The result after photolithography is shown in 3.6

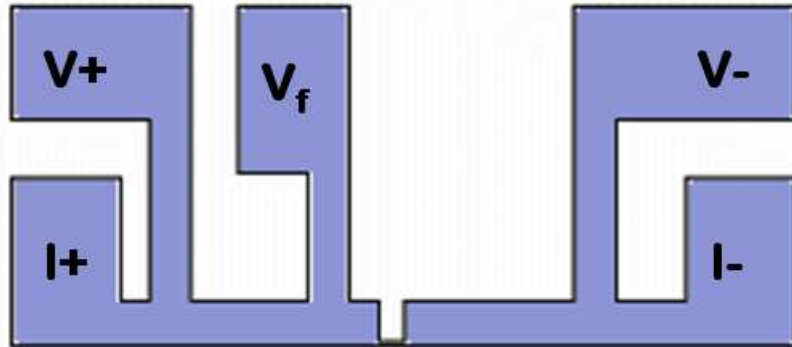


Figure 3.6: The shape of our Cr mask used in photolithography. The thinnest region was made in one of four sizes-5, 10, 15, and 20  $\mu\text{m}$ , and that is the portion that covers the wire. The outermost electrodes(I+, I-) are used to inject a current , and the next inner electrodes (V+, V-) measure the voltage across the wire. There is a fifth electrode ( $V_f$ ) for measurement of the film portion of the pattern.

## 3.2 Measurement of superconducting nanowires

### 3.2.1 Mounting the sample

The sample must be mounted for electrical measurements after the electrodes are patterned on the chip. During this process, it is possible to burn wires by static electric discharges. We do our best to negate this problem by electrically grounding ourselves with a wristband and by spraying anti-static solutions around the work area. We mount the chip on a 6-pin plastic chip carrier. First, the chip carrier is clamped in an electrically grounded vice, and each of the pins on the chip carrier to be used is wetted with solder. Pieces of gold wire (50  $\mu\text{m}$  diameter,  $\sim 1$  cm long) are soldered to the pins of chip carrier. A small piece of double sided sticky carbon tape is placed in the center of the carrier, and the sample is attach to the carbon tape. We use indium dots (avg. dia. 25  $\mu\text{m}$ ) to connect the gold wires to the chip. An indium dot can be placed in a particular location on a sample using the flat end of a small drill bit or the end of a metal lead. We place an indium dot on each pad of the electrode pattern (Fig. 3.6) and press down slightly to flatten the indium. Using tweezers,

a gold wire attached to a pin is moved over the indium dot, and a second indium dot is flattened over the gold wire. The result is a gold wire sandwiched between two indium dots and connected to a pad. This helps maintain a good electrical contact and minimizes the possibility that the gold wire will become detached when the sample is cooled.

### 3.2.2 Cryostats

Once all the pads on the chips to be used are connected to the chip carrier using the gold wires, the chip carriers are inserted into a socket on one of three cryostats. One of the cryostats is designed for inserting samples into  $^4\text{He}$  transfer dewars, and we can measure down to temperatures of  $\sim 1.35$  K using this  $^4\text{He}$  system. Another cryostat is a standard  $^3\text{He}$  cryostat, and we can measure down to  $\sim 0.27$  K using this  $^3\text{He}$  system. The dewar for the  $^3\text{He}$  system is also equipped with a magnet allowing us to generate magnetic fields up to 9 T. For measurements at the lowest temperatures, an insert was used for a top loading Oxford Instruments Kelvinox dilution refrigerator that is located in Dale van Harlingens laboratory and maintained by his research group.

The  $^4\text{He}$  system is the most basic system that we use for measurements as it is easy to use, inexpensive and the sample can be quickly measured down to 1.35 K. The  $^4\text{He}$  system was built by U. C. Coskun in our laboratory. The details about this dipstick can be found in Ref. [52]. In the dipstick, a socket for the chip carriers is located at the bottom of the dipstick. There are ten measurement leads that run from the room temperature portion of the stick down to the bottom and are connected thermally to a copper block by silver paste. The silver paste also serves as a filter for high frequency noise. The temperature is measured by measuring the resistance of a calibrated Cernox thermometer, to which four of the measurement leads are attached, located next to the socket on the copper plate. A copper can covers the sample and thermometer, and it is wound with resistive twisted pair wire (Stableohm) which serve as a heater. A stainless steel pipe covers the length of the dipstick so that a vacuum can be created around the sample. Once a sample to be measured

has been placed in the socket, the air in the dipstick is evacuated at room temperature, and a small amount of He gas (as exchange gas) is introduced to help in the cooling process. The bottom portion of the stick is immersed in liquid nitrogen until it cools to 77 K. By cooling first in liquid nitrogen, we save on the amount of liquid helium necessary to cool the dipstick to 77 K from room temperature. We then transfer the dipstick into a 35-liter capacity liquid He transfer dewar filled with  $\sim 2$  liters of liquid helium and let it cool. To attain temperatures down to  $\sim 1.35$  K, we use a vacuum pump to slowly remove the He vapor above the liquid helium bath which decreases the boiling point of liquid He. By pumping on only a small volume of liquid helium ( $\sim 2$  liters), we are able to quickly reduce the temperature to  $\sim 1.4$  K in about a couple of hours. Once at this base temperature, we can measure our samples for  $\sim 12$  hours before the liquid helium has completely evaporated. Also, once at the base temperature the sample can be heated up to some desired temperature with the help of the heater and a current source.

To achieve lower temperatures below 1.35 K for measurements, we use  $^3\text{He}$  system purchased from Janis Research Company. In this system a  $\sim 2$  mm wide tube connects the  $^4\text{He}$  bath to a 1 K pot, allowing liquid  $^4\text{He}$  to enter at a controllable rate (with the help of a valve). A vacuum pump can cool the pot to  $\sim 1$  K by removing the  $^4\text{He}$  vapor. The 1 K pot surrounds an inner tube containing  $^3\text{He}$  gas, which begins to condense once the 1 K pot reaches a temperature below 2 K. The condensed  $^3\text{He}$  liquid collects in the  $^3\text{He}$  pot just above the sample. Once all the  $^3\text{He}$  is condensed, the  $^3\text{He}$  vapor above it can be “pumped” away by the sorption pump charcoals that bind He vapor when they are cold. By using this sorption pump, we are able to remove the vapors without allowing  $^3\text{He}$  gas to leave our system, and we can achieve temperature of  $\sim 0.27$  K. High resistance wires connect the room temperature portion of the cryostat to the 1 K pot to minimize thermal coupling. More high resistance wires connect from the 1 K pot to the  $^3\text{He}$  pot. A copper attachment connects the  $^3\text{He}$  pot and sockets for the thermometer and sample. Long low resistance wires are wound around the copper attachment connected to the  $^3\text{He}$  pot and covered with silver paste as

a filter. These wires are then connected to the sample carrying sockets. Two sockets exist in this system for different magnetic field orientations (perpendicular and parallel to the film). The side socket which can hold up to two chips has a calibrated ruthenium oxide thermometer measured in a four-probe configuration. As mentioned before, the dewar for this system is equipped with a magnet, which can generate fields up to 9 T.

### 3.2.3 Filtering system of $^3\text{He}$ measurement setup

It is essential for us to minimize the high frequency noise (which if of the order of the QPS rate) coming from the outside environment that would interact with the nanowire and lead to noise in the acquired data and can be wrongly interpreted as QPS. In this section we discuss the arrangement of RF filters in our  $^3\text{He}$  measurement setup. The purpose of these filters is to suppress external high-frequency electromagnetic noise, such as the noise originating from cell-phones, radio stations, and also the black-body radiation, which can, if filters are not installed, propagate through the measurement leads and reach the sample and modify the switching current observed in the experiment. Our filters are designed to reduce this noise effect to a negligible level.

Our main filtering stage is a Copper powder filter thermalized at the base temperature (0.29 K). The filter is of the type developed by Martinis, Devoret and Clarke [5]. More details are presented below.

In our system, each signal line has three stages of filtering in series, namely, a  $\pi$ -filter at room temperature and a copper-powder filter (Cu-F) (at the base temperature) and silver-paste filter (Ag-F) (also, at the base temperature). These filters are necessary to suppress noise ranging from low frequency to high microwave frequencies. The compact powder filters (i.e., Cu-F or Ag-F) rely on the skin effect damping for attenuation of high frequencies. At room temperature, commercially available  $\pi$ -filters (Spectrum Control, SCI 1201-066) are placed on each electrical lead before they enter the cryostat. The  $\pi$ -filters are mounted inside an aluminum box (Hammond Manufacturing) which is attached to the top of the cryostat.

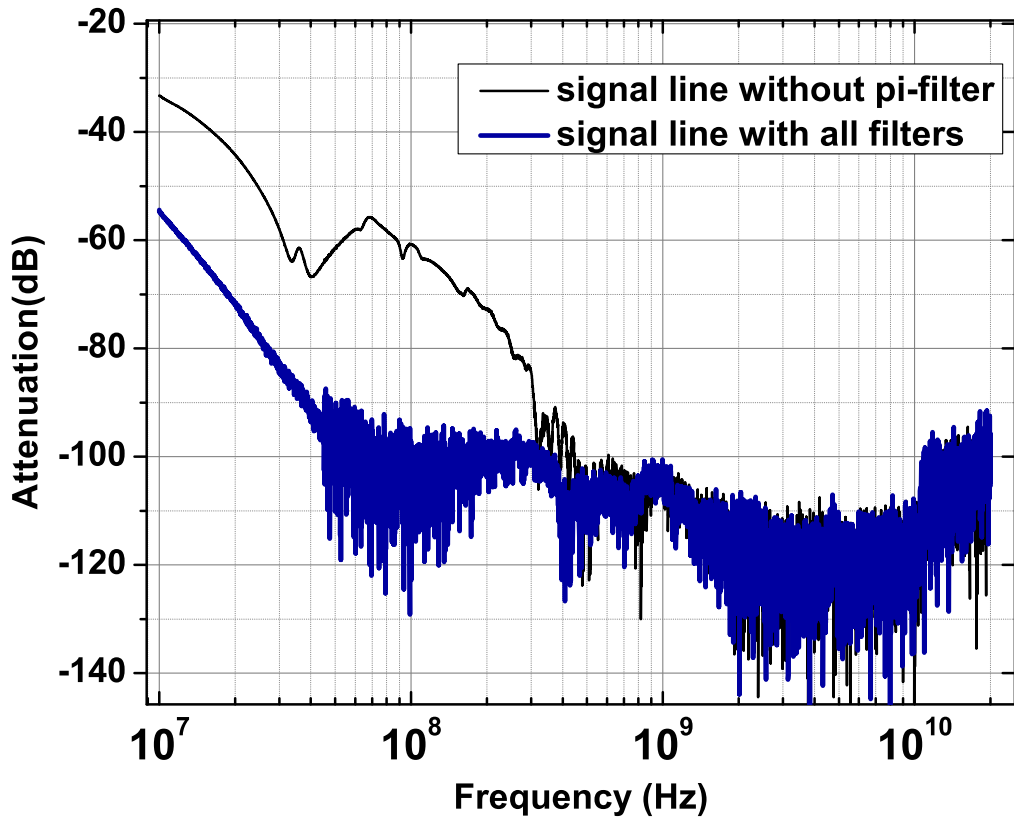


Figure 3.7: Attenuation of a signal line of our  $^3\text{He}$  setup measured at room temperature between 10 MHz and 20 GHz. For measurement of the signal line with all the three stages of filters (blue curve) we find attenuation larger than 90 dB for frequencies higher than 40 MHz. For frequencies higher than 6 GHz (roughly corresponding to our base temperature of  $T \sim 0.29$  K), we find the attenuation to be larger than 110 dB and the signal falls below the noise level of our network analyzer. The attenuation of the signal lines without the  $\pi$ -filter is also shown (black curve). The  $\pi$ -filters provide an attenuation of 20 dB for frequencies larger than 10 MHz (rated 7 dB cut-off frequency of 3 MHz).

The  $\pi$ -filters used are low-pass filters with a rated 7 dB cut-off frequency of 3 MHz. As shown in Fig. 3.7, for frequencies larger than 10 MHz, the measured attenuation of these  $\pi$ -filters is more than 20 dB. Our copper powder filters are fabricated using three feet of coiled insulated Constantan wire [Cu(55 %)Ni(45 %) alloy, resistance 18.4  $\Omega$ /feet, diameter 0.004 inch] embedded in a mixture of copper powder (-325 mesh, Alfa Aesar) and epoxy (Stycast #1226, Emerson and Cuming). Similarly, the silver paste filters are fabricated using three feet of coiled insulated Constantan wire (the same wire) in silver paste (Fast drying silver paint, Ted Pella Inc.). By measuring the signal lines with all the filters, using a vector

network analyzer (Agilent N5230A), we found the attenuation to be larger than 100 dB for frequencies higher than 1 GHz (3.7). Any frequency above 6.25 GHz (which corresponds to a temperature of 0.3 K) is attenuated by more than 110 dB and falls below the noise floor of our network analyzer. This level of attenuation is similar to the attenuation used in previous experiments on MQT, see for example, Ref.[5] .

### 3.2.4 Transport Measurements

We carry out electrical transport measurements in a four-probe configuration using one of the three cryostats described in the previous subsection. In this study, most of the measurements for this work was carried on the  $^3\text{He}$  cryostat as low bath temperatures allow us to study the effect of quantum fluctuations dominant over thermal fluctuations at temperatures much lower than the critical temperatures of the nanowires.

In our measurement scheme, an ultra low distortion function generator (Stanford Research Systems DS 360) applies a voltage, which is passed through a known standard resistor (typically 1 M $\Omega$ ). The circuit diagram for the measurement setup is shown in Fig. 3.8 [29]. This large resistance of the standard resistor compared to the resistance of the nanowire effectively makes the measurements current-biased. By measuring the voltage across the resistor amplified through battery-powered pre-amplifier (either Princeton Applied Research model 113 or Stanford Research Systems model SR 560) connected to a data acquisition card (National Instruments model PCI-MIO-16XE-10), we are able to measure the current we are applying to the sample. Then, using another pre-amplifier and slot on the data acquisition card, we measure the voltage across the sample. We measure the resistance of the thermometer with a Keithley 2000 multimeter ( $^4\text{He}$  system) or a Lakeshore 370 AC Resistance Bridge ( $^3\text{He}$  system) with a four-probe configuration. In this manner, we can measure voltage as a function of current,  $V(I)$ . We define the resistance of the sample  $R$  as the slope of the  $V(I)$  curve in the limit of zero current. Typically, we use an AC measuring current of amplitude 5 nA at a frequency of  $\sim 12$  Hz centered at zero bias for measuring resistance.

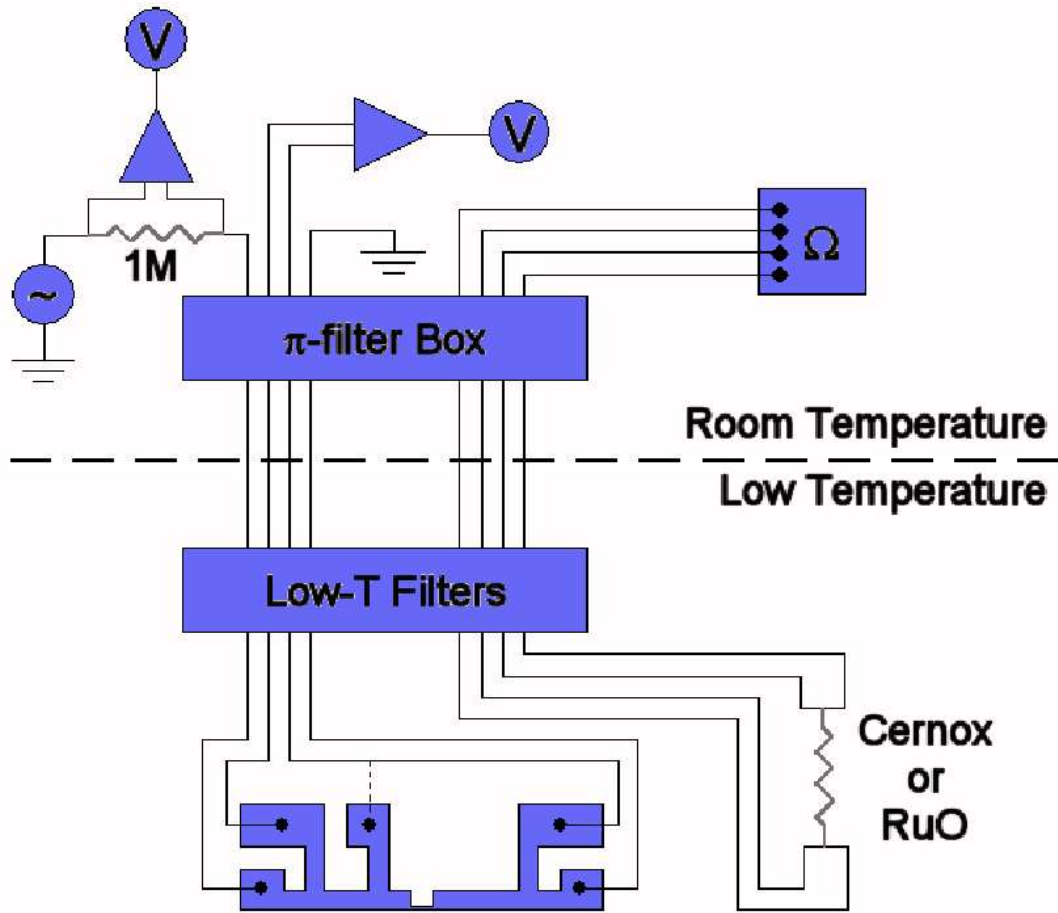


Figure 3.8: Schematic of the measurement setup for transport measurement of nanowires [29]. The sample is current-biased by a function generator with a 1 M $\Omega$  resistor in series. The current is measured by measuring the voltage across the standard resistor using a preamp. The sample voltage is measured using another preamp. The temperature of the sample is measured using a calibrated thermometer measured in a four-probe configuration. To reduce noise  $\pi$ -filters are employed at room temperature and Cu powder and Ag paste filters are used at the base temperature.

Using a measuring current that is too low leads to a noisy measurement of  $R$ , and using a measuring current that is too large gives an incorrect value of  $R$  if the  $V(I)$  curve is no longer linear at high bias.

For measuring a  $V(I)$  curve, the function generator is set at slow frequency of  $\sim 5$  mHz and large amplitude that gives bias currents of the order of few  $\mu\text{A}$  (The amplitude of this current is modulated depending upon the critical current of the nanowire). During these

measurements currents much larger than the critical current of the wires have a risk of burning the wires. We also measure  $dV(I)/dI$  by measuring the slope of the  $V(I)$  curve in a narrow range centered around a nonzero bias current. We can also measure any of these parameters while altering magnetic fields and temperatures. For temperatures low enough for a sample to be superconducting, we can also measure switching current  $I_{SW}$  (the current at which the sample jumps from a low-voltage state to a resistive state) and retrapping current  $I_R$  (the current at which a resistive wire returns to a low-voltage state). The temperatures can be fixed during these measurements through a LabVIEW controlled feedback loop ( $^4\text{He}$  system) or a feedback loop (PID) controlling the heater output by the Lakeshore device ( $^3\text{He}$  system).

# Chapter 4

## Low-bias measurements of superconducting nanowires

In this chapter I will discuss about low-bias  $R(T)$  measurements performed on single nanowires samples. By low-bias measurements we mean that the applied currents are much smaller than the thermodynamic critical current such that the current-voltage ( $V(I)$ ) characteristics show Ohmic behavior. I will also discuss that for the superconducting wires the resistive transitions can be well explained by theory of thermally activated phase slips (TAPS). To obtain the fits I have used two models of TAPS, namely, Little fit and Langer, Ambegaokar, McCumber and Halperin (LAMH) fit. An agreement of the resistance measured in an experiment with that predicted in LAMH model would thus indicate homogeneity of the measured wire. For the insulating wires only the  $R(T)$  data will be shown for a few measured samples. For the insulating wires only the  $R(T)$  data will be shown for a few measured samples .

### 4.1 Resistance vs. temperature $R(T)$ curves

The resistance vs, temperature curve for nanowire measured in the  $^4\text{He}$  measurement set up is shown in Fig. 4.1. As the wire is seamlessly connected in series with the film electrodes we observe two resistive transitions, one corresponding to the film electrodes and the other corresponding to the nanowire. The rather sharp transition ( at  $\sim 6$  K) is due to the film electrodes becoming superconducting. The second transition (around  $\sim 3.5$  K) is due to the nanowire going “superconducting”. Throughout this study the film and wire were sputtered together, its found that the film always had a higher  $T_C$  than the wire. The resistance of the wire diminishes by three orders of magnitude and the resistance can be measured down to

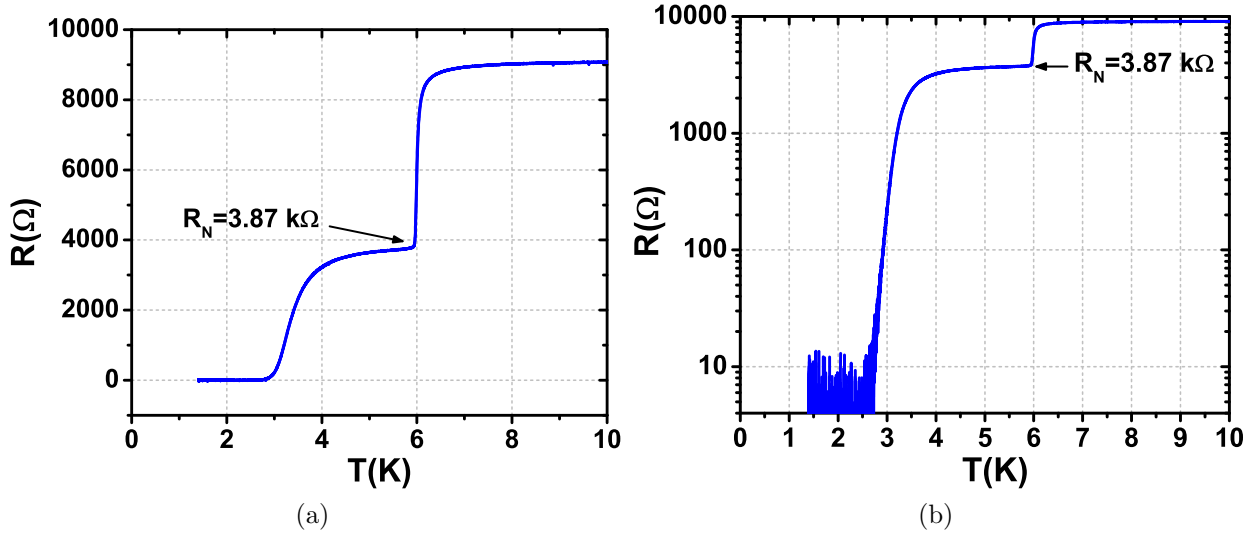


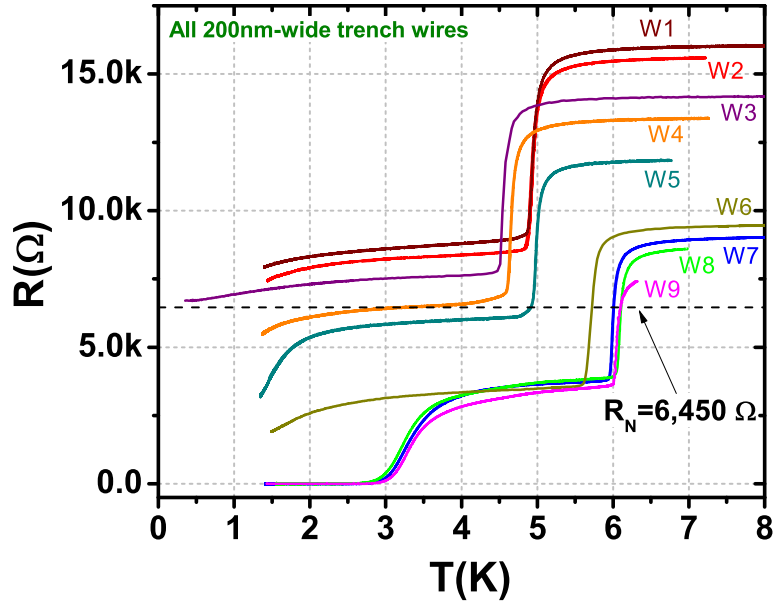
Figure 4.1: (a)  $R(T)$  curve for a MoGe nanowire sample. The higher temperature transition corresponds to the superconducting transition of the thin film electrodes. The width of the film transition is  $\sim 0.1$  K. The broader transition at lower temperature corresponds to that of the nanowire. The width of the wire transition is  $\sim 1$  K. The normal state resistance  $R_N$  of the wire is taken to be the resistance measured just below the transition temperature of the film. The  $R_N$  of the wire is indicated by the arrow. (b) log-linear plot of the same  $R(T)$  data as shown in (a). The resistance of the wire can be measured down to a few  $\Omega$ s, below which the resistance falls below the noise-floor of the setup.

a few  $\Omega$ , below which the measurement falls below the noise floor of our setup (Fig. 4.2b).

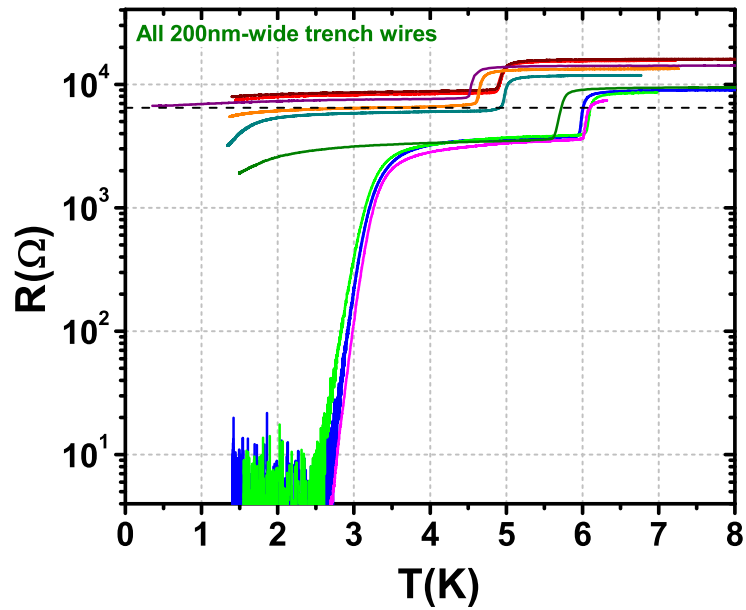
The resistance of the sample measured just below the temperature at which the thin film electrodes become superconducting is defined as the normal state resistance  $R_N$  of the wire. This  $R_N$  for the sample is indicated in Fig. 4.2a and 4.2b by the arrows. Observation of a single resistive transition of the wire reflects the fact that the wire is homogeneous or free from large variations in the cross-sectional area which would lead to multiple steps in the resistive transition of the wire as shown in Ref. [43].

The  $R(T)$  behavior of the nanowires allows us to distinguish between superconducting and insulating nanowires. A set of  $R(T)$  curves for such nanowires is shown in Fig. 4.2. All the wires shown are fabricated on trenches that were 200 nm wide. Thus all the wires had similar length but their normal state resistance varied due to different thicknesses of the sputtered MoGe. It was found that all the wires can be categorized into two types, i. e.,

“superconducting” and “insulating” wires [28, 14]. The wires W6-W9 have  $R_N < R_Q$  where  $R_Q = h/4e^2 \approx 6,450 \Omega$  (indicated by the black horizontal dotted line) are superconducting around 3 K. The wires W5 and W6 also have  $R_N < R_Q$  and do so superconducting trend measured down to  $\sim 1.4$  K (the base temperature of  $^4\text{He}$  setup). The wires W1-W4 have  $R_N > R_Q$ , and show insulating behavior [28, 14]. The wire W5 has a resistance  $R_N = 7.08 k\Omega > R_Q$  but shows signs of superconducting behavior down to the base temperature of 1.4 K. This wire needs to be measured to lower temperatures to be concluded as superconducting or insulating. This set of wires corroborate the observation of the superconductor-insulator transition previously observed in nanowires [13, 43, 14]. It is noteworthy that, for all the wires (superconducting or insulating) measured  $R(T)$  curves show a single film transition and single wire transition. This indicates that the film and the wires are homogeneous in nature. One would expect multiple transitions for the wire if it is not homogeneous [43]. This is very crucial for us make sure that the wire is free from morphological defects before we proceed to further investigation using switching current distribution measurements.



(a)



(b)

Figure 4.2: (a)  $R(T)$  curves for 9 different MoGe nanowires (W1-W9) representing superconductor-insulator transition (SIT). For all wires, the higher temperature transition corresponds to the superconducting transition of the thin film electrodes. The width of the film transition is  $\sim 0.1$  K for all superconducting wires. (b) log-linear plot of the same  $R(T)$  data as shown in (a). The resistance of the superconducting wires can be measured down to a few  $\Omega$ s, below which the resistance falls below the noise-floor of the setup.

## 4.2 Comparison with Little's and LAMH fits

In this section we will first compare the measured  $R$ - $T$  data with the model of phase slip proposed by Little. The derivation for the expression of  $R_{Little}$  was done in Chapter 2 and

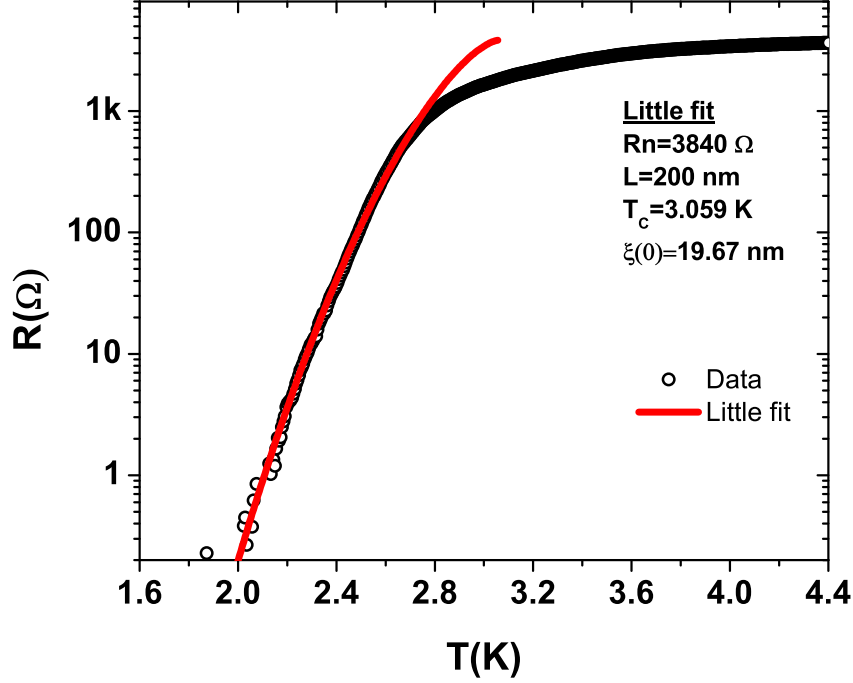


Figure 4.3: Little's fit to the  $R$ - $T$  data for a nanowire shown in a log-linear scale. The open circle is zero-bias resistance measured and the red line is the the fit to the Little model using Eq. 4.1. The fitting parameters are critical temperature  $T_C$  and zero temperature coherence length  $\xi(0)$ . The normal state resistance  $R_N$  is taken to be resistance measured at a temperature just below the film transition temperature  $T_{C, film}$  (not shown here). The length of the wire  $L$  is determined from the SEM image of the wire. All the wire parameters and the fitting parameters are indicated in the graph. The Little model shows good agreement with the observed wire transition.

here the expression used for fitting will be just restated. To fit the  $R$ - $T$  data, the expression used is,

$$R(T) = [R_{Little}^{-1}(T) + R_N^{-1}]^{-1} \quad (4.1)$$

where  $R_N$  is the normal state resistance of the wire. The  $R_{Little}$  is given by

$$R_{Little} = R_N \exp\left(\frac{\Delta F(T)}{k_B T}\right) \quad (4.2)$$

where,  $\Delta F(T)$  is the free energy barrier for a phase slip is expressed as,

$$\Delta F(T) = \frac{8\sqrt{2}}{3} \left( \frac{H_C^2(T)}{8\pi} \right) A\xi(T) \quad (4.3)$$

where,  $H_C(T)$  [53] and  $\xi(T)$  [30] are given by,

$$H_C(T) = H_C(0) [1.73(1-t) - 0.40087(1-t)^2 - 0.33844(1-t)^3 + 0.00722(1-t)^4] \quad (4.4)$$

$$\xi(T) = \xi(0) \left[ \frac{\sqrt{(1-t^4)}}{1-t^2} \right] \quad (4.5)$$

where  $t = T/T_C$ . Also, in terms of wire parameter the free energy barrier at zero temperature is,

$$\Delta F(0) = \frac{8\sqrt{2}}{3} \left( \frac{R_Q}{R_N} \right) \left( \frac{L}{\xi(0)} \right) k_B T_C \quad (4.6)$$

Hence, the temperature dependent free energy barrier (as in Eq. 4.3) in terms of wire parameter now becomes,

$$\begin{aligned} \Delta F(T) = & \frac{8\sqrt{2}}{3} \left( \frac{R_Q}{R_N} \right) \left( \frac{L}{\xi(0)} \right) k_B T_C \\ & \times [1.73(1-t) - 0.40087(1-t)^2 - 0.33844(1-t)^3 + 0.00722(1-t)^4]^2 \left[ \frac{\sqrt{(1-t^4)}}{1-t^2} \right] \end{aligned} \quad (4.7)$$

To do the fit, critical temperature  $T_C$  and zero temperature coherence length  $\xi(0)$  are used as fitting parameters. The normal state resistance  $R_N$  is taken to be resistance measured at a temperature just below the film transition temperature  $T_{C, film}$  (not shown here). The length of the wire  $L$  is determined from the SEM image of the wire. A fitting to the measured  $R$ - $T$  data is shown for a wire of  $L = 200$  nm and  $R_N = 3840 \Omega$  in Fig. 4.3. All the wire parameters and the fitting parameters are indicated in the graph. The Little's model can be used efficiently to explain the wire transition.

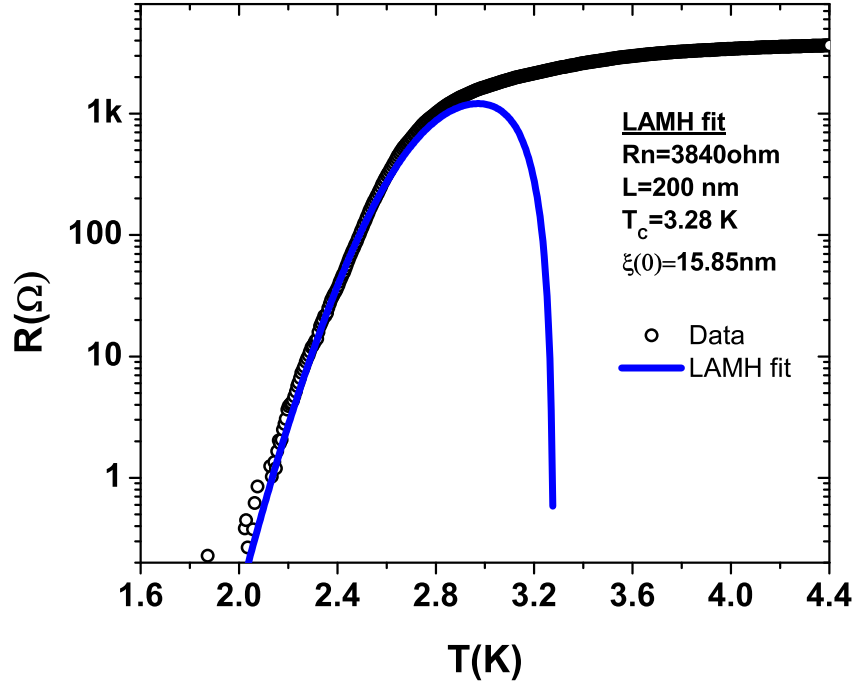


Figure 4.4: LAMH fit to the  $R$ - $T$  data for a nanowire shown in a log-linear scale. The open circle is zero-bias resistance measured and the blue line is the the fit to the LAMH model using Eq. ???. The fitting parameters are critical temperature  $T_C$  and zero temperature coherence length  $\xi(0)$ . The normal state resistance  $R_N$  is taken to be resistance measured at a temperature just below the film transition temperature  $T_{C, film}$  (not shown here). The length of the wire  $L$  is determined from the SEM image of the wire. All the wire parameters and the fitting parameters are indicated in the graph. The LAMH model shows good agreement with the observed wire transition.

Next the same data will be fitted to the model of TAPS developed by Langer, Ambe- gaokar, McCumber, Halperin (LAMH) that incorporates thermally activated phase slips. The derivation of the expression for  $R_{LAMH}$  was done in Chapter 2 and here the form of  $R_{LAMH}$  will be restated. To fit the  $R$ - $T$  data we have used the expression,

$$R(T) = [R_{LAMH}^{-1}(T) + R_N^{-1}]^{-1} \quad (4.8)$$

where  $R_N$  is the normal state resistance of the wire. The  $R_{LAMH}$  is given by

$$R_{LAMH}(T) = \frac{\pi \hbar^2 \Omega(T)}{2e^2 k_B T} \exp\left(-\frac{\Delta F(T)}{k_B T}\right) \quad (4.9)$$

where  $\Omega(T)$  is the attempt frequency given by,

$$\Omega(T) = \left( \frac{L}{\xi(T)} \right) \sqrt{\left( \frac{\Delta F(T)}{k_B T} \right)} \left( \frac{1}{\tau_{GL}} \right) \quad (4.10)$$

with  $\tau_{GL} = [\pi\hbar/8k_B(T_C - T)]$  is the GL relaxation time. The form of  $\Delta F(T)$  is the same as used for Little's fit (Eq. 4.7).

To do the fit the fitting parameters are critical temperature  $T_C$  and zero temperature coherence length  $\xi(0)$ . The normal state resistance  $R_N$  is taken to be resistance measured at a temperature just below the film transition temperature  $T_{C, film}$  (not shown here). The length of the wire  $L$  is determined from the SEM image of the wire. A fitting to the measured  $R$ - $T$  data (as used in Little fit in Fig. 4.3) is shown for the wire of  $L = 200$  nm and  $R_N = 3840 \Omega$  in Fig. 4.4. All the wire parameters and the fitting parameters are indicated in the graph. It is found that the LAMH model can efficiently explain the wire transition.

Its found that both the Little and LAMH model explain the resistive transition of the wire very well. But the fitting parameters  $T_C$  and  $\xi(0)$  for both the fits are slightly different. Nevertheless, the resistive transition captured in the zero-bias measurement of wires are explained by thermally activated phase slips (TAPS). There is *no evidence* of quantum phase slips in these measurements.

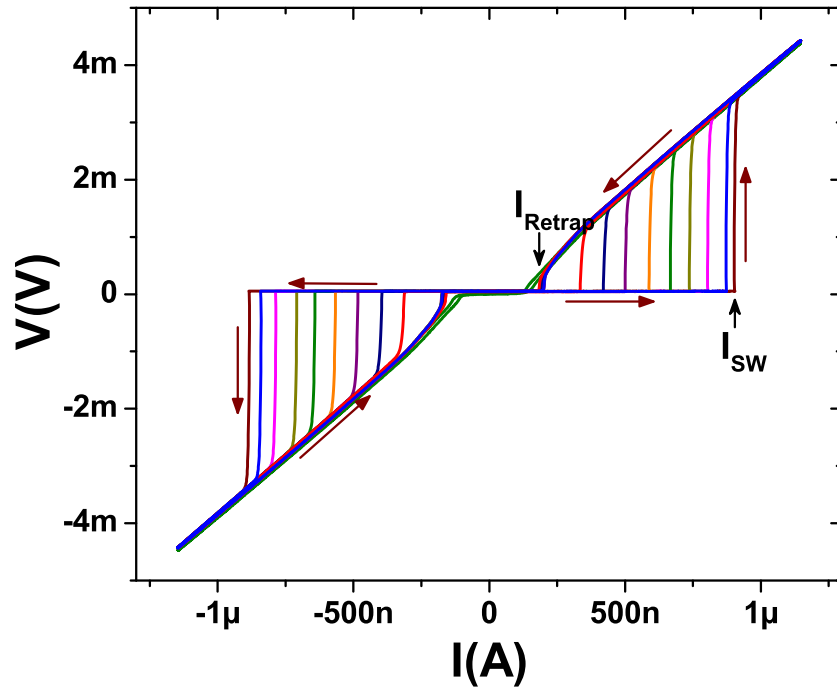
# Chapter 5

## Switching current measurements of superconducting nanowires

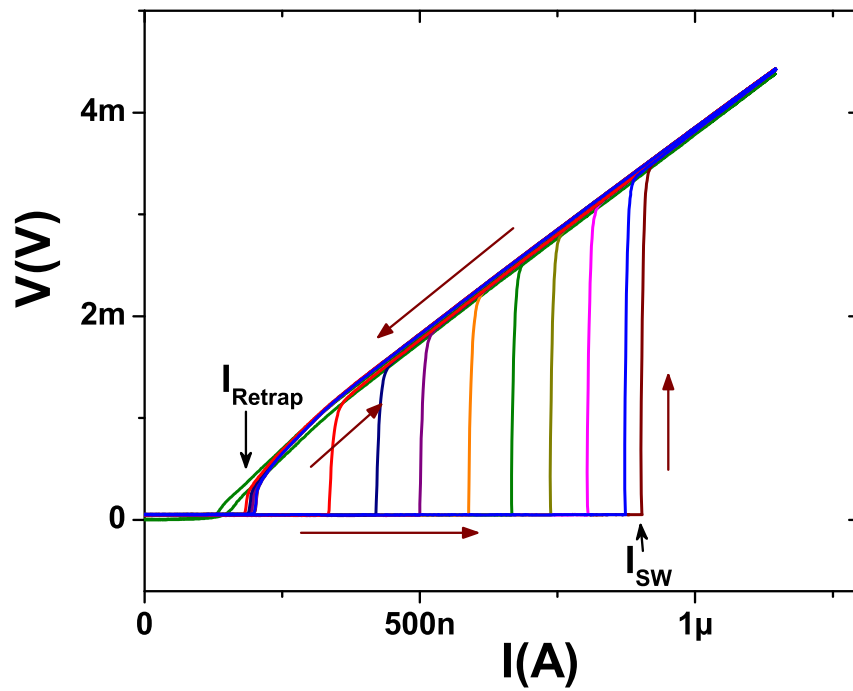
### 5.1 High-bias $V(I)$ measurements

A representative set of voltage-current characteristics  $V(I)$ , measured at various temperatures, is shown in Fig.5.1. These data show that, as the bias current is swept from low to high, the system exhibits an abrupt transition from a zero or extremely low-voltage state (i.e., a superconducting state) to a high-voltage state (i.e., a normal state) in which the resistance is close to  $R_N$  (22). We call the current at which switching occurs the switching current  $I_{SW}$ . Similarly, as the bias current is swept from high to low, the state reverts to being superconducting, doing so at a retrapping current  $I_R$ . We indicate these currents in Fig. 5.1 for data taken at 0.3 K. As can be seen from Fig. 5.1, our nanowires are strongly hysteretic: there is a regime of currents within which the wire is bistable (i.e., two voltage states, one superconductive and one normal, are locally stable), and one of the two states is realized depending upon the current history.

We find that the switching current of a nanowire  $I_{SW}$  increases with decrease in the temperature while the retrapping current  $I_R$  increases by a very small amount as the temperature is decreased. This essentially leads to the increase of the hysteresis as the temperature is decreased (as shown Fig. 5.1). At high temperatures when the wire is in a normal state the  $V(I)$  curves of a nanowire is linear or ohmic in nature without any hysteresis loop. Also at high temperatures, we see voltage “tails” before the the wire switches to the normal state. This is shown in the  $V-I$  curves shown in Fig. 5.2. These voltage tails appear due to many phase slips occurring in the wire before it switches to the resistive state with a resistance



(a)



(b)

Figure 5.1: (a)  $V(I)$  curves for a MoGe nanowire sample at various temperatures. The switching current  $I_{SW}$  and the retrapping current  $I_R$  are indicated for the curve measured at 0.277 K. The temperatures are 0.27 K (highest  $I_{SW}$ ), 0.4 K, 0.6 K, 0.8 K, 1.0 K, 1.2 K, 1.4 K, 1.6 K, 1.8 K, 2.34 K. (b) The zoomed in plot of the curves shown in (a) for clarity.

close to the normal state resistance  $R_N$  of the wire. From the set of curves in Fig. 5.2 it is evident that the voltage tails increase in magnitude with increase in temperature. These voltage tails fall below the noise floor of our measurement for low temperatures and the switching transition is sharp without any observable tails (e.g. for the curve measured at 2.34 K in Fig. 5.2). We also note that the voltage increases roughly in an exponential manner before the wire switches to the normal state.

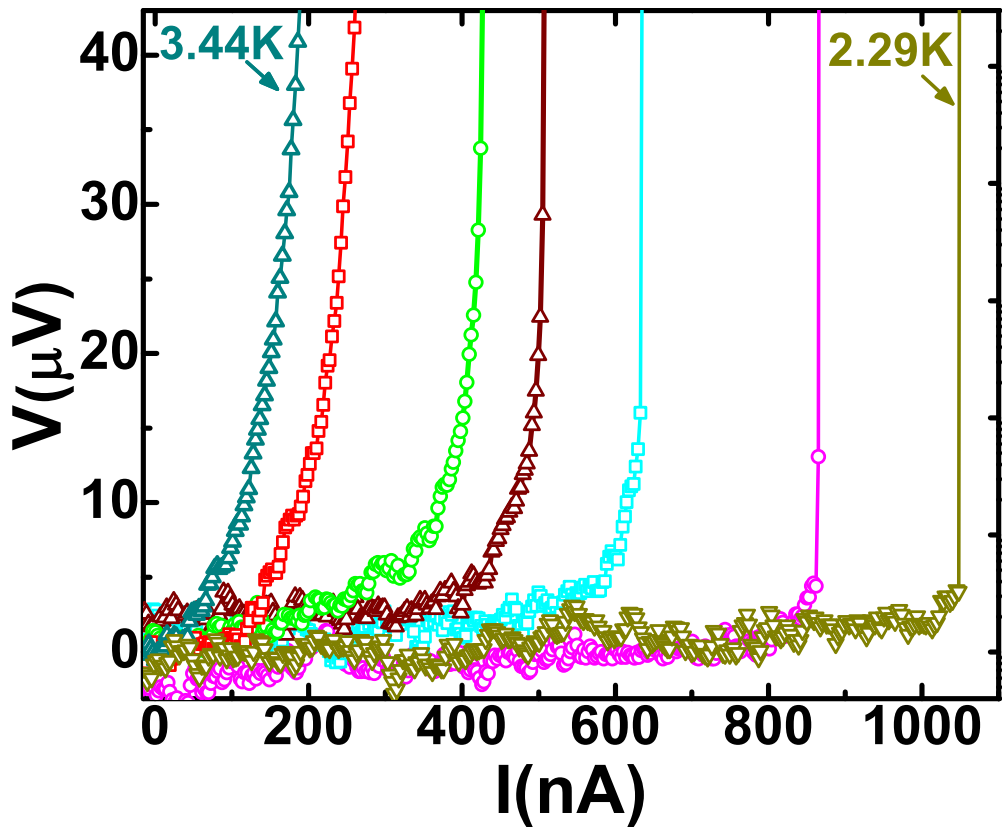


Figure 5.2:  $V(I)$  curves for several temperatures illustrating the “voltage tails” observed before switching at high enough temperatures. The temperatures are  $T = 3.44$  K (left most), 3.33 K, 3.11 K, 3.00 K, 2.85 K, 2.49 K, 2.29 K (right most). At high temperatures, when the voltage tails are measurable, the voltage increases exponentially with bias current before the switch.

Hysteresis behavior is found in several other systems including macroscopic superconducting filaments and under-damped Josephson junctions [24]. In superconducting filaments the hysteresis behavior is explained in terms of self heating hotspots, which can be can be

used as the basis for the hot-electron bolometers [54]. In under-damped Josephson junction system the hysteresis is attributed to the run-away and retrapping of the phase particle in the tilted washboard potential of the Josephson junction without considering any heating effect [30]. Our wires show hysteresis even though they are overdamped and many phase slips occur at high temperatures before the wire switches to the normal state. Tinkham and co-workers [54] have considered the effect of phase slip in heating the wire. They showed that the heat released during a phase slip process is not instantaneously dissipated but, rather leads to alterations in local temperature of the quasi-one-dimensional system and resulting flow of heat, which feed back to influence the phase slip kinetics. This feedback leads to a switching bistability of the system involving a pair of mesoscopic states. One of these states is essentially superconducting, low-voltage state and the other one is a more highly resistive, high-voltage state. The rarity of the phase slips in the essentially superconducting state mean that very little Joule heating takes place, which favors the persistence of the state. However, the energy liberated by concentrated bursts of phase slips can Joule-heat the system enough to weaken the superconductivity, and, via this feedback loop, lead to the essential destruction of the superconductivity and the maintenance of the more strongly Joule-heated, more highly resistive state.

## 5.2 Stochasticity of switching currents

We observe that even if the bath temperature  $T$  and the bias-current sweep protocol is kept the same the measured switching current  $I_{SW}$  varies from run to run. On the other hand, the retrapping current  $I_R$  is reproduced accurately within the experimental resolution. Hence, the the switching current is statistically distributed and does not have a sharp value. This a reflection of the collective dynamics of the superconducting condensate in the nanowire. The condensate can be visualized as a fluctuating entity, evolving stochastically in time and, at random instants undergoing phase slip events. the goal of this thesis work is to understand

the behavior of these distributions of switching currents, and from this gain insight into the thermal and quantum phase-slip rates at low temperatures, not studied in previous works on superconducting nanowires.

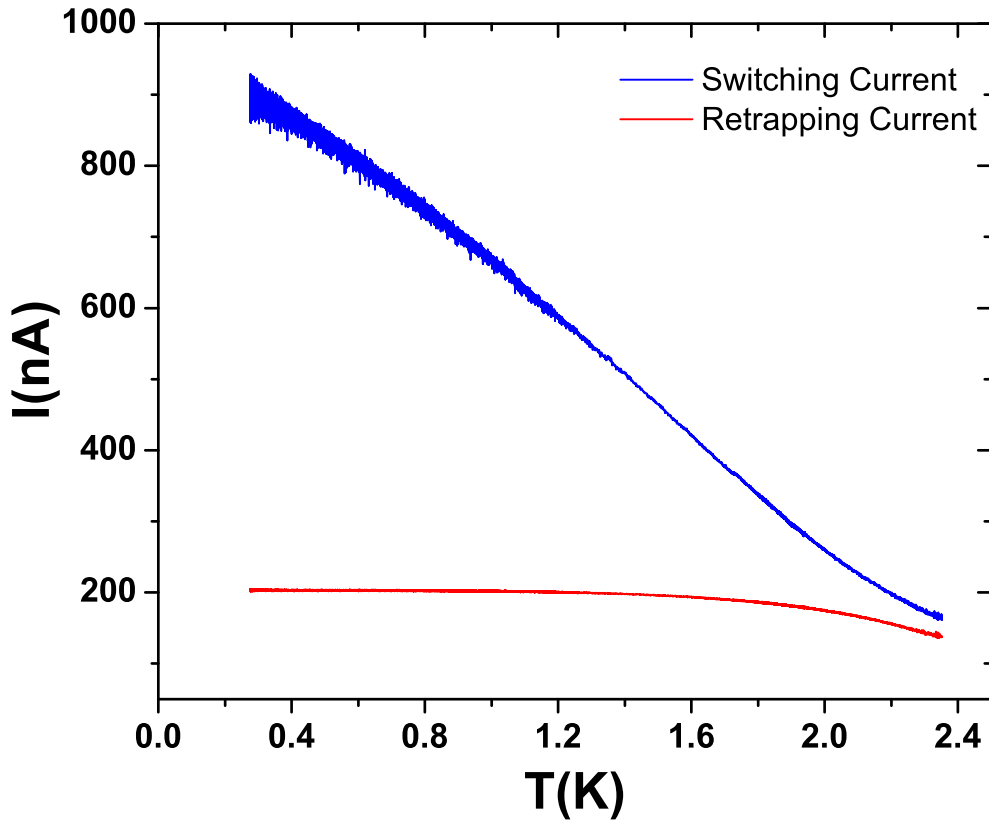


Figure 5.3: The switching current  $I_{SW}$  and retrapping current  $I_R$  measured as the temperature is decreased. The mean switching current increases as the temperature is decreased. Also the width of the fluctuation of the switching current increases with decrease in temperature. The width of the retrapping current distribution remains almost constant within the experimental resolution of  $\sim 0.5$  nA.

In Fig. 5.3 we have shown the measured switching current and retrapping currents of a MoGe nanowire as the sample was being cooled from 2.4 K to 0.3 K in our  $^3\text{He}$  setup. As the temperature is decreased the mean switching current increases. At each temperature the measured switching current varies from measurement to measurement which is reflected in the width of the measured curve. We notice a feature in the graph that the width of

the fluctuation of the switching current is increasing with decrease in temperature. This is rather counter-intuitive if we consider that the width of the fluctuations is simply related to thermal fluctuations and one would expect the widths of the fluctuations to decrease as the bath temperature is decreased. On the other hand, the retrapping current has a width which is within the resolution of our measurement (of the order of  $\sim 0.5$  nA). This is expected as fluctuation of switching current reflects the fluctuation of the superconducting condensate while reproducibility of the retrapping current reflects the minimum current level at which the Ohmic resistive state is stable [24].

### 5.3 Switching current distribution measurements

As mentioned above, the stochasticity corresponds to the observation that even when the temperature and current-sweep protocol are kept fixed,  $I_{SW}$  varies from run to run, resulting in a distribution of switching currents  $P(I_{SW})$ , as was first studied for Josephson junctions by Fulton and Dunkleberger (FD) [55]. Such distributions, obtained at various temperatures, reflect the underlying, stochastically-fluctuating, collective dynamics of the condensate, and therefore provide a powerful tool for shedding light on the nature of the quasi-1D superconductivity. Indeed, one would expect the distribution width to scale with the thermal noise, and hence to decrease, as the temperature is reduced [55]; and to saturate at low temperature where thermal fluctuations are frozen out and only quantum fluctuations are left [5]. A representative set of switching current distribution measurement data is shown in Fig. 5.4. To obtain  $P(I_{SW})$  at a particular temperature, we applied a triangular-wave current (sweep rate  $125.5 \mu\text{A}/\text{sec}$  and amplitude  $2.75 \mu\text{A}$ ), and recorded  $I_{SW}$  for each of 10,000 cycles. We have plotted the obtained 10,000 for each temperature in the form of a histogram. The bin size of the histograms is 3 nA. For the data shown for three temperatures 0.3 K, 1.0 K, 2.0 K. We find that the mean switching current decreases with increase in temperature. One interesting trend we observe is the *decrease* in the widths of the distributions with *increase*

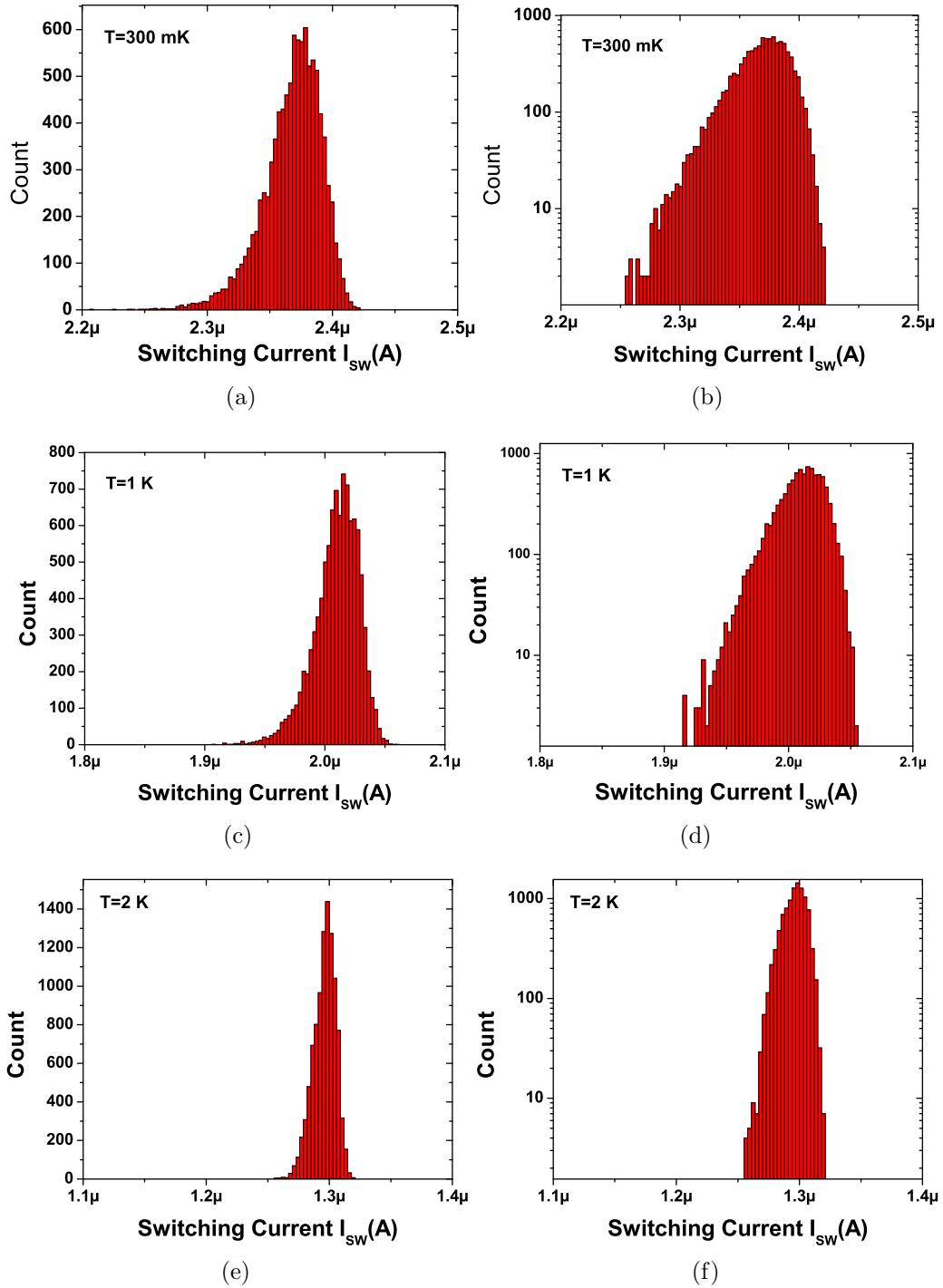


Figure 5.4: Switching current distribution data for three different temperatures,  $T = 300$  mK [(a) and (b)],  $T = 1$  K [(c) and (d)],  $T = 2$  K [(e) and (f)] for sample S1 ( $L = 110$  nm,  $R_N = 2666 \Omega$ ). For each distribution 10,000 measurements were done. The bin size for the histograms is 3 nA. For each distribution the count is shown in linear scale (left graph) and log scale (right graph). For each distribution shown the switching current range shown in the horizontal axes is  $0.3 \mu\text{A}$ .

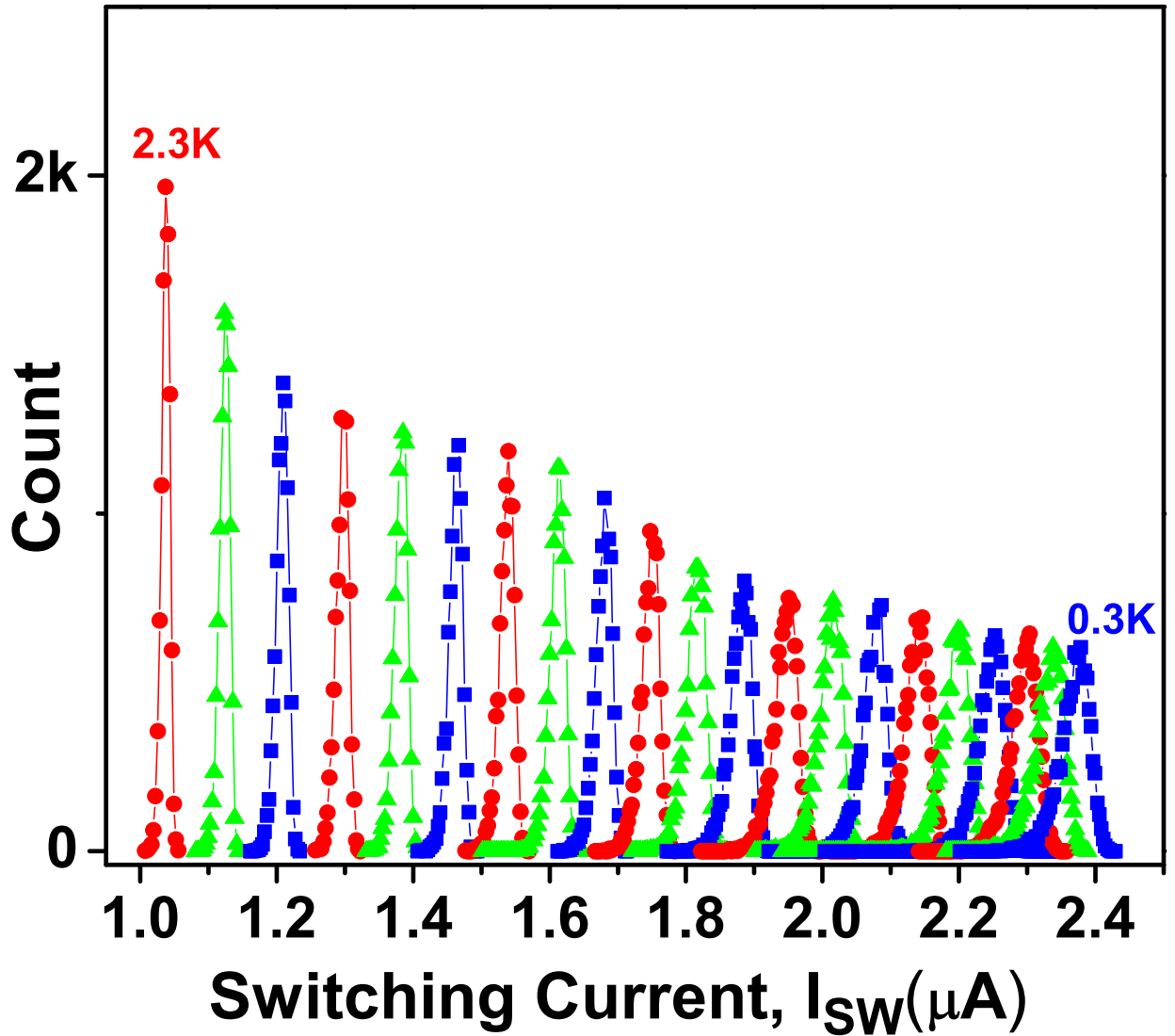


Figure 5.5: Switching current distributions  $P(I_{SW})$  for 21 temperatures between 0.3 K (right most) and 2.3 K (left most) with  $\Delta T = 0.1$  K for sample S1 ( $L = 110$  nm,  $R_N = 2666 \Omega$ ). For each distribution 10,000 switching events were recorded and the bin size of the histograms is 3 nA.

in temperature (as indicated from the data shown in Fig. 5.3). We would like to mention that this observed trend is exact opposite to what was observed by Fulton and Dunkleberger [55] on their measurements on Sn–Sn-oxide–Sn junctions. They found the widths of the distributions to increase with increase in temperatures.

The switching current distributions at 21 temperatures from 0.3 K to 2.3 K with a temperature interval of  $\Delta T = 0.1$  K is shown in Fig. 5.5. A total 10,000 number of measurements were done for each distribution shown. The bin size of each histogram is 3 nA. As the temperature is decreased the height of the distribution is decreasing and the width is increasing. We repeated similar switching current distribution measurements for several nanowire samples. Here we are showing the data for another four MoGe nanowire samples (total 5 nanowires). In Fig. 5.6, the switching current distributions are shown for measurements between 0.3 K and 1.8 K with a temperature interval of  $\Delta T = 0.1$  K for wire S2 ( $L = 195$  nm,  $R_N = 4100$   $\Omega$ ). In Fig. 5.7, the switching current distributions are shown for measurements between 0.3 K and 1.4 K with a temperature interval of  $\Delta T = 0.1$  K for wire S3 ( $L = 104$  nm,  $R_N = 1430$   $\Omega$ ). In Fig. 5.8, the switching current distributions are shown for measurements between 0.277 K and 1.6 K for wire S4 ( $L = 200$  nm,  $R_N = 3900$   $\Omega$ ). The bath temperature for each distribution is indicated in the graph.

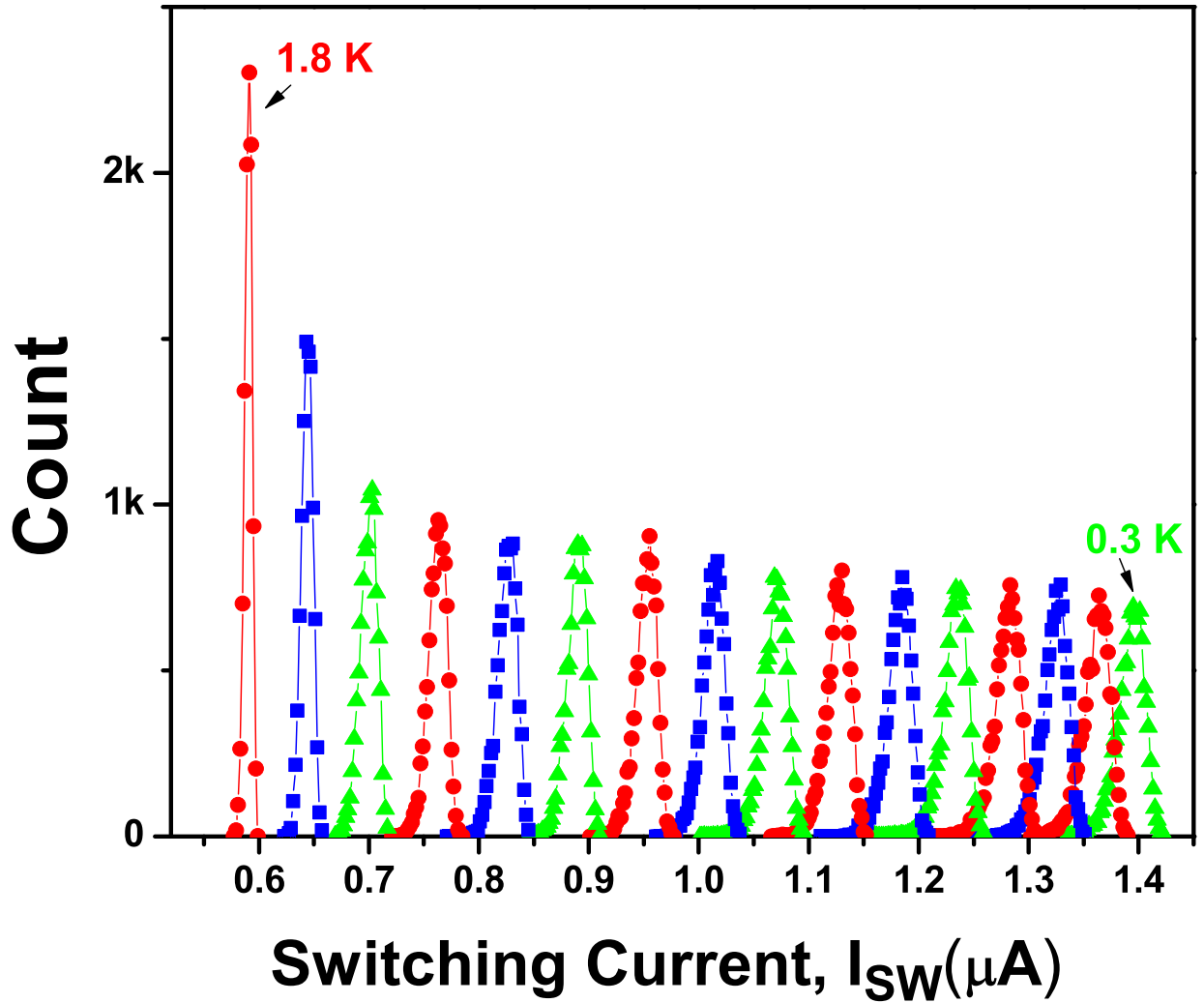


Figure 5.6: Switching current distributions  $P(I_{SW})$  for 16 temperatures between 0.3 K (right most) and 1.8 K (left most) with  $\Delta T = 0.1$  K for sample S2 ( $L = 195$  nm,  $R_N = 4100$   $\Omega$ ). For each distribution 10,000 switching events were recorded and the bin size of the histograms is 2 nA.

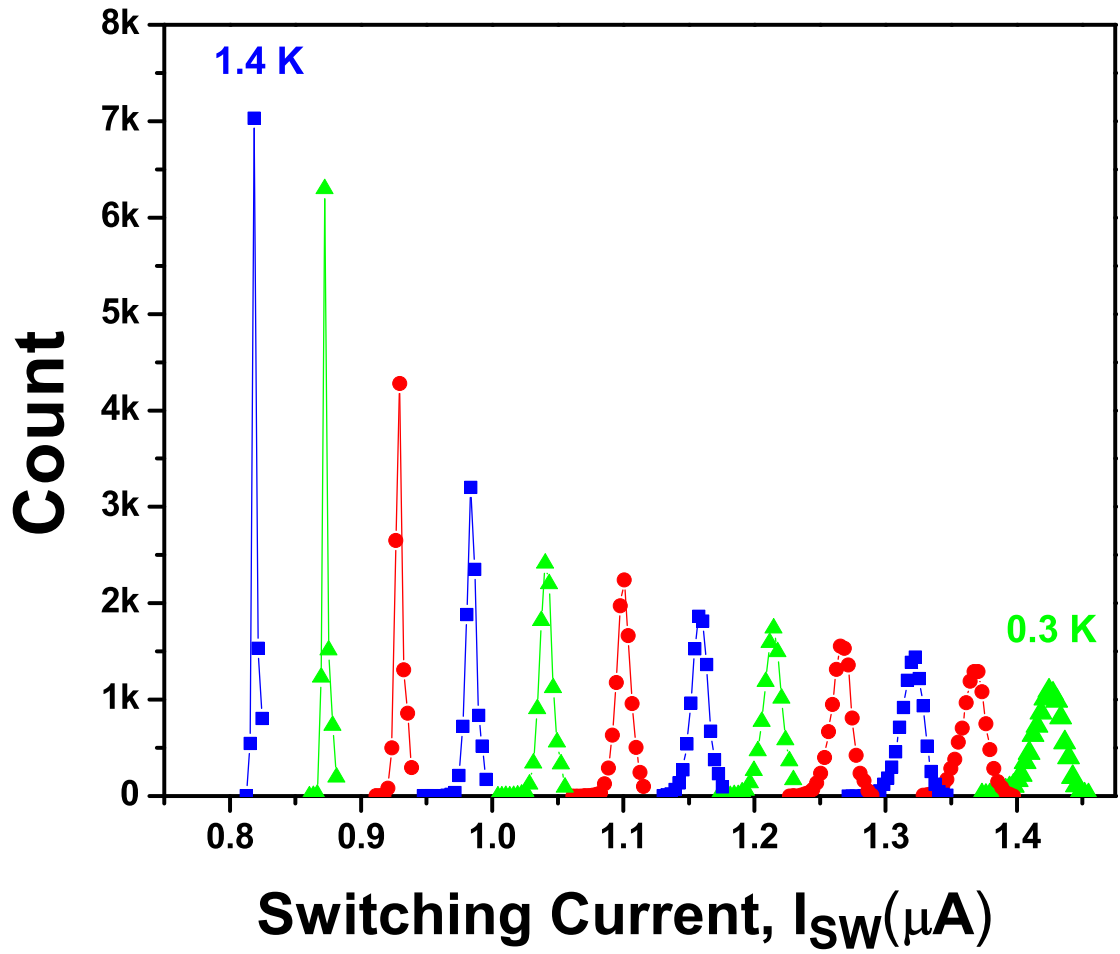


Figure 5.7: Switching current distributions  $P(I_{SW})$  for 12 temperatures between 0.3 K (right most) and 1.4 K (left most) with  $\Delta T = 0.1$  K for sample S3 ( $L = 104$  nm,  $R_N = 1430 \Omega$ ). For each distribution 10,000 switching events were recorded and the bin size of the histograms is 3 nA.

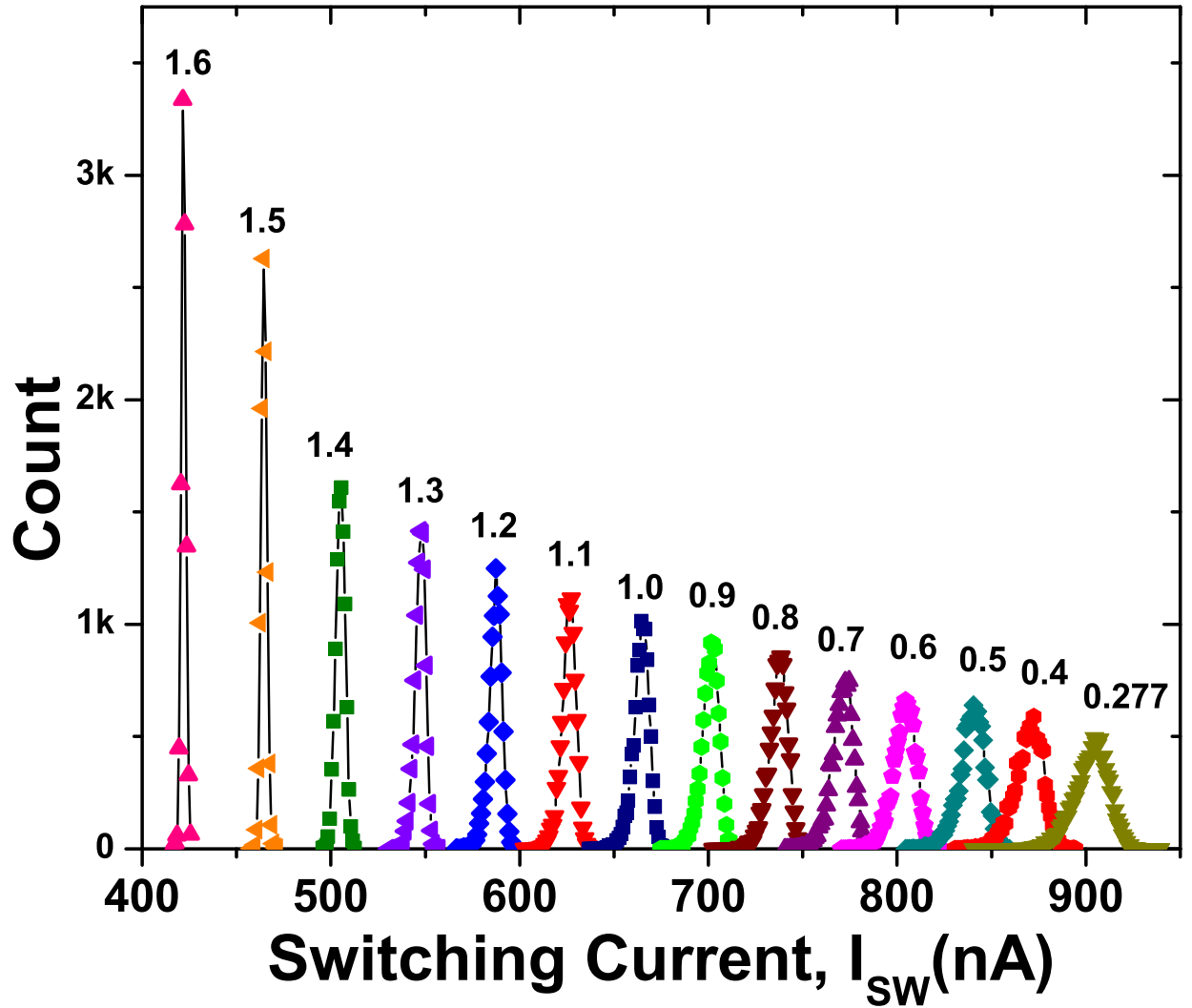


Figure 5.8: Switching current distributions  $P(I_{SW})$  for 14 temperatures between 0.277 K (right most) and between 0.4 K and 1.6 K (left most) with  $\Delta T = 0.1$  K for sample S4 ( $L = 200$  nm,  $R_N = 3900 \Omega$ ). The bath temperature for each distribution is indicated. For each distribution 10,000 switching events were recorded and the bin size of the histograms is 1 nA.

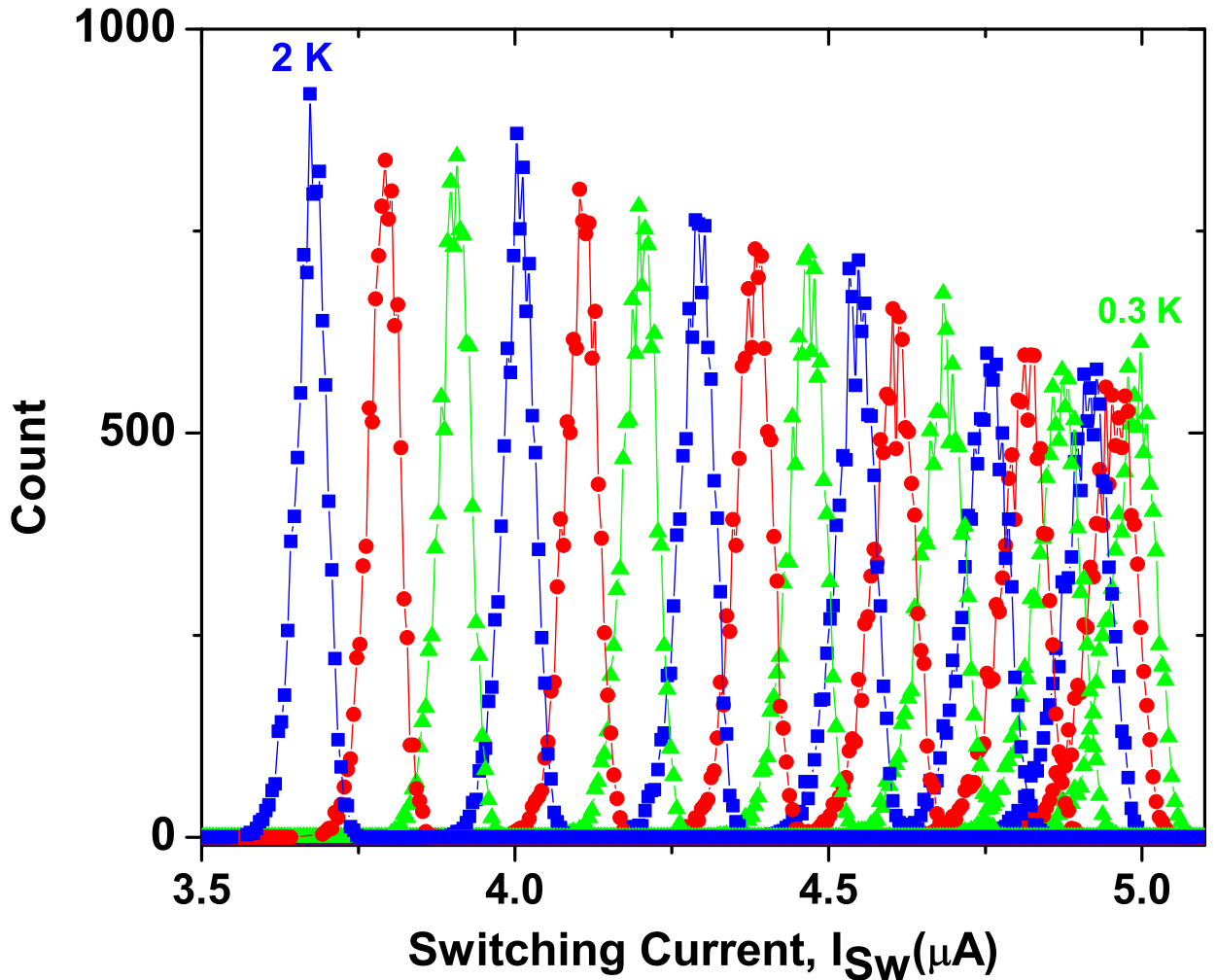


Figure 5.9: Switching current distributions  $P(I_{SW})$  for 18 temperatures between 0.3 K (right most) and 2.0 K (left most) with  $\Delta T = 0.1$  K for sample S5 ( $L = 120$  nm,  $R_N = 1450 \Omega$ ). The bath temperature for each distribution is indicated. For each distribution 10,000 switching events were recorded and the bin size of the histograms is 1 nA.

## 5.4 Standard deviation of switching current distributions

The widths of the switching current distributions can be quantified by calculating the standard deviation (SD) of the distributions. The standard deviations obtained for all the five

samples are plotted in Fig. ???. To obtain the standard deviation the formula used is,

$$\sigma = \sqrt{\frac{\sum_{i=1}^n (I_{SW,i} - \bar{I}_{SW})^2}{(n-1)}}$$

where  $\sigma$  is the standard deviation,  $I_{SW,i}$  is the  $i$ th switching current in the distribution,

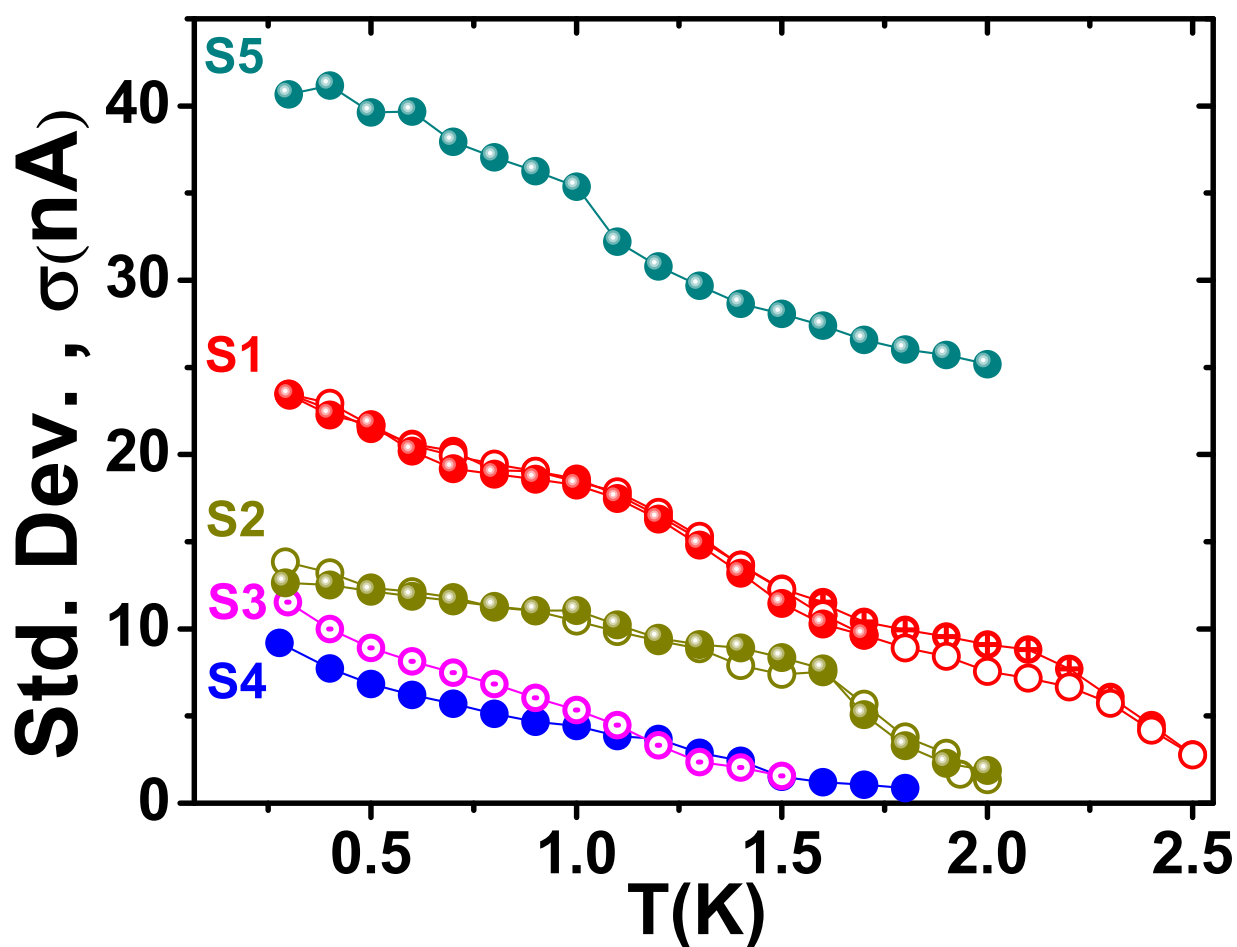


Figure 5.10: Standard deviation of switching current distributions for five samples

$\bar{I}_{SW}$  is the mean switching current,  $n$  is the total number of switching currents in the distribution. It is evident from Fig. 5.10 that for all samples the SD increases with decrease in temperature. For wires S1 and S2, the measurements were repeated a couple of times to verify the reproducibility of the data. We would like to mention that in some distribution measurements we find that there are a few anomalous switching currents recorded that are

many SDs away from the mean switching current for that distributions. For example, we have discovered for sample S5 two data points (out of a total of 10,000 points for  $T = 0.9$  K) and one data point (out of a total of 10,000 points for  $T = 1$  K) that have anomalously low values of switching current (with more than 30 standard deviations). For example, at  $T = 0.9$  K the mean value of the switching current was  $4.67 \mu\text{A}$ , the standard deviation was  $0.04 \mu\text{A}$ , and the points that we term anomalous correspond to switching currents of  $2.66 \mu\text{A}$  and  $3.35 \mu\text{A}$ . It seems to us highly likely that these three points are due to factors extrinsic to our measurement setup. Hence, these kind of anomalous points were not included in the calculation of SDs for all the samples.

## 5.5 Switching rates from switching current distributions

We can derive the switching rates from the superconducting state to the resistive state using the Fulton-Dunkleberger (FD) transformation [55]. To convert the measured switching current distribution  $P(I_{SW})$  directly into  $\Gamma_{SW}(I)$ , the relationship is,

$$P(I) = \Gamma_{SW}(I) \left( \frac{dI}{dt} \right)^{-1} \left( 1 - \int_0^I P(u) du \right) \quad (5.1)$$

where  $P(I)dI$  is the probability of switching happening in the range  $I$  and  $I + dI$ ,  $\Gamma_{SW}(I)$  is the switching rate at bias current  $I$ ,  $dI/dt$  is the sweep rate of the bias current. Also  $P(I)$  is normalized here. It is useful to consider this expression in terms of an ensemble of wires subject to increasing  $I$ . In this picture the final factor in Eq. 5.1 represents the number of wires remaining in the superconducting state after the current has reached the value  $I$ . Since  $P(I)$  is known experimentally and  $I(t)$  is known (sinusoidal or rectangular in our case),  $\Gamma_{SW}(I)$  can be obtained directly. To apply this transformation to our data, as suggested by FD, we first associate the measured distribution histogram as the number

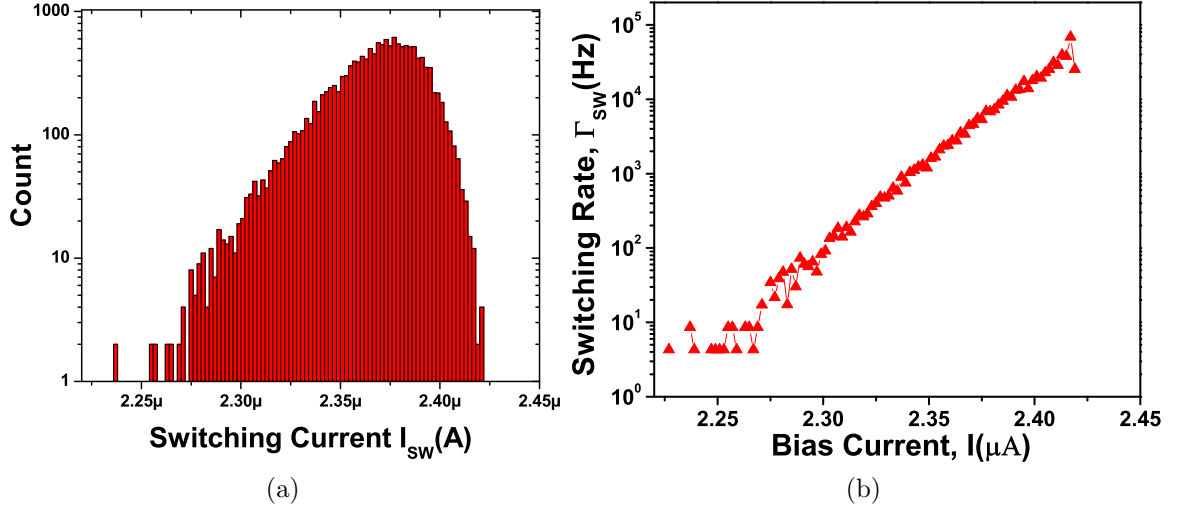


Figure 5.11: (a) Log-linear plot of the switching current distribution  $P(I_{SW})$  measured at 300 mK for wire S1 at 300 mK. For the distribution 10,000 switching events were recorded and the bin size is 2 nA. (b) log-linear plot of the switching rate vs. bias current obtained from the distribution shown in (a) using FD transformation as in Eq. 5.2. The bias-current sweep rate was  $125 \mu\text{A}/\text{sec}$ .

of counts  $P(K)$  in the channel  $K$ . To obtain the switching rate  $\Gamma_{SW}(I)$  we first associate a current  $I(K)$  to channel  $K$  using calibrated current interval per channel (denoted by  $\Delta I$  or the bin size of the histogram) and the measured channel number corresponding to  $I = 0$ . We can also determine the current sweep-rate  $dI/dt$  corresponding to the channel  $K$  since the sweep frequency and the channel numbers corresponding to the switching current  $I_{SW}$  is known. We denote by  $K = 1$  the channel corresponding to the highest value of the  $I_{SW}$  in the distribution. Then the switching rate  $\Gamma_{SW}(I)$  is calculated according to the formula,

$$\Gamma_{SW}(I) = \frac{dI}{dt} \frac{1}{\Delta I} \ln \left( \frac{\sum_{j=1}^K P(j)}{\sum_{i=1}^{K-1} P(i)} \right) \quad (5.2)$$

This is equivalent to approximating  $\int_I^\infty P(u)du$  by a series of exponential fit between adjacent points of  $\sum_{j=1}^K P(j)$ , effectively assuming thereby that  $\Gamma_{SW}(I)$  is constant over a single-channel interval. An exponential fit is used rather than a linear fit because the values of

$P(K)$  may decrease quite abruptly for low values of  $K$ . Finally,  $\Gamma_{SW}(K)$  is assigned to  $I(K)$  to yield  $\Gamma_{SW}(I)$ .

An example of distribution to rate conversion using the FD method just described is shown in Fig. 5.11. In Fig. 5.11a we have shown a log-linear plot of the switching current distribution  $P(I_{SW})$  measured at 300 mK for sample S1. To obtain  $P(I_{SW})$  at a particular temperature, we applied a triangular-wave current (sweep rate  $dI/dt = 125.5 \mu\text{A}/\text{sec}$  and amplitude  $2.75 \mu\text{A}$ ), and recorded  $I_{SW}$  for each of 10,000 cycles. The bin size of the histogram is 2 nA. To get the switching rates from distribution measurement we used Eq. 5.2 with the known  $dI/dt$  and  $\Delta I = 2 \text{ nA}$ . The obtained switching rate vs. bias current data is shown in Fig. 5.11b. We find our measurements the switching rates obtained are in the range  $1 - 10^5 \text{ Hz}$ .

The switching rate data for sample S1 obtained at 21 equally spaced temperatures between 0.3 K and 2.3 K is shown in Fig. 5.16. The distribution data used for these rates are shown in Fig. 5.5 before.

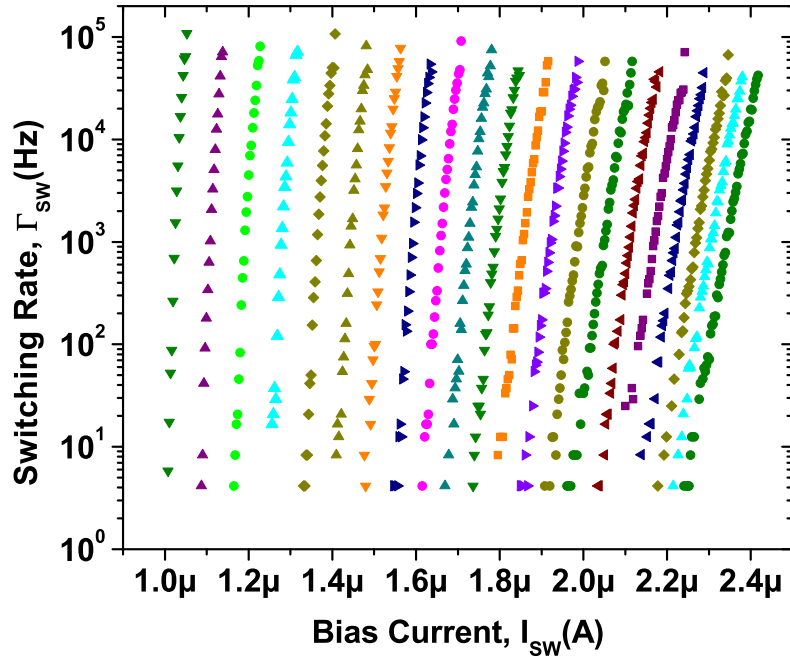


Figure 5.12: Switching rates obtained using FD transformation for wire S1 using the switching current distributions in Fig. 5.5 for 21 equally spaced temperatures between 2.3 K (left most) and 0.3 K (right most).

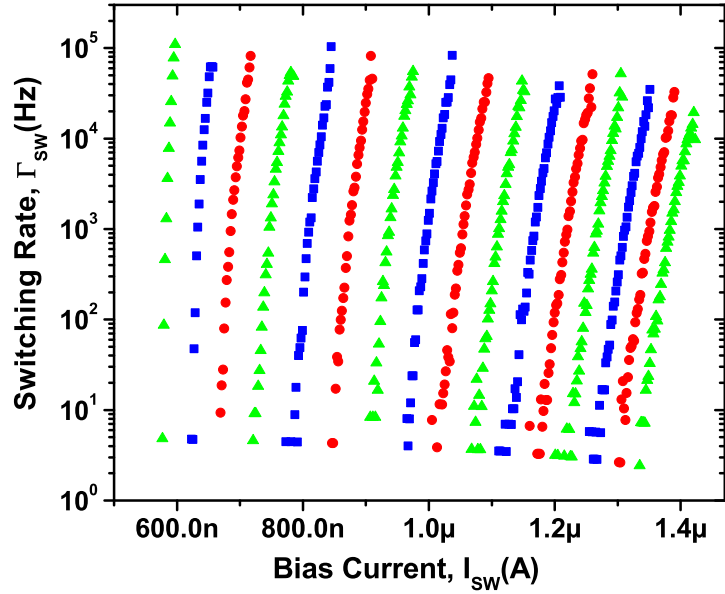


Figure 5.13: Switching rates obtained using FD transformation for wire S2 using the switching current distributions in Fig. 5.6 for 16 equally spaced temperatures between 1.8 K (left most) and 0.3 K (right most).

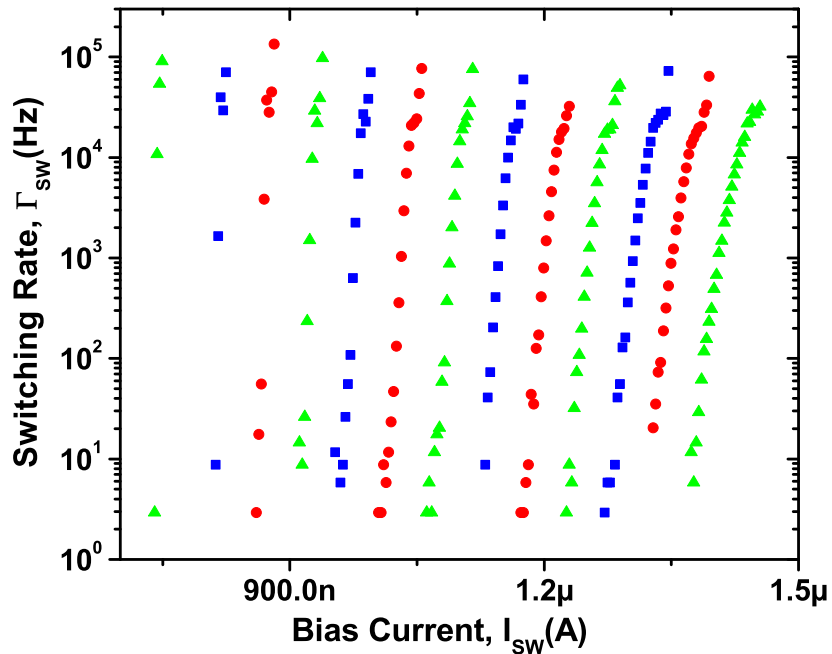


Figure 5.14: Switching rates obtained using FD transformation for wire S3 using the switching current distributions in Fig. 5.7 for 12 equally spaced temperatures between 1.4 K (left most) and 0.3 K (right most).

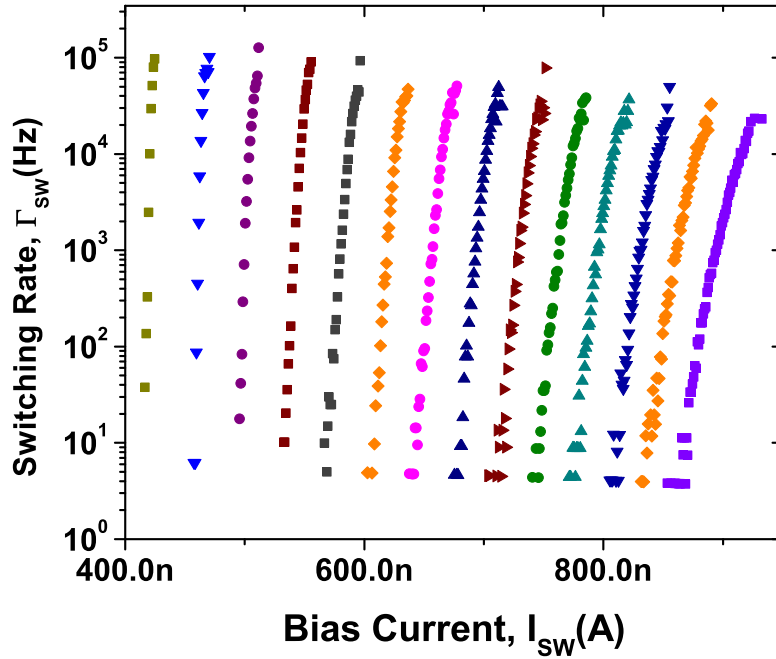


Figure 5.15: Switching rates obtained using FD transformation for wire S4 using the switching current distributions in Fig. 5.8 for 14 temperatures between 1.6 K (left most) and 0.4 K with  $\Delta T = 0.1$  K and 0.277 K (right most).

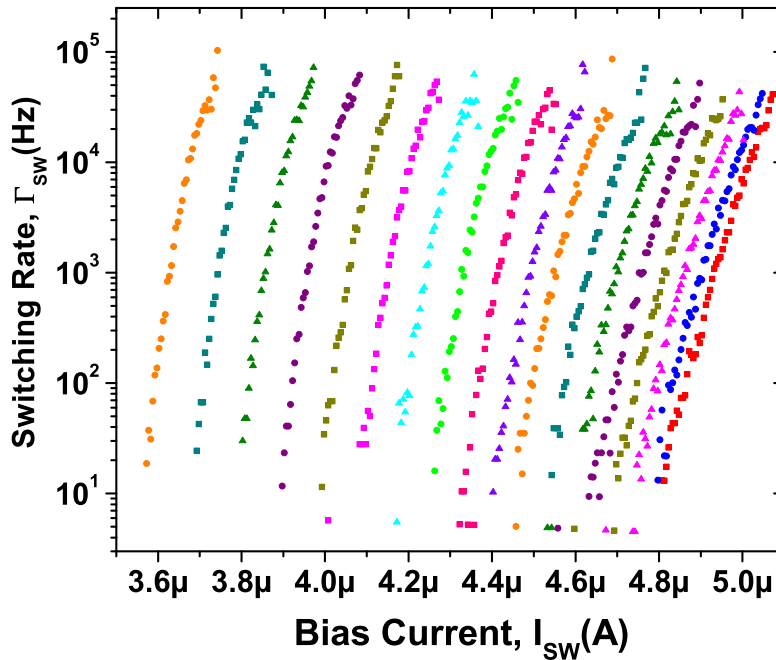


Figure 5.16: Switching rates obtained using FD transformation for wire S5 using the switching current distributions in Fig. 5.9 for 18 temperatures between 2.0 K (left most) and 0.3 K with  $\Delta T = 0.1$  K.

## 5.6 Dynamics of switching in superconducting nanowires

To understand the origin of the peculiar dependence of the switching current distribution on temperature, we review mechanisms that could be responsible for the switching from the superconducting to the resistive state, and their implications for the switching current distributions. It is evident from the observed variability of the switching current that, to be viable, a candidate for the switching mechanism must be stochastic in nature. This suggests that the switching events are triggered by intrinsic fluctuations in the wire. In what follows, we shall focus on mechanisms driven by phase-slip fluctuations.

The simplest mechanism to consider is the one in which a single phase slip necessarily causes switching to the resistive state, as in an under-damped Josephson junctions [55]. In fact in our wires, at temperatures  $T > \sim 1$  K, the rate of TAPS as indicated by both low-bias  $R - T$  and high-bias  $V - I$  measurements, is always expected to be much larger than the observed switching rate, even at very low currents. Therefore, at these temperatures, a current-carrying wire undergoes many TAPSs before the switch takes place, as directly confirmed by the non-zero voltage regime observed prior to the switching [19, 21]; as shown in Fig. 5.2. For  $T > 2.7$  K we can measure these residual voltage tails occurring at current lower than the switching current. As the temperature is reduced, these voltage tails, indicating a non-zero phase slips rate, become smaller, and below  $\sim 2.5$  K the voltage falls below the experimental resolution of our setup ( $\sim 2 \mu\text{V}$ ). The quantitative analysis of the switching process [23] leads us to the conclusion that the switching is activated by multiple phase slips at  $T > \sim 1$  K and by single phase slips at  $T < \sim 1$  K.

We now focus on switching mechanisms that incorporate multiple phase-slips. The observed high-voltage state is inconsistent with the presence of a phase-slip centre, because there is almost no offset current. We therefore hypothesize that the dynamics is always over-damped, and propose a runaway overheating model in spirit of ref. [24]. Our model

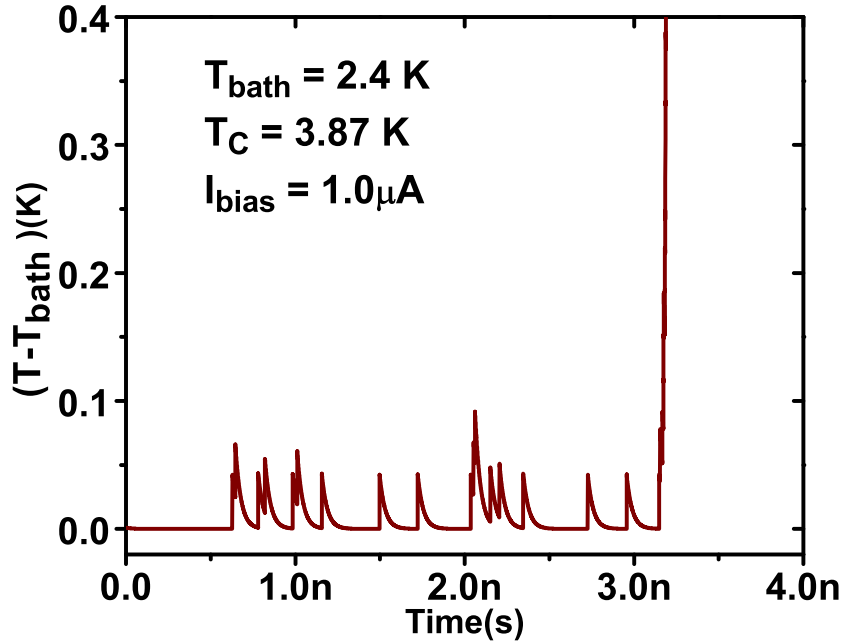


Figure 5.17: Simulated “temperature bumps” in the nanowire due to a sequence of phase-slips events. The bath temperature is assumed to be  $T_b = 2.4$  K,  $T_C = 3.87$  K and bias current  $I = 1.0 \mu\text{A}$ . As the temperature of the wire section becomes higher than  $T_C$ , it becomes normal.

has two ingredients: (i) Stochastic phase slips that heat the wire by a quantum of energy, and occur at random times and locations in the wire, but with a rate that depends on the local temperature of the wire. (ii) The heat produced by the phase slips is conducted along the wire, and is carried away by the leads. In effect, right after a phase-slip has occurred, the temperature of the wire rises, and therefore the phase-slip rate is enhanced. The higher phase-slip rate persists until the wire cools down. If another phase-slip happens to occur before the wire has cooled down, the temperature would rise further. Moreover, if, after several consecutive phase-slips, the temperature in the wire becomes high enough for the phase-slip rate to exceed the cooling rate, a subsequent cascade of phase slips carries the wire into the high-voltage state, which is the normal state. Thus the switching is stochastic in nature. The rate of this switching is directly determined by the likelihood of having an initial burst of phase-slips that starts a cascade. This phenomenology is captured in Fig. 5.17, which shows the temperature at the center of a wire (above the bath temperature) as

a function of time. Phase-slips correspond to sudden jumps in temperature, while cooling corresponds to the gradual decrease of temperature. A burst of phase-slips that results in a cascade can be seen near time  $t = 3$  ns.

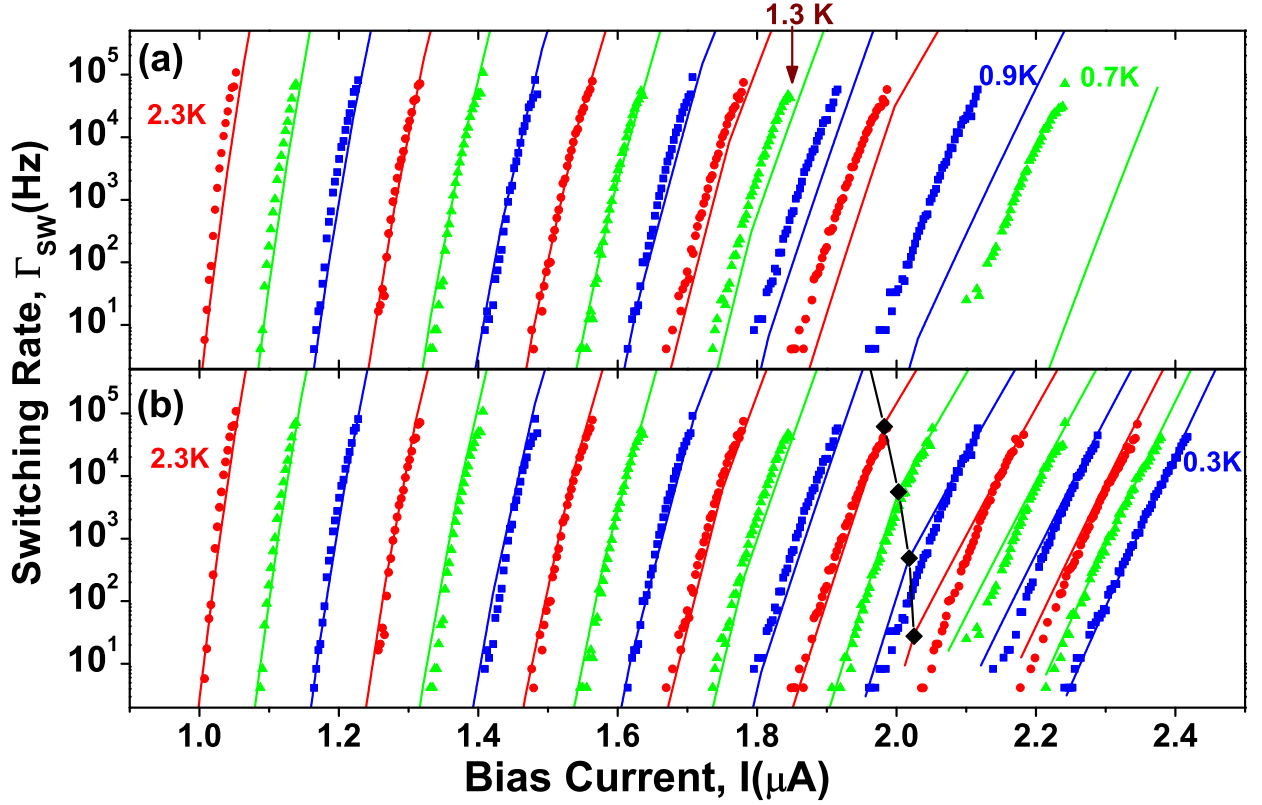


Figure 5.18: (a) Switching rates from the superconducting state to the resistive state for both temperatures between 2.3 K (left most) and 0.7 K (right most) (here not all the measured curves are shown for clarity). The data is shown for all temperatures between 2.3 K and 1.1 K with  $\Delta T = 0.1$  K and for  $T = 0.9$  K and  $T = 0.7$  K (sample S1). The symbols are experimental data and the lines (with corresponding color) are fits to the overheating model that incorporates stochastic TAPS-only (see text). The fits agree well with the data down to 1.3 K, indicated by an arrow. (b) Fits to the same data (all temperatures are shown here) with the stochastic overheating model which now incorporates both the TAPS and QPS rates to calculate the switching rates. The boundary for single phase-slip switch regime is indicated by the black diamond symbols at four temperatures (connected by line segments). For the measured range of switching rates, any of the  $(I, \Gamma_{SW})$  to the right of this boundary (i.e., for higher bias currents) is in the single-slip regime.

In the overheating model just discussed, the width of the switching-current distribution is controlled by the competition between the number of phase slips in the cascade-triggering burst and the rate of phase slips. If the number of phase slips to make such a burst tends

to unity, the switching rate approaches the phase-slip rate. In the opposite regime, in which a large number of phase-slips are required to form the burst, the switching rate is much lower than the phase-slip rate. At higher temperatures, many phase slips are needed in the initial burst, and thus switching tends to occur only when  $I_{SW}$  is in a very narrow range close to  $I_C$ , thus making the distribution narrow. As the temperature decreases, the heat capacity and heat conductivity both decrease, making phase-slips more effective at heating the wire. Thus, the typical number of phase slips in the cascade-triggering burst decreases with temperature, as our model shows [23]. At the same time, the rate of TAPS also decreases with temperature. In practice, with decreasing temperature, the broadening effect of the burst length on  $P_{SW}(I)$  overwhelms the narrowing effect of the decreasing TAPS rate, and this provides a possible explanation of the unanticipated broadening of the  $I_{SW}$  distributions.

We first tried to fit all the switching-rate data in Fig. 5.18 using the overheating model but with a phase-slip rate  $\Gamma$  that follows from allowing only thermally-activated (and not quantum) processes, i.e.,  $\Gamma_{TAPS}$ . At temperature  $T$  and bias-current  $I$ ,  $\Gamma_{TAPS}$  is given by,

$$\Gamma_{TAPS} = \frac{\Omega_{TAPS}(T)}{2\pi} \exp\left(-\frac{\Delta F(T, I)}{k_B T}\right) \quad (5.3)$$

where  $\Omega_{TAPS}(T)$  is the attempt frequency,  $\Delta F(T, I) = \Delta F(T) \left(1 - \left(\frac{I}{I_C(T)}\right)\right)^{5/4}$  is the free-energy barrier at bias-current  $I$  [25, 24],  $I_C(T)$  is the fluctuation-free depairing current, and  $\Delta F(T) = \sqrt{6} \frac{\hbar I_C(T)}{2e}$  is the free-energy barrier at zero bias-current. These fits agree well with the data over the temperature range 2.4 K to 1.3 K (Fig. 5.18b). Within this range, we can attribute the decrease in the width of the distribution to the mechanism described in the previous paragraph: the competition between (i) the number of phase slips in the initial burst required to start a cascade, and (ii) the rate of phase slips. However, below 1.2 K it is evident from Fig. 3a that the switching rates predicted by TAPS are considerably smaller than the switching rates obtained experimentally.

## 5.7 Quantum phase slip and single phase-slip regime

As the temperature is reduced and fluctuations become smaller, the switching happens at higher values of the bias-current  $I$ . Thus each phase slip releases more heat into the wire ( $Ih/2e$ ). Also, as bias-current  $I$  is increased, the value of the temperature increase required in order to reach the normal state becomes smaller. Therefore, according to the overheating model one ultimately expects to have a low  $T$  regime in which a single phase-slip event releases enough heat to induce a switching event [23]. We call this the single-slip regime. We expect that for  $T < \sim 0.7$  K, the wire S1 should be operating in this single-slip regime, as indicated in Fig. 5.18b (the black curve). We find, however, in the regime  $0.3 \text{ K} < T < 1.2 \text{ K}$  our data can not be fitted well if the phase-slip rate is taken to be  $\Gamma_{TAPS}$ , but can be fitted well if the total phase-slip rate ( $\Gamma_{TOTAL}$ ) is taken to be the sum of TAPS rate ( $\Gamma_{TAPS}$ ) and QPS rate ( $\Gamma_{QPS}$ ), i.e.,

$$\Gamma_{TOTAL} = \Gamma_{TAPS} + \Gamma_{QPS} \quad (5.4)$$

Since at 0.3 K we are already in the single-slip regime the switching rate should be equal to the phase-slip rate. We now introduce a simple model of QPS that was suggested by Giordano [35, 10]. We use this model, but instead of the Ginzburg-Landau relaxation time, which is only correct near  $T_C$ , we use the notion of the effective “quantum” temperature  $T_{QPS}$ , which is a common (and well-tested) approach in Josephson junctions (JJ) [5]. Thus, the QPS rate is given by the same expression as the TAPS rate but with the wire temperature  $T$  replaced by an effective “quantum” temperature  $T_{QPS}(T)$ , i.e.,

$$\begin{aligned} \Gamma_{QPS} &= \frac{\Omega_{QPS}(T)}{2\pi} \exp\left(-\frac{\Delta F(T, I)}{k_B T_{QPS}}\right) \\ &= \left(\frac{L}{\xi(T)}\right) \left(\frac{1}{\tau_{GL}}\right) \left(\frac{\Delta F(T)}{k_B T_{QPS}}\right)^{1/2} \exp\left(-\frac{\Delta F(T, I)}{k_B T_{QPS}}\right) \end{aligned} \quad (5.5)$$

As shown in Fig. 5.19, at 0.3 K, the measured switching rate can be fitted by the Giordano-type QPS rate. For  $T = 0.3$  K, the switching rate predicted by TAPS is roughly

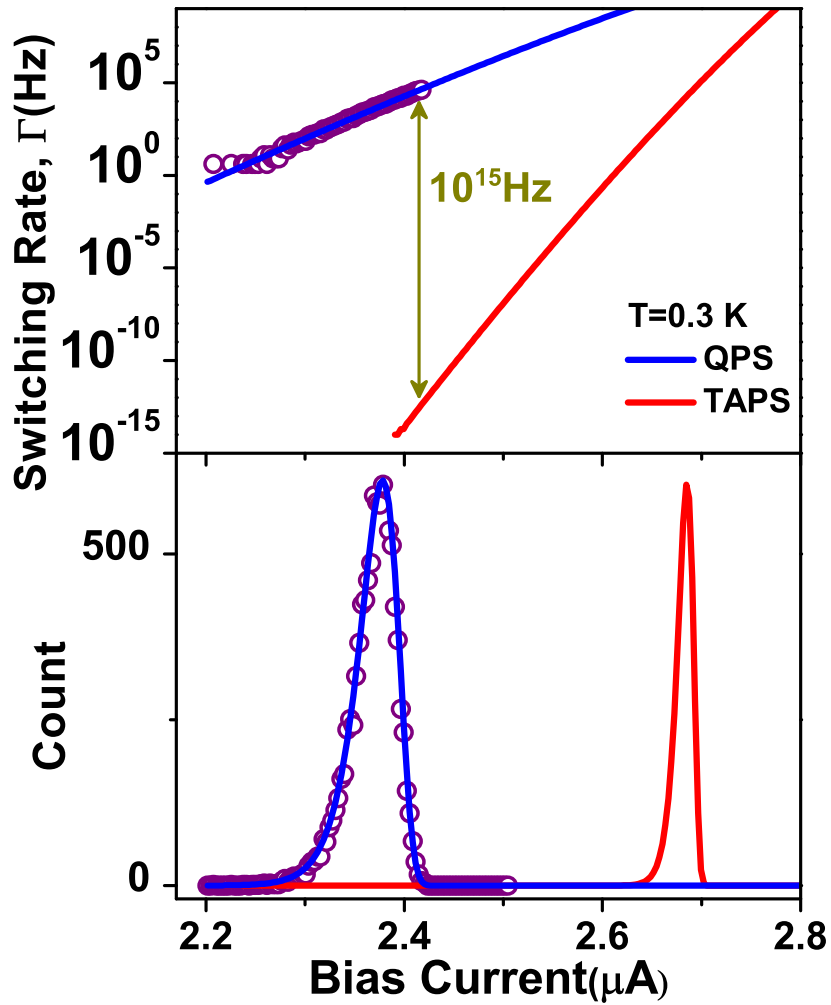


Figure 5.19: (top panel) Switching rates at  $T = 0.3 \text{ K}$  for sample S1 (open circles). The blue curve is the fit to the data, based on the Giordano-type QPS model. The red curve is expected for the TAPS rate. The arrow indicates the difference between the expected TAPS rate and the data. This difference is very large namely  $10^{15} \text{ Hz}$ . (bottom panel) The corresponding switching current distribution at  $0.3 \text{ K}$  (open circles) and the predictions due to QPS rate (blue) and TAPS rate (red).

$10^{15}$  times smaller than the measured switching rate as indicated in Fig. 5.19 . In the model of QPS used,  $T_{QPS}$  is the effective quantum temperature representing the strength of zero-point fluctuations in the  $LC$ -circuit formed by the nanowire, which has a nonzero kinetic inductance of the order of 0.1 nH, and the leads, with a mutual capacitance of the order of 1-10 fF. Thus we can roughly estimate the plasma frequency as  $\omega_p \approx \sqrt{1/LC}$  and therefore the expected quantum temperature is  $\sim 1$  K. Using different expressions for the attempt frequency (e.g. those derived for Josephson junctions) can only increase the disagreement between the TAPS model and the data (to be discussed later). On the other hand, fitting the measured switching rate with the Giordano-type QPS rate for several values of the temperature; we find a very good agreement. The corresponding effective quantum temperature  $T_{QPS}(T)$  is considerably higher than the bath temperature  $T$ , which is a strong indication of QPS. We also observe that to fit data it is necessary to assume a weak linear dependence of the  $T_{QPS}(T)$  on the bath temperature  $T$  (Fig. 5.20). For sample S1,  $T_{QPS}$  is found to be,  $T_{QPS}(T) = 0.726 + 0.40 \times T$  (in Kelvins). The non-zero intercept indicates the persistence of the high-bias-current-induced QPS down to zero temperature. It is found that below a crossover temperature  $T^*$  the QPS rate dominates over the TAPS rate and the fluctuations in nanowire are mostly quantum in nature. This  $T^*$  for wire S1 is 1.2 K and is denoted by the red arrow in Fig. 5.18 . To verify the consistency of our model at all measured temperatures, we replaced the TAPS rate by the total phase-slip rate  $\Gamma_{TOTAL}$  (Eq. 5.4) to obtain the switching rates over the full range of temperatures (i.e., 0.3 K-2.3 K). We find that the predicted switching rates agree reasonably well with the data as shown in Fig.5.18b for all temperatures.

Furthermore, we verified the evidence of QPS in four more nanowire samples (S2-S5). The function  $T_{QPS}(T)$  (which we define to be linear in all cases) for these nanowires is shown in Fig.5.20. As with the first sample, this linear dependence is chosen to give the best possible fits to the measured switching rates, as those in Fig. 5.19. Also, the corresponding crossover temperatures  $T^*$  for all samples are indicated by the arrows. We find that the  $T^*$  is consistently reduced with the reduction of the critical depairing current  $I_C(0)$ : as shown

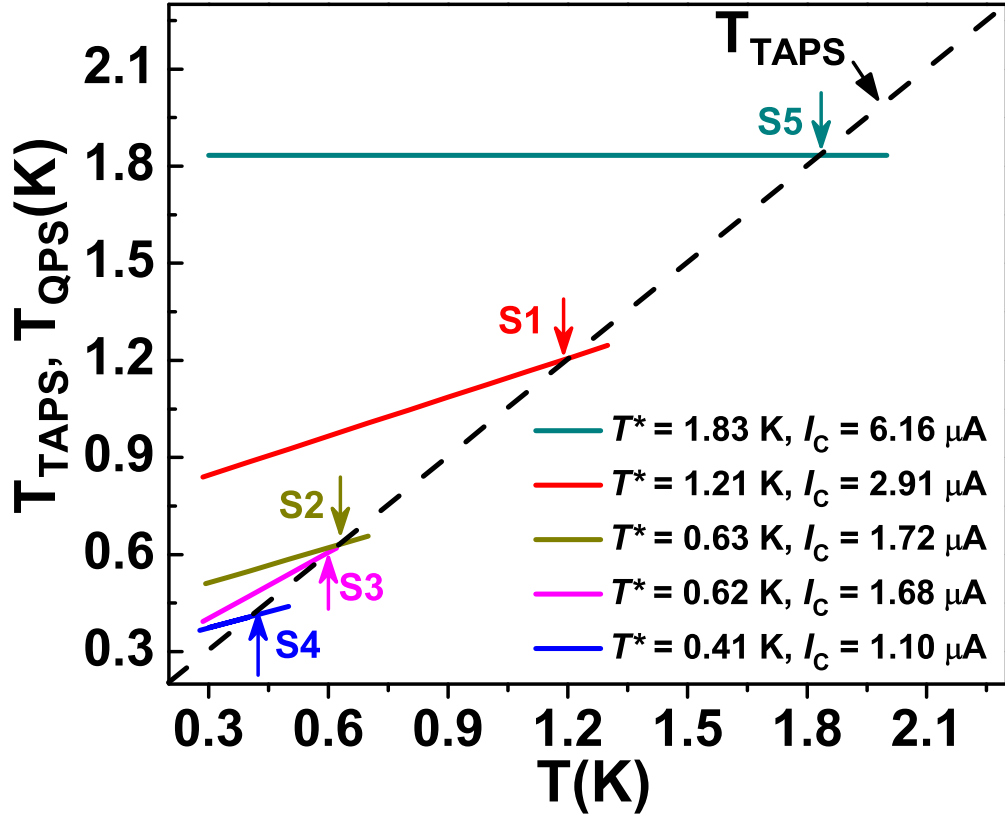


Figure 5.20: The best fit effective temperature for fluctuations at different bath temperatures for five different samples (S1-S5). For all TAPS rates calculation the effective temperature is chosen as the bath temperature (shown by the black dotted line). For the QPS rates, the effective temperature  $T_{QPS}$ , used in the corresponding QPS fits, similar to the blue-line fits of Fig.5.19, are shown by the solid lines. For each sample, below the crossover temperature  $T^*$  (indicated by arrows), QPS dominates the TAPS. We find that the  $T^*$  decreases with decreasing critical depairing current of the nanowires, which is the strongest proof of QPS. The trend indicates that the observed behavior of  $T_{QPS}$  below  $T^*$  is not due to extraneous noise in the setup or granularity of wires, but, indeed, is due to QPS.

in Fig. 5.20. This observed trend is analogous to the case of Josephson junctions in ref. [5]. To understand this observation we remind that  $T^*$  is proportional to the plasma frequency of the device, which, in turn, is proportional to the critical current. On the other hand, if the observed increase in the fluctuation strength and the fact that  $T_{QPS} > T$  were due to some uncontrolled external noise in the setup, the thicker wires, having larger critical currents, would have shown a reduction in the  $T^*$ , which is opposite to what we observe. These observations also allow us to rule out the possibility that some hidden granularity cause the QPS-like effects. Indeed, what we find is that wires of lower critical currents, which obviously have more chance to have weak links, show a less pronounced quantum behaviour and a lower  $T^*$  value (Fig. 5.20). Thus the possibility of weak links producing the reported here QPS-like effects is ruled out. In conclusion, the result of Fig. 5.20 provides a qualitatively new and strong evidence for the existence of QPS in thin superconducting wires.

We would like to briefly comment on the attempt frequency  $\Omega$ , that is used to get the TAPS rate. In Fig. 5.21, we have plotted the TAPS rates estimated using different expressions for  $\Omega$  (curves 2 - 4), the data (open circles) and the QPS rate (curve 1) (all at 0.3 K). For curve 2 we have used,  $\Omega = (L/\xi(T)) (\Delta F(T)/k_B T)^{1/2} (1/\tau_{GL})$  according to McCumber and Halperin expression, based on time-dependent Ginzburg-Landau equations. In this expression,  $[L/\xi(T)]$  is of the order of  $\sim 10$ ,  $(\Delta F/k_B T)^{1/2}$  is of the order of  $\sim 10$  and  $(1/\tau_{GL})$  is of the order of  $\sim 10^{12}$ . Hence  $(1/\tau_{GL})$  is the dominant term in the expression for  $\Omega$ . We also attempt to obtain the estimates of the thermal phase slip rate without relying on time-dependent Ginzburg-Landau equations, and arrive practically at the same conclusions, as is explained in detail below.

For curve 4, we have replaced  $(1/\tau_{GL})$  by the characteristic frequency of the nanowire, which acts as an inductor and forms an  $LC$ -circuit with the leads, which are coupled to each other by a capacitance. In other words, we replace  $(1/\tau_{GL})$  with  $\omega_{LC}$ , where  $L_w \simeq \hbar L/3\sqrt{3}eI_C(T)\xi(T)$  is the kinetic inductance of the wire [56], and  $C$  is the capacitance

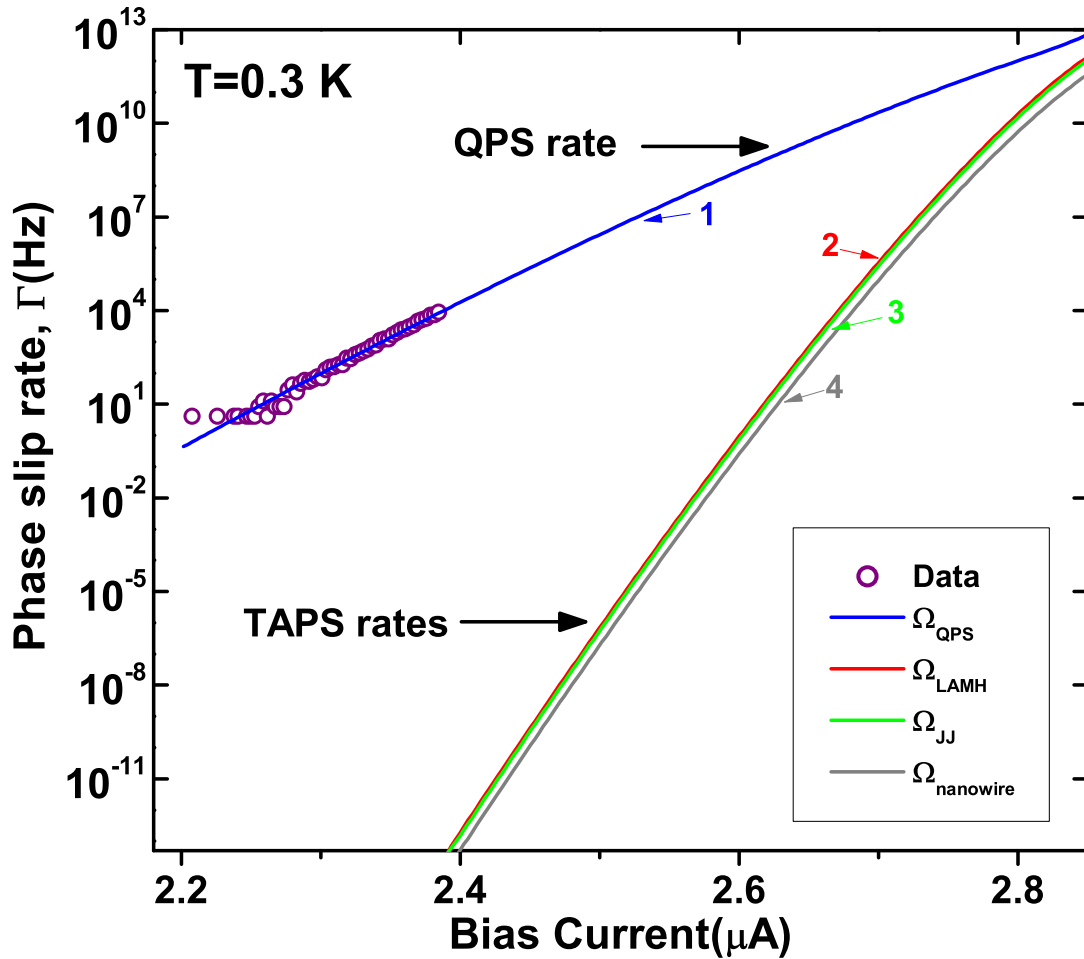


Figure 5.21: The data (open circles) and the calculated QPS rate (solid blue line) at 0.3 K for wire S1. The observed agreement is very good. Different estimates of TAPS rate by using different attempt frequency expressions are also shown by solid red, green, and grey lines. For all our estimates of TAPS rate, the data is at least  $\sim 10^{15}$  orders of magnitude higher than the predicted thermal rate. Hence, the data can not be explained by considering thermal fluctuation alone, even if the uncertainty in the attempt frequency is taken into account. Note also that for the lowest bias current of 2.2  $\mu\text{A}$ , the thermal rate is about  $10^{25}$  orders lower than the experimental rate, which further proves our point.

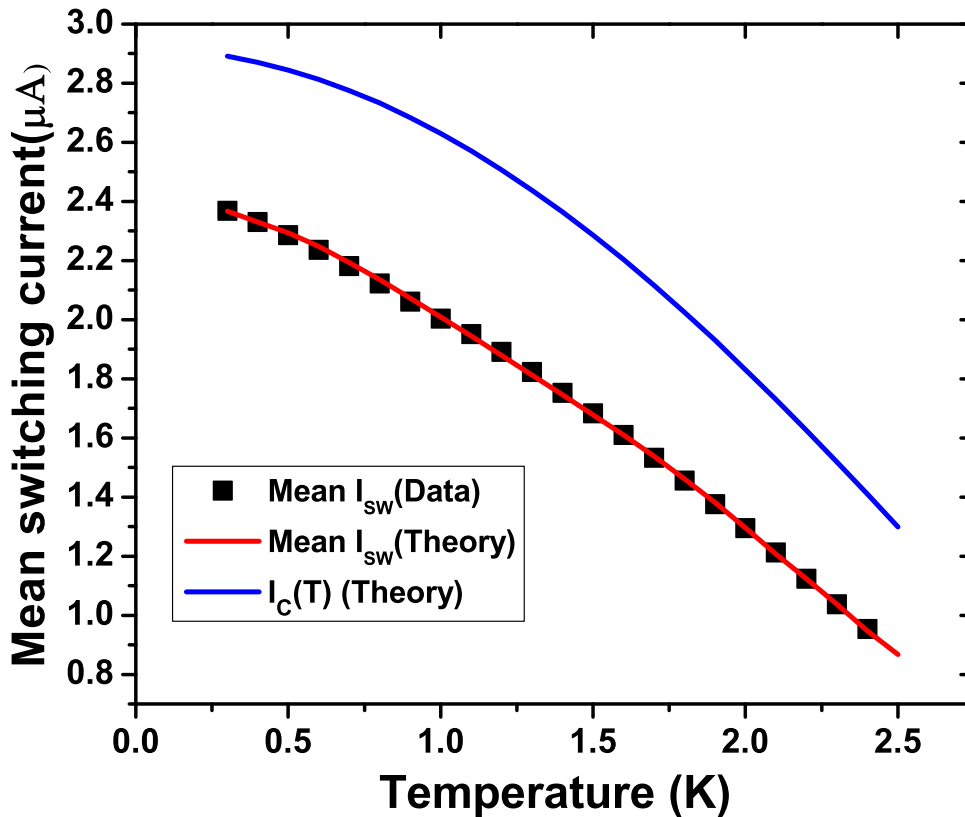


Figure 5.22: The measured mean switching current (squares) and the predicted mean switching current by our model (red line) as a function of temperature. The predicted fluctuation-free critical depairing current,  $I_C(T)$  is shown (blue line). At all temperatures a premature switching occurs before the bias current reaches the critical depairing current.

of the leads. For the calculations  $C$  is taken to be 10 fF [20]. Thus obtained curve (gray line in Fig. 5.21) is very close to the traditional LAMH result (the red curve). In another attempt to verify the approximate validity of the McCumber-Halperin attempt frequency, we replaced  $(1/\tau_{GL})$  by a well-known expression of plasma frequency for a JJ [30], i.e.,  $\omega_p = \sqrt{2eI_C(T)/\hbar C}$ . Again, the obtained curve 3 (green) appears very close to the LAMH result. Thus, in all cases, we find that with the TAPS model, the prediction of the phase slip rate is  $\sim 10^{15}$  orders of magnitude smaller than the data and we can in no way account for this difference by changing the attempt frequency. Hence, it strongly indicates that, at low temperatures, the measured phase slips are QPS, not TAPS.

The mean switching current predicted at each temperature by the overheating model and

the mean switching current for each distribution (Mean  $I_{SW}$ ) is compared in Fig. 5.22. We have also plotted the critical depairing current  $I_C(T) = I_C(0) [1 - (T/T_C)^2]^{3/2}$  [57]. We find that at all temperatures the switching is premature.

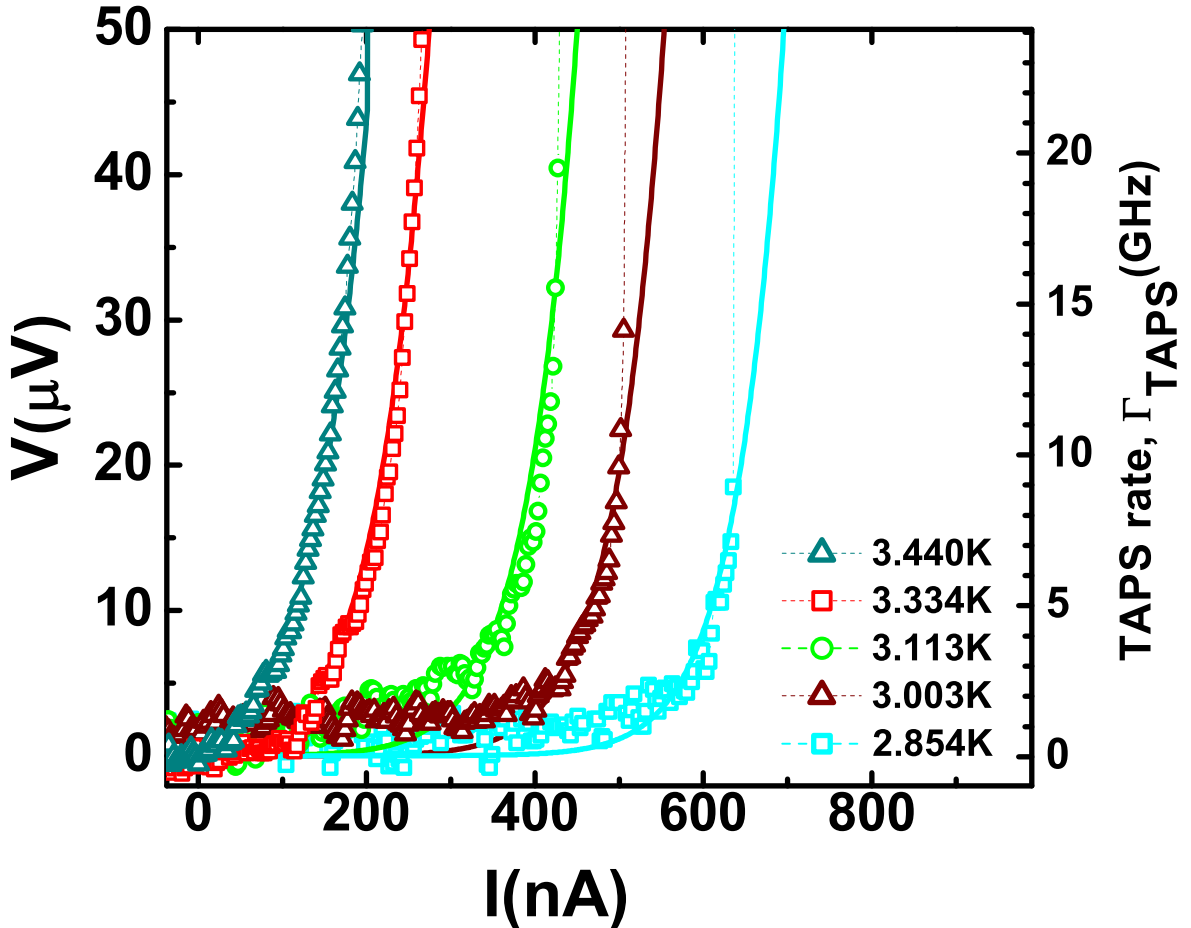


Figure 5.23: High-bias V-I measurements at high temperatures where the voltage due to phase diffusion is measurable even before the switching event. The solid lines are predictions of phase slip rate using the TAPS model with the wire parameters used are those which were obtained by fitting the switching rates measurements between  $T = 0.3$  K to 2.3 K. The phase-slip rate  $\Gamma_{TAPS}$  (shown in the right axis) is converted into voltage using the relation,  $V = \frac{h\Gamma_{TAPS}}{2e}$ . The dashed line is the line connecting the data points, not a fit.

Another independent validation of the TAPS model, applied at higher temperatures, and the wire parameters used, can be obtained from non-linear  $I - V$  curves measured at relatively high temperatures. At these temperatures measured  $I - V$  curves show tails due to TAPS that are large enough to be measured in our set up; as shown in Fig. 5.23. In Fig.

5.23, we also plotted the predicted voltage obtained from the TAPS model, using  $V = \frac{\hbar\Gamma_{\text{TAPS}}}{2e}$ . For the TAPS rate calculations, the wire parameters used for all our fittings (as shown in Fig. 3) are kept the same and only the  $T$  was varied to get the corresponding TAPS rate. The measured voltage (or phase-slip rate) and the predicted voltage (or the TAPS rate) are in good agreement for the five temperatures noted in Fig. 5.23. This agreement indeed verifies our model for TAPS. The calculation of the TAPS V-I curve is made under the assumption that the wire temperature equals the bath temperature, i.e., no significant Joule heating occurs. These type of phase diffusion “tails” on the V-I curves can only be seen at temperature of about 2.7 K or larger, which is about 10 times higher a temperature than those where the QPS effects are found.

We can also estimate the zero-bias resistance from our high-bias switching current measurements for very low temperatures, by an extrapolation. Using LAMH theory, we can convert the zero-bias phase slip rate,  $\Omega(T) \exp\left(-\frac{\Delta F(T)}{k_B T}\right)$  to resistance. We find that the resistance drops exponentially from  $10^{-50}$  to  $10^{-80}$   $\Omega$  for temperatures from 1.1 K to 0.3 K in the QPS dominated regime for sample S1. This resistance is obviously very small to be measured in a typical lab setup and can only be estimated from such an extrapolation of the switching current measurements data. We verified that this resistance is of the same order as predicted by Golubev-Zaikin (GZ) theory ??, which gives for zero-temperature limit the result as follows,  $R_{QPS} = \Omega(T) \exp(-AR_Q L/R_N \xi(0))$ . To get the resistance value of  $10^{-50}$  to  $10^{-80}$   $\Omega$  we varied  $A$  from 2.7 to 4.0 for  $T = 1.1$  K to  $T = 0.3$  K. This is in agreement with the GZ theory, since they predict that  $A$  should be of the order of unity, which we confirm.

## Nanowire parameters

Nanowire	$L$ nm	$R_N$ $\Omega$	$T_C$ K	$\xi(0)$ nm	$I_C(0)$ nA	$A$ nm <sup>2</sup>	$T_{QPS}(T)$ in the form $T_0 + T_1 \times T$	$T^*$ K
S1	110	2666	3.872	5.038	2917	74.2	$0.726 + 0.40 \times T$	1.210
S2	195	4100	3.810	9.650	1727	85.6	$0.404 + 0.0.362 \times T$	0.633
S3	104	1430	3.160	12.560	1683	130.9	$0.199 + 0.0.678 \times T$	0.620
S4	200	3900	2.870	12.250	2917	92.3	$0.275 + 0.0.33 \times T$	0.410
S5	120	1450	4.55	5.637	6164	148.9	1.834	1.834

Table 5.1: Nanowire sample parameters for the five measured MoGe wires. The parameters listed are: length ( $L$ ), normal state resistance ( $R_N$ ), critical temperature ( $T_C$ ), zero-temperature coherence length ( $\xi(0)$ ), critical depairing current ( $I_C(0)$ ), cross sectional area ( $A$ ), effective quantum temperature  $T_{QPS}(T)$  and crossover temperature  $T^*$ .

## 5.8 Details of the stochastic overheating model

In this section I will discuss the model of overheating in superconducting nanowires due to stochastic phase slips that was developed in collaboration with D. Pekker, N. Shah, T-C Wei and P. Goldbart to explain the switching rates obtained from measurements of our nanowires.

### 5.8.1 Model for heating by phase slips

The goal of this section is to construct a theoretical model of the stochastic dynamics that leads to the switching of current-biased nanowires from the superconductive to the resistive state. We begin by reviewing the theory of the steady-state thermal hysteresis as set out in Ref. [24]. We continue by replacing the *steady-state* heating of the wire by heating via *discrete* stochastic phase-slips. The main result of this section is a Langevin-type stochastic differential equation that describes the dynamics of the temperature within the wire.

## I. Thermal hysteresis mechanism

The thermal mechanism for hysteresis in superconducting nanowires was originally proposed by Tinkham et al.[24]. Here we set up the quantitative description of the mechanism by giving a brief account of their work, and thus set the stage for our stochastic extension of it. Their description rests on the premise that the temperature of the wire is controlled by a competition between Joule heating and cooling via the conduction of heat to the leads. If  $\Theta(x)$  is the temperature at position  $x$  along the wire of length  $L$  and cross-sectional area  $A$ , then the power-per unit length dissipated due to Joule heating at a bias current density  $I$  is taken to be

$$Q_{\text{source}}(x) = \frac{I^2 R(\Theta(x))}{AL}, \quad (5.6)$$

where the function  $R(\Theta')$  is to be understood to be the resistance of an entire wire held at a uniform temperature  $\Theta(x) = \Theta'$ . On the other hand, since the wire is suspended in vacuum, the heat is almost exclusively dissipated through its conduction from the wire to the superconducting leads that are held at a temperature  $T_b$  and which play the role of thermal baths. The heating and cooling of the wire is described by the corresponding static heat conduction equation:

$$Q_{\text{source}}(x) = -\partial_x [K_s(\Theta) \partial_x \Theta(x)] \quad (5.7)$$

$$= -\frac{\partial K_s(\Theta)}{\partial \Theta} (\partial_x \Theta)^2 - K_s(\Theta) \partial_x^2 \Theta, \quad (5.8)$$

where  $K_s(\Theta)$  is the thermal conductivity of the wire (The first term on the right-hand side of Eq. (5.8) was absent in Ref. [24]). This equation is supplemented by the boundary conditions  $\Theta(\pm L/2) = T_b$  at the wire ends,  $x = \pm L/2$ , and is numerically solved via the corresponding discretized difference equation.

It was found in Ref. [24] that Eq. (5.8) yields two solutions for a certain range of  $I$  and  $T_b$ . The nonlinear dependence of the resistance  $R$  on temperature, which is characteristic

of a superconducting nanowire, is at the root of this bistability. This bistability in turn furnishes the mechanism for the thermal hysteresis in the  $I - V$  characteristics; the two solutions correspond to the superconducting (cold solution) and the resistive (hot solution) branches of the hysteresis loop. To obtain the hysteresis loop at a given bath temperature  $T_b$ , one begins by solving Eq. (5.7) to obtain  $\Theta(x)$  at a bias current sufficiently low such that the equation yields only one solution. Next, by using the solution  $\Theta(x)$  from the previous step to initialize the equation solver for the next bias current step, the locally stable solution of Eq. (5.7) is traced out as a function of  $I$  by tuning the bias current first up and then down. The  $I - V$  loop is thus traced out by calculating the voltage,

$$V = \int_{-L/2}^{L/2} dx IR(\Theta(x)), \quad (5.9)$$

at each step.

The numerical analysis of Eq. (5.7) requires a knowledge of  $R(\Theta)$  and  $K_s(\Theta)$ , which serve as the input functions for the theory. In Ref. [24], the linear-response resistance measured at  $T_b = \Theta$  was used for  $R(\Theta)$ . However,  $R$  depends also on the value of the bias current  $I$ . Henceforth, we shall use  $R(\Theta(x), I)$  instead of  $R(\Theta(x))$ .

## II. Heating by discrete phase slip events: Derivation of Langevin equation

In the previous subsection we described the static theory of thermal hysteresis as was discussed in Ref. [24] in the context of experiments on MoGe nanowires. Let us go one step further and include dynamics by considering the time-dependent heat diffusion equation

$$C_v(\Theta) \partial_t \Theta(x, t) = \partial_x [K_s(\Theta) \partial_x \Theta(x, t)] + Q_{\text{source}}, \quad (5.10)$$

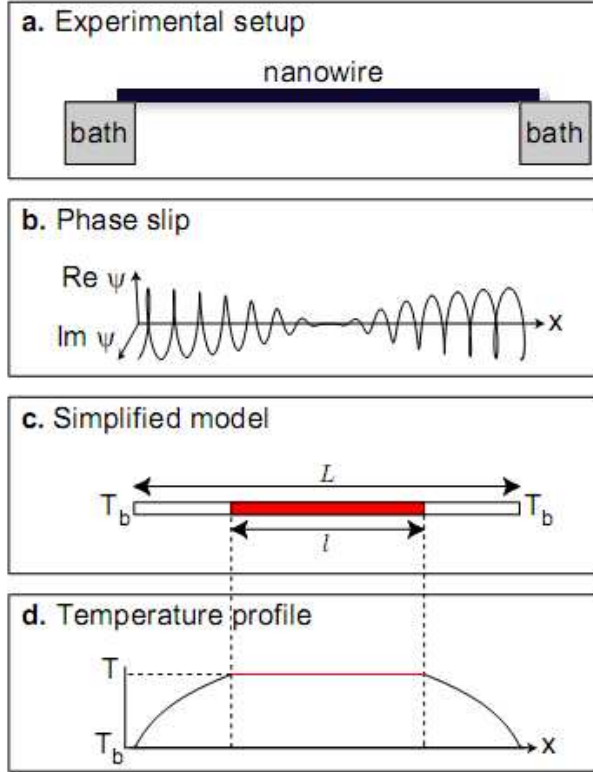


Figure 5.24: Sketch of the overheating model from Ref. [23]. (a) Schematic of the experimental configuration described by our model: a superconducting nanowire is suspended between two thermal baths. (b) Sketch showing the attenuation of the order parameter in the core of a phase-slip. (c) Schematic of the simplified model. All phase slips are taken to occur in a central (i.e. shaded) segment of length  $l$ , which is assumed to be at a uniform temperature  $T$ ; heat is carried away through the end segments, which are assumed to have no heat capacity. The temperature at the ends of the wire is fixed to be  $T_b$ . (d) Sketch of a typical temperature profile.

where the specific heat  $C_v(\Theta)$  enters as an additional input function. This differential equation can be derived in the standard way, by using the continuity equation,

$$\nabla \cdot j_Q + \partial_t Q = Q_{\text{source}} \quad (5.11)$$

for the heat current,

$$j_Q \equiv -K_s(\Theta)\nabla\Theta, \quad (5.12)$$

together with the energy density,

$$Q \equiv \int^{\Theta(x)} C_v(\Theta') d\Theta'. \quad (5.13)$$

However, as long as we assume that the wire is heated by the source term given by Eq. (5.6), the dynamic formulation turns out to be inadequate for our purposes, as should become clear from our analysis and results. Such a source term assumes that the wire is being continually heated locally as a result of its resistivity  $R(\Theta(x), I)A/L$  at any given position  $x$  along the wire. Is this assumption of continual Joule heating correct? To answer this question we need to deconstruct the resistance and get to its root. It needs to be emphasized that it is the resistive phase-slip fluctuations that are responsible for the characteristic resistance of a quasi-one dimensional wire. Therefore, one should thus consider the Joule heating as being caused by individual, discrete phase-slip events.

Let us then explicitly consider discrete phase-slip events (labelled by  $i$ ) that take place one at a time at random instants of time  $t_i$ , and are centered at random spatial locations  $x_i$ . By using the Josephson relation

$$\frac{d\phi}{dt} = \frac{2eV}{\hbar} = \frac{2\pi V}{\Phi_0} \quad (5.14)$$

relating the voltage pulse  $V(t)$  to the rate of change of the end-to-end phase difference across the wire  $\phi$ , we arrive at the work done on the wire by a phase slip, viz.,

$$Q_{\text{ps}} = \int dt IV = I \int_0^{2\pi} d\phi \frac{\hbar}{2e} = \Phi_0 I, \quad (5.15)$$

where  $\Phi_0 = h/2e$  is the superconducting flux quantum. Hence, a single phase slip (or anti-phase slip), which corresponds to a decrease (or increase) of  $\phi$  by  $2\pi$ , will heat (or cool) the wire by a “quantum” of energy  $Q_{\text{ps}}$ . Using this result, we can now write down a

time-dependent stochastic source term,

$$Q_{\text{source}}(x, t) \equiv \frac{Q_{\text{ps}}}{A} \sum_i \sigma_i F(x - x_i) \delta(t - t_i), \quad (5.16)$$

where  $F(x - x_i)$  is a spatial form factor, normalized to unity, representing the relative spatial distribution of heat produced by the  $i^{\text{th}}$  phase-slip event, and  $\sigma_i = \pm 1$  for phase (anti-phase) slips. The probability per unit time  $\Gamma_{\pm}$  for anti-phase (phase) slips to take place depends on the local temperature  $\Theta(x, t)$  and the current  $I$ .

Now, instead of using the continual Joule heating source term, Eq. (5.6), let us use the source term given by Eq. (5.16). Instead of being a deterministic differential equation, the heat diffusion equation (5.10) becomes a stochastic differential equation for  $T(x, t)$ . We thus have a Langevin equation with stochasticity, in one space and one time dimension, with a “noise” term that is characteristic of a jump process.

Let us try to understand the connection between the two source terms. By using the Josephson relation (5.14), we can express

$$R(\Theta, I) = \frac{V}{I} = \frac{1}{I} \frac{\Phi_0}{2\pi} \frac{d\phi}{dt} = \frac{\Phi_0 \Gamma(\Theta, I)}{I} \quad (5.17)$$

and use it to rewrite the continual Joule-heating source term, Eq. (5.6), as

$$Q_{\text{source}} = \frac{Q_{\text{ps}} \Gamma(\Theta, I)}{AL}, \quad (5.18)$$

where  $\Gamma \equiv \Gamma_- - \Gamma_+$ . Let us assume that a phase slip only affects its local neighborhood, i.e.,  $F(x - x_i) \sim \delta(x - x_i)$ . Then, if we take the continuum time-limit of Eq. (5.16) by assuming that the phase-slips are very frequent and that  $Q_{\text{ps}} \rightarrow 0$ , the two source terms would indeed become equivalent (as can also be seen formally by taking the limit  $\Phi_0 \rightarrow 0$ ).

We now make a brief remark about the switching current. The static theory of hysteresis that was discussed in the previous subsection has a single, well-defined value of the switching

current, which corresponds to the value of the bias current at which the low-temperature (superconductive) solution becomes unstable. On the other hand, we see from the theory discussed in the present subsection that the randomness in  $x_i$  and  $t_i$  generates a stochasticity in the switching process. The full implications of the stochastic dynamical theory will be discussed in the following sections.

### III. Simplified model: Reduced Langevin equation

In principle, one can proceed to study the physics of the stochastic switching dynamics of a current-biased nanowire by using the dynamics of Eq. (5.10) together with stochastic source Eq. (5.16), both derived in the previous subsection. In practice, however, it is not easy to solve the full Langevin equation with both spatial and temporal randomness. In this subsection we derive a simplified model, and argue that it is capable of capturing the physics essential for our purposes.

We concentrate on wires that are in the dirty limit, for which the mean free path is much shorter than the coherence length, which is shorter than the charge imbalance length required for carrier thermalization, which itself is somewhat shorter than  $L$ . In addition to restrictions on length-scales, we assume that the time for a phase-slip ( $\sim \tau_{\text{GL}}$ ) and the quasi-particle thermalization time  $\tau_{\text{E}}$  are both smaller than the wire cooling time, i.e., the time it takes the heat deposited in the middle of the wire by a phase-slip to diffuse out of the wire.

We will make a series of simplifications as follows:

1. Due to the presence of the superconducting leads at two ends as well as edge effects, it is more likely that the phase-slip fluctuations in the wire are centered away from the wire edges. We thus assume that the source term is restricted to a region near the center of the wire.
2. We assume that the heating takes place within a central segment of length  $l$ , to which

a uniform temperature  $T$  is assigned. Note that the total length  $L$  may be allowed to differ slightly from the geometric length of the wire, in order to compensate for the temperature gradients in the lead at the wire attachment point.

3. We assume that the heat is conducted away through the end segments, each of which are of length  $(L - l)/2$ . As an additional simplification, we ignore the heat capacity of these end segments.
4. To simplify the problem further, we make use of the fact that the probability per unit time (i.e., the characteristic rate)  $\Gamma_+$  for an anti-phase slip to take place is much smaller than the rate  $\Gamma_-$  for a phase slip to take place, and we thus ignore the process of cooling by anti-phase slips. To account indirectly for their presence, we use a reduced rate  $\Gamma \equiv \Gamma_- - \Gamma_+$  instead of  $\Gamma_-$ . This ensures that the discrete expression for  $Q$  correctly reduces to the continual Joule-heating expression.

With the simplified model defined above, the description of superconducting nanowires reduces to a stochastic ordinary differential equation for the time-evolution of the temperature  $T$  of the central segment:

$$\frac{dT}{dt} = -\alpha(T, T_b)(T - T_b) + \eta(T, I) \sum_i \delta(t - t_i). \quad (5.19)$$

This equation can be thought of as a reduced Langevin-type equation which is the counterpart of the full Langevin-type Eq. (5.10) with the source term Eq. (5.16) in the un-simplified model. The second term on the RHS of Eq. (5.19) corresponds to (stochastic) heating by phase slips, and the first to (deterministic) cooling as a result of conduction of heat from the central segment to the external bath via the two end-segments. The temperature-dependent cooling rate,  $\alpha(T, T_b)$ , is obtained by comparing the heat currents through the end segments to the thermal mass of the central segment, where the heat currents through the end segments are found by solving the heat equation in the end segments subject to the

boundary conditions that  $T(0) = T(L) = T_b$  and  $T(\frac{L-l}{2}) = T(L - \frac{L-l}{2}) = T$ .

$$\alpha(T, T_b) \equiv \frac{4}{l(L-l)C_v(T)} \frac{1}{T - T_b} \int_{T_b}^T dT' K_s(T'). \quad (5.20)$$

If  $T_i$  and  $T_f$  are temperatures of the central segment before and after a phase slip then we can express the temperature ‘impulse’ due to a phase slip, i.e.,  $T_f - T_i \equiv \eta(T_i, I) \equiv \tilde{\eta}(T_f, I)$ , as function of either  $T_i$  or  $T_f$  (depending on the context) by using

$$A l \int_{T_i}^{T_f} C_v(T') dT' = Q_{ps}. \quad (5.21)$$

To summarize, in this section we have derived a simplified model that is described by the reduced Langevin equation (5.19). The central assumption that we used to build this simplified model is that phase-slips predominantly occur in the center of the nanowire, or at least their exact spatial locations are unimportant. This assumption is appropriate for shorter nanowires, in which we do not have several distinct locations along the wire at which a switching event may nucleate. Specifically, if the wire length does not greatly exceed the charge imbalance length (which itself is assumed to be much larger than the coherence length), then independent of where a phase-slip occurs the temperature profile in the wire after the phase slip will be similar, and we can use our simplified time-only model.

## 5.8.2 Input functions and parameters

In this appendix we list the models for phase-slip rate, specific heat, and thermal conductivity that go into the stochastic heat equation (5.10).

## Phase-slip rate

We begin by considering the phase slip rate. For the TAPS rate we have used the LAMH model, including the non-linear current response

$$\Gamma_{\text{TAPS}}(I, T) = \Gamma_{-, \text{TAPS}}(I, T) - \Gamma_{+, \text{TAPS}}(I, T) \quad (5.22)$$

$$\Gamma_{\pm, \text{TAPS}}(I, T) = \Omega_{\pm}(I, T) \exp\left(-\frac{\Delta F_{\pm}(I, T)}{k_B T}\right) \quad (5.23)$$

where, + and - indicates whether the phase-slip results in current rise or current drop respectively. The phase-slip barrier at bias current  $I$  and temperature  $T$  is

$$C_1(T) = \frac{3\sqrt{3}}{8} \frac{\hbar}{2e} I_c(T) \quad (5.24)$$

$$\Delta F_-(T) = C_1(T) \left( \frac{8}{3} \sqrt{2} \sqrt{1-3k^2} - 8k(1-k^2) \arctan \frac{\sqrt{1-3k^2}}{\sqrt{2}k} \right) \quad (5.25)$$

$$\Delta F_+(T) = C_1(T) \left( \frac{8}{3} \sqrt{2} \sqrt{1-3k^2} + 8k(1-k^2) \left[ \pi - \arctan \frac{\sqrt{1-3k^2}}{\sqrt{2}k} \right] \right) \quad (5.26)$$

where the phase gradient  $k$  is the real solution of

$$\frac{I}{I_c(T)} = k(1-k^2), \quad (5.27)$$

and the temperature dependent critical current  $I_c(T)$  [57] is expressed in terms of the wire length  $L$ , critical temperature  $T_c$ , zero temperature coherence length  $\xi(0)$ , and the normal state resistance of the wire  $R_n$  [58]

$$I_c(T) = (92 \mu\text{A}) \frac{L T_c}{R_n \xi_0} \left( 1 - \left( \frac{T}{T_c} \right)^2 \right)^{3/2}. \quad (5.28)$$

We approximate the prefactor  $\Omega_{\pm}(I, T)$  via

$$\Omega(T) = \frac{\sqrt{3}}{2\pi^{3/2}} \frac{L}{\xi(T)\tau(T)} \left( \frac{\Delta F(I=0, T)}{k_B T} \right)^{1/2} \quad (5.29)$$

$$\Omega_-(I, T) = (1 - \sqrt{3}k)^{15/4} (1 + k^2/4) \Omega(T) \quad (5.30)$$

$$\Omega_+(I, T) = \Omega(T). \quad (5.31)$$

In the presence of a bias current, the “+” phase slips are exponentially more rare than the “-” phase-slips. Therefore, we keep the current corrections to the prefactor for the “-” phase-slips, but not the “+” phase slips. Thus we get an approximation which works in both linear-response regime where the current correction is irrelevant and in the high bias regime where “+” phase slips are rare. We estimate the temperature dependent coherence length and the Ginzburg-Landau time via

$$\xi(T) = \xi(0) \sqrt{1 - (T/T_C)^4} / (1 - (T/T_C)^2) \quad (5.32)$$

$$\tau(T) = \pi\hbar/8k_B(T_C - T). \quad (5.33)$$

Thus, we can express the phase slip rate via  $L$ ,  $R_n$ ,  $\xi(0)$ ,  $T_C$ .

To obtain the quantum phase-slip rate, we replace  $T$  in the denominator of the exponential function of Eq. (5.23) by the effective temperature  $T_{\text{eff}} = T_0 + T_1 T$ , where  $T_0$  and  $T_1$  are treated as fitting parameters.

### Heat capacity and thermal conductivity

Unfortunately, there is no direct experimental data on the heat capacity and thermal conductivity of current carrying superconducting nanowires. The diameter of the wires used in experiments is comparable to  $\xi(0)$ . Thus, thermodynamic properties of these wires should be somewhere between those of a bulk superconductor and a normal metal. Therefore, for the purposes of computing the thermodynamic functions we model the wire as being composed

of a BCS superconducting wire with cross-section  $A_1$  in parallel to a normal metal wire with cross-section  $A_2$ .

The BCS and Fermi liquid expressions for heat capacity [30] are

$$C_{v,\text{BCS}} = -\frac{2N_0}{T} \int E_k \frac{df_k}{d(\beta E_k)} \left( E_k + \beta \frac{dE_k}{d\beta} \right) d\xi_k, \quad (5.34)$$

$$C_{v,\text{FL}} = \frac{2}{3} \pi^2 N_0 k_B^2 T, \quad (5.35)$$

where  $\beta = 1/k_B\Theta$ ,  $E_k = \sqrt{\xi_k^2 + \Delta^2(\Theta)}$ ,  $f_k$  is the Fermi function and  $\Delta(\Theta)$  is obtained from the BCS gap equation. Thus the total heat capacity of the wire is

$$C_v = \frac{A_1 C_{v,\text{BCS}} + A_2 C_{v,\text{FL}}}{A_1 + A_2}. \quad (5.36)$$

Similarly, the dirty limit BCS [59] and Fermi liquid expressions for thermal conductivity are

$$K_{s,\text{BCS}}(\Theta) = 2N_0 D \int_{\Delta}^{\infty} \frac{\text{sech}^2 \left[ \frac{\epsilon}{2k_B\Theta} \right]}{2k_B\Theta} \frac{\epsilon^2}{k_B\Theta} d\epsilon, \quad (5.37)$$

$$K_{s,\text{FL}}(\Theta) = \frac{L_0 \Theta L}{AR_n} \quad (5.38)$$

where  $D$  is the diffusion constant (for MoGe  $D \sim 1 \text{ cm}^2/\text{s}$  [51]), and  $L_0 = \pi^2 k_B^2 / 3e^2$ . The total heat conductivity is

$$K_s = \frac{A_1 K_{s,\text{BCS}} + A_2 K_{s,\text{FL}}}{A_1 + A_2}. \quad (5.39)$$

The fitting parameters describing heat capacity and heat conductivity are the cross-sections  $A_1$  and  $A_2$ , and the  $T_C$  of the nanowire.

### 5.8.3 Comparison with experimental data

In this section, we compare results from our experiments with predictions of our theory. We show that our theory is both qualitatively and quantitatively consistent with experimental observations. The main implication of the comparison are: (1) the switching-current distribution-width does indeed increase as the temperature is decreased; (2) there is a single phase-slip-to-switch regime at low temperatures; and (3) thermally activated phase-slips, alone, are insufficient to fit the dependence of the mean switching time on the bias current at low temperatures which suggests that we should include quantum phase-slips; upon including quantum phase-slips phenomenologically, we can obtain good fits to the experimental data in the low temperature regime as well. This section is structured as follows. To establish the validity of the thermal hysteresis model, we begin by analyzing the  $I$ - $V$  hysteresis loops. Next, we qualitatively analyze the experimentally measured switching current distribution. We continue with a quantitative analysis of the experimental data on the mean switching rate.

#### I. $I - V$ hysteresis loops

We begin our analysis by comparing the qualitative features of the experimentally measured and theoretically computed current-voltage characteristics. Experimentally it is found that at high temperatures there is no hysteresis. As  $T_b$  is lowered, a hysteresis loop gradually opens up. Next, as the temperature is lowered even further, the switching current (i.e., the bias current at the superconducting-resistive transition) grows gradually, whilst the re-trapping current (i.e., the bias current at the resistive-superconducting transition) remains almost unchanged. This behavior is consistent with the experimental observations and the theory of Ref. [24], where this is also qualitatively explained as follows. Switching is controlled by the properties of the low-temperature (i.e., superconducting-like) solution which depends strongly on the temperature of the bath  $T_b$ . On the other hand, re-trapping is largely a property of the hotter (i.e., resistive) state, and thus has only a weak dependence

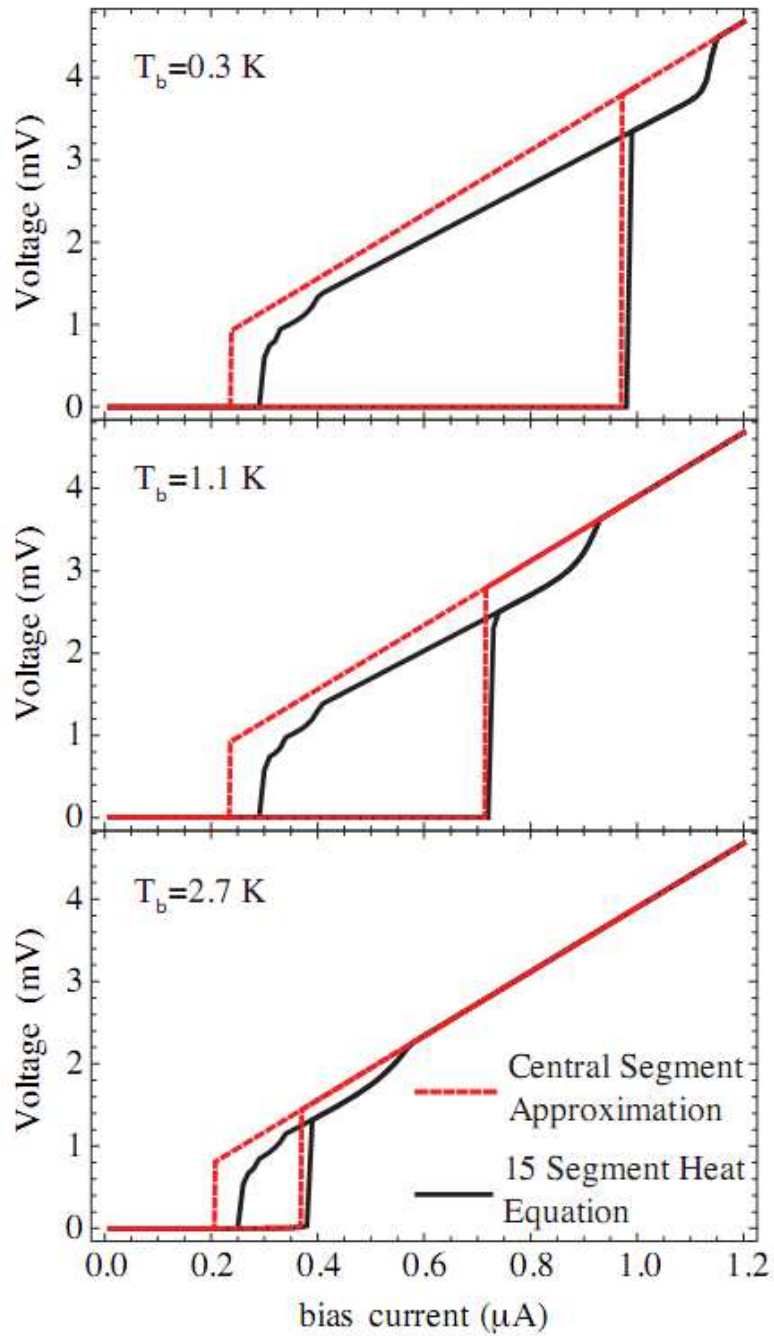


Figure 5.25: Comparison of  $I$ - $V$  hysteresis loops computed using central segment approximation and the full heat equations. For the case of the heat equation the wire was split into 15 segments. The steps in the high voltage branch of the segmented solution correspond to various segments becoming superconducting. These steps would disappear in the continuum limit.

on  $T_b$ .

Typical  $I$ - $V$  curves obtained from the central segment model as well as those obtained from solving the heat equation are shown in Fig. 5.25 for several bath temperatures  $T_b$ . Following Ref. [24], the solutions of the heat equation were obtained from a spatially discretized version of Eq. (5.7). The theoretical curves both qualitatively and quantitatively reproduce the features seen in experiments. We take a moment to point out that for fitting experimental data it is important to take into account the non-linear dependence of the phase-slip rate on the bias current. Finally, we point out that making the central segment approximation has little effect on the switching current found in the hysteresis loops (for typical wires used in experiments). This fact supports the validity of the central segment approximation for computing switching phenomena.

## II. Switching current distributions

In experiments, every time an  $I - V$  characteristic is measured by sweeping the bias current up and down, switching occurs at a different value of the bias current. By repeatedly measuring the hysteresis loop at a fixed bath temperature  $T_b$  and current sweep rate  $dI/dt$ , one can obtain the distribution of switching currents  $P(I_{sw}, T_b, dI/dt)$ . Typical  $P(I_{sw}, T_b, dI/dt)$  distributions, obtained experimentally, are shown in Fig. 5.26. For completeness, we also show the corresponding theoretical fits, which we shall describe in detail in the next subsection. For a given  $T_b$ , switching events, in general, tend to occur at lower bias currents than the switching current found in the thermodynamic stability analysis of Ref. [24]. The reason for this premature switching at bias currents that are lower than the stability analysis indicates is thermally activated barrier crossing in the form of a phase-slip cascade. In Fig. 5.27 we plot the mean and the standard deviation of the switching-current distributions measured experimentally, as well as those obtained from theoretical fits of the simplified model. Using the tuning parameters obtained from the fits, we also plot the theoretical de-pairing critical current and the critical current from the stability analysis of the simplified model.

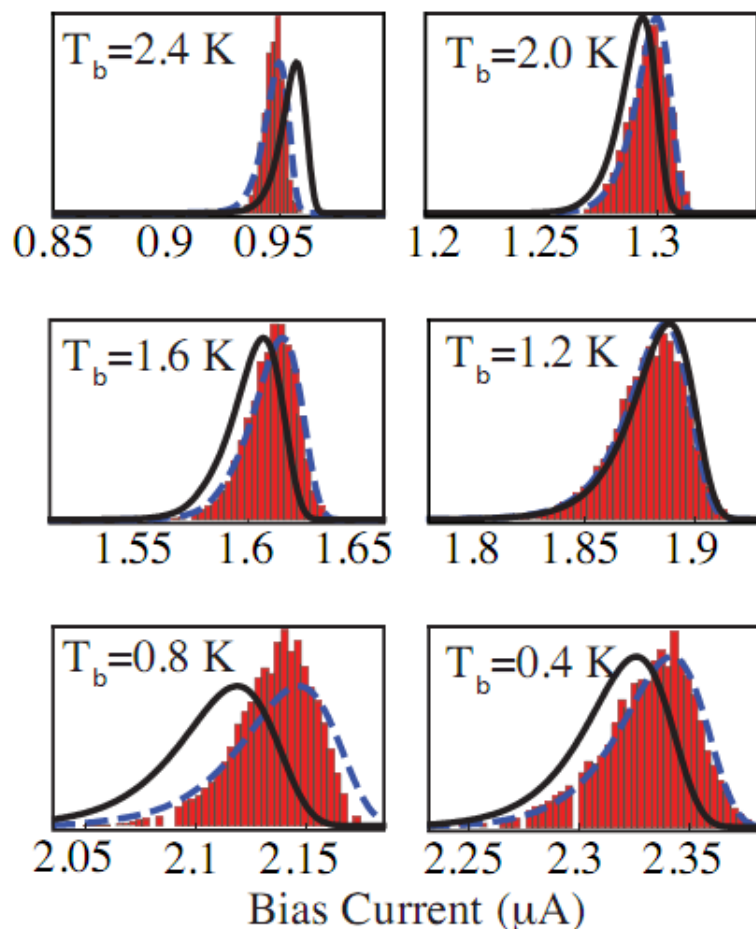


Figure 5.26: Experimental data (red bar charts) and theoretical fits (black lines) for the switching current distributions for various bath temperatures. To make the comparisons between the shapes of distributions easier, we shifted the theoretical curves (blue dashed lines) so that their means coincide with the experimental curves.

As described before, one would typically expect the standard deviation of the switching-current distribution to *decrease* with decreasing temperature, as thermal fluctuations are suppressed. Such narrowing of the switching-current distribution is expected to continue with cooling until the temperature becomes sufficiently low such that *quantum* phase slips are the main drivers of the switching, at which point the narrowing is expected to come to a halt. Qualitatively, this would indeed be the case if switching was always triggered by a single phase-slip. However, our theory, predicts that the situation is more complicated because the mean switching time, and hence the width of the switching-current distribution,

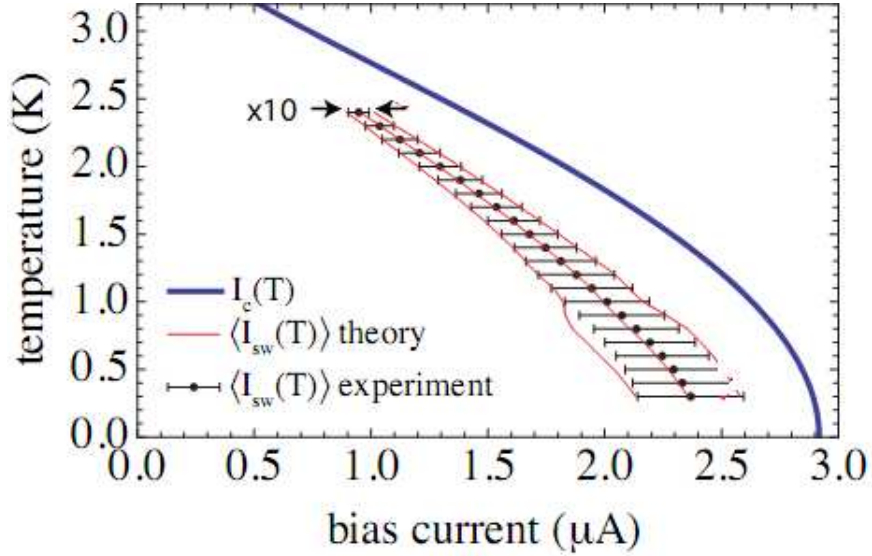


Figure 5.27: Hierarchy of critical and switching currents. All theoretical curves were produced using the parameters obtained from fitting experimental data. Highest current scale is the depairing critical current  $I_c(T)$ . Next, is the actual switching current  $I_{sw}(T)$ . The error bars on the switching current correspond to the  $10\times$  the standard deviation of the switching current distribution (the scale of the standard deviation was exaggerated to make it easier to see, the sweep rate was set to  $58 \mu\text{A/s}$ ).

is controlled by a competition between the phase-slip rate and the number of consecutive phase-slips needed to induce switching, as described in the previous section. Thus, qualitatively, we expect the opposite behavior at higher temperatures. That is, in the regime of thermally activated phase slips and at temperatures above the single phase-slip-to-switch regime, the width of the switching-current distribution should *increase* with decreasing temperature. This counter-intuitive broadening of the switching current distributions with decreasing temperature is indeed observed experimentally, as shown in Fig. 5.10.

In fact, all samples that have been studied show monotonic broadening with decreasing temperature down to the lowest accessible temperature of 277 mK.

### III. Mean switching rate

As the switching-current distribution depends on the bias current sweep rate, in order to quantitatively compare our theory with experimental data, we focus on the mean switch-

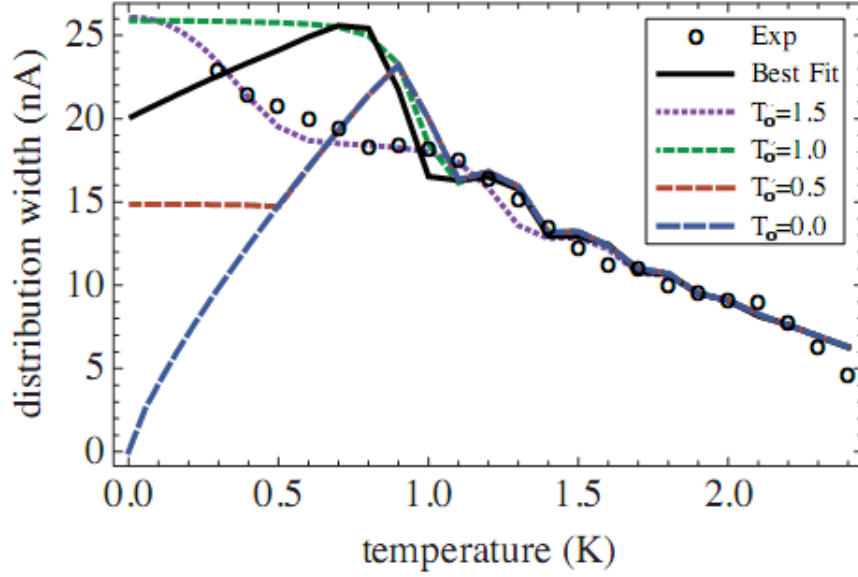


Figure 5.28: The standard deviation of the switching current distribution as a function of temperature. Comparison of experimental data for a typical sample (circles) with various QPS scenarios labeled by  $T_0$ . The “best fit” curve was obtained using parameters in Table 5.1 (with  $T_0 = 0.726$ ), where the fit was optimized to simultaneously capture the dependence of mean switching current and the standard deviation of the switching current distribution on temperature.

ing rate, which is related to the switching current distribution. The mean switching time  $\tau$  in bistable current-biased systems can be measured directly by performing waiting-time experiments. Alternatively,  $\tau$  can be extracted from switching-current statistics[55]. The switching-current distribution can be generated via the repeated tracing of the  $I$ - $V$  characteristic, ramping the current up and down at some sweep rate

$$\frac{dI}{dt} = r.$$

The sweep-rate-dependent probability  $P(I, T_b; r)dI$  for the event of switching (from the superconductive to the resistive branch) to take while the current is in the range  $I$  to  $I + dI$

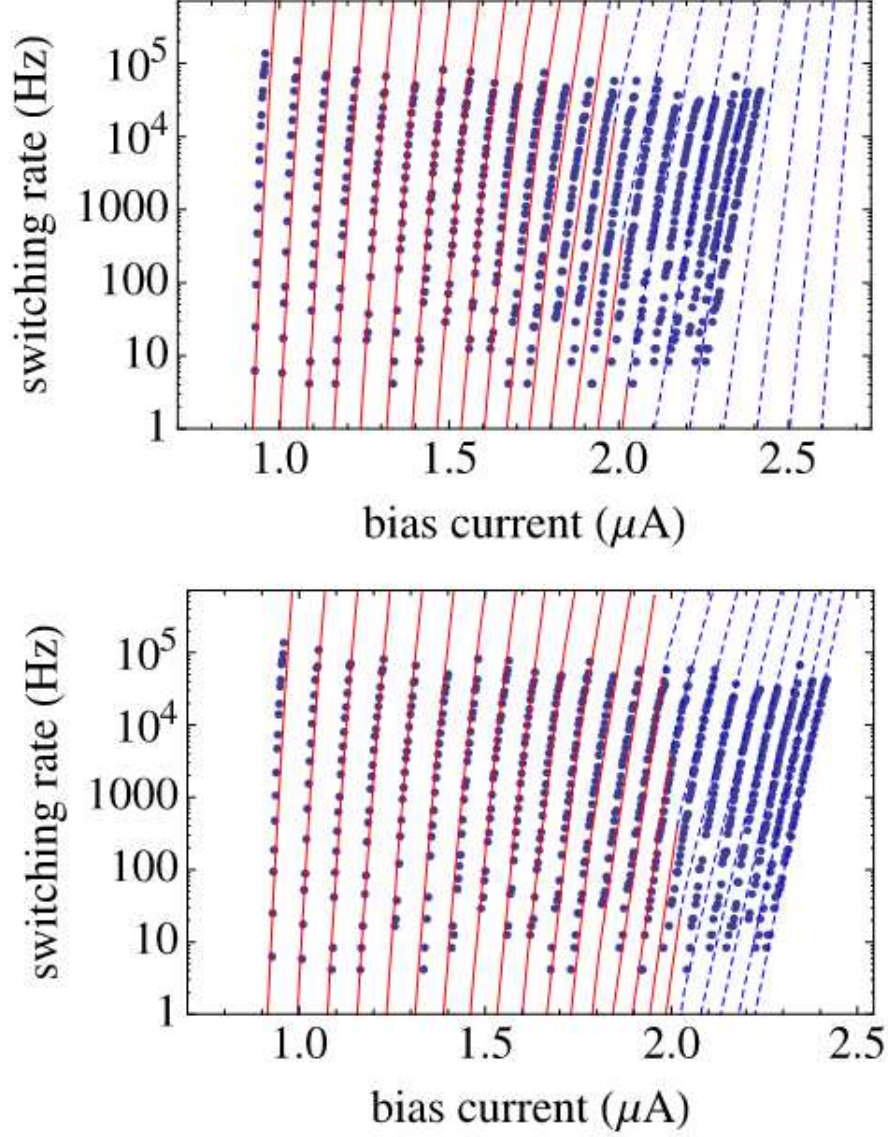


Figure 5.29: Comparison of theoretical fits (lines) to the experimental (blue dots) Mean Switching Rates. The top panel shows fits with thermally activated phase slips only, while the bottom panel includes both thermally activated and quantum phase slips. The solid red lines correspond to multiple-phase-slips-to-switch regime, while the dashed blue lines correspond to multiple-phase-slips-to-switch regime.

can explicitly be related to the mean switching time  $\tau$  via the relation

$$P(T_b, I; r)dI = \left( \tau^{-1}(T_b, I) \frac{dI}{r} \right) \times \left( 1 - \int_0^I P(T_b, I'; r) dI' \right). \quad (5.40)$$

The term in the first parenthesis corresponds to the probability for switching to happen within the ramp time, while the term in the second parenthesis corresponds to the probability that the wire has not already switched before reaching the bias current  $I$ . The experimentally obtained mean switching rate  $\tau^{-1}(I, T_b)$  for a typical sample, along with theoretical fits, are plotted as a function of the bias current  $I$  for different values of the lead temperature  $T_b$  in Fig. 5.29. To help relate the mean switching rate to the switching current distribution width, we note that for a fixed  $T_b$ , the shallower the slope of  $\tau^{-1}(I, T_b)$  the wider the corresponds distribution. The two main features of the experimental data plotted in Fig. 5.29 are as  $T_b$  decreases (1) the mean switching rate decreases ( $\langle I_{sw} \rangle$  increases) and (2) the slope of  $\tau^{-1}(I)$  decreases ( $I_{sw}$  distribution width becomes wider).

Two different fits to the same set of experimental data are shown in Fig. 5.29. The fit shown in the top panel includes TAPS only while the one in the bottom panel uses the fitting parameters from the top panel, but also includes QPS. The tuning parameters that were used to obtain the fits fall into two categories. The first category is composed of the geometric model parameters such as the wire length, while the second category controls the “input functions,” i.e. the heat capacity, the heat conductivity, and the phase-slip rate. The expressions for these input functions are given in Eqs. (-) of Appendix ???. In obtaining these fits, we ensure that the fitting parameters that we used are consistent with the high temperature  $R(T)$  data.

The TAPS only fit (top panel Fig. 5.29) works well at temperatures above 1 K. In this regime the theory is able to quantitatively explain the observed rise in  $\langle I_{sw} \rangle$  with decreasing temperature as well as the peculiar increase the  $I_{sw}$  distribution width with decreasing temperatures.

#### IV. Single-slip-to-switch regime

In general, as the temperature is lowered and the bias current is increased, the wire tends to enter the single-slip-to-switch regime as indicated in Fig. 5.30. This regime roughly

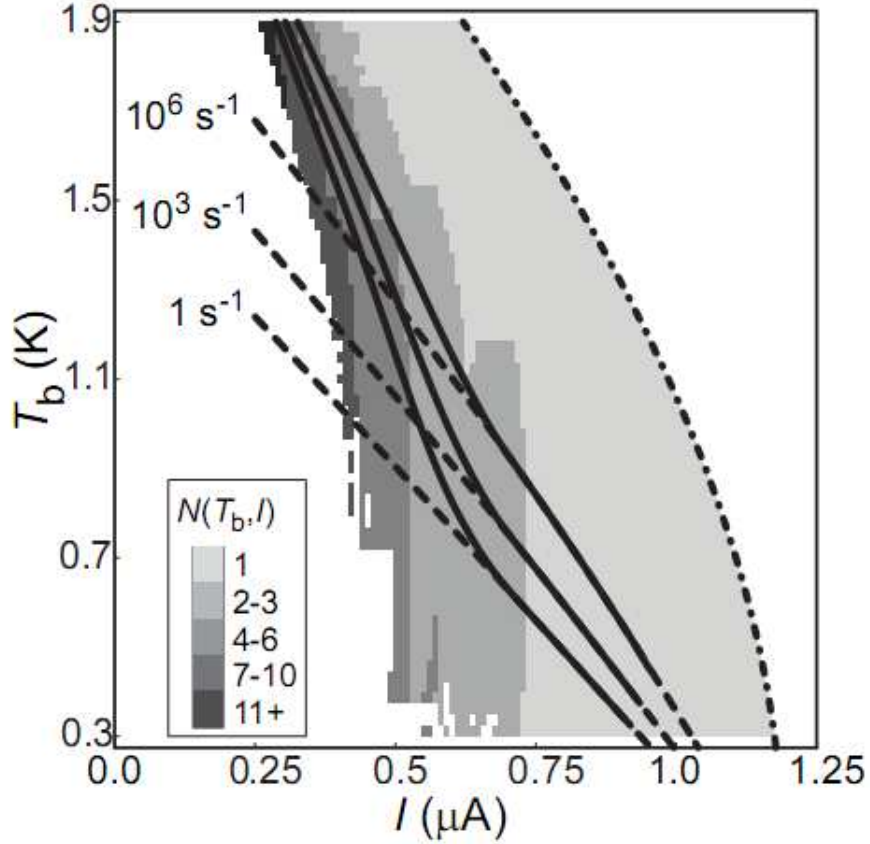


Figure 5.30: Map of  $N(T_b, I)$  the number of consecutive phase slips required to overcome the barrier and induce the wire to switch as a function of bias current  $I$  and bath temperature  $T_b$ . The three solid lines indicate the contours along which  $\Gamma_{sw}^{-1}$  (the mean switching rate) is 1,  $10^3$ , and  $10^6$   $s^{-1}$ . Similarly, the three dashed lines indicate the contours along which the phase slip rate is 1,  $10^3$ , and  $10^6$   $s^{-1}$ . For comparison, the depairing critical current is indicated by the dashed-dotted line.

corresponds to the region of the  $(I, T)$  plane where a single phase slip heats up the wire to  $T_C(I)$ , and thus the boundaries of this regime are primarily determined by the heat capacity of the wire. When working within regime, switching current statistics correspond directly to the phase-slip statistics.

Theoretical fitting indicates that at temperatures below 1 K the wire enters the single-phase-slip-to-switch regime. This regime is indicated by the switch of the theory curves from solid red lines to dashed blue lines in Fig. 5.29. In the absence of quantum phase slips, in this regime the  $I_{sw}$  distribution width should follow a more conventional behavior

and decreases with temperature. This corresponds to the increase in the slope of the mean switching rate curves with decreasing temperature in the single-slip-to-switch regime (see top panel of Fig. 5.29).

However, experimentally the distribution width seems to increase monotonically as the temperature is lowered, even in the single-slip-to-switch regime. This behavior suggests that there is an excess of phase slips at low temperatures.

## V. Quantum phase-slip scenarios

We expect that at low temperatures quantum phase-slips can strongly contribute to the switching rate. We model the presence of QPS by adding their rate to the rate of TAPS to obtain the total phase-slip rate which goes into our model

$$\Gamma_{\text{total}}(I, T) = \Gamma_{\text{TAPS}}(I, T) + \Gamma_{\text{QPS}}(I, T). \quad (5.41)$$

To model the QPS rate,  $\Gamma_{\text{TAPS}}(I, T)$ , we replace  $T \rightarrow T_0 + T_1 T$  in  $\Gamma_{\text{QPS}}(I, T)$ . Here,  $T_0$  and  $T_1$  are both treated as fitting parameters. Letting  $T_1$  be nonzero does somewhat improve the quality of our fits.

We can envision several scenarios for the effect of QPSs on the switching current distributions, these are summarized in Fig. 5.28. In the absence of QPS, upon lowering the temperature, once the single-slip-to-switch regime is reached the distribution width will start decreasing with temperature. This type of behavior is demonstrated by the  $T_0 = 0$  line in Fig. 5.28. However, in the presence of QPS, the distribution width is expected to saturate at low temperature, with the saturation value controlled by  $T_0$ . If, upon cooling, the single-slip-to-switch regime is reached before the temperature reaches  $T_0$ , we expect the distribution width increases and then decrease before saturating with decreasing temperature ( $T_0 = 0.5$  K curve in Fig. 5.28). On the other hand, if  $T_0$  is reached before the single-slip-to-switch regime, we expect the distribution width increases monotonically with decreasing

temperature ( $T_0 = 1.0, 1.5$  K curves in Fig. 5.28).

To include QPS in our fitting, we started with parameters obtained by fitting the mean switching rate curves at high temperatures ( $T > 1$  K) as described in the previous subsection (See top panel of Fig. 5.29). Next we optimized  $T_0$  and  $T_1$  to obtain best possible fit to the mean switching rate curves at low temperatures as well. The optimal values thus obtained were  $T_0 = 0.726$  K and  $T_1 = 0.4$ , which corresponds to the fit shown in the bottom panel of Fig. 5.29 and the curve labeled “best fit” in Fig. 5.28.

To fit experimental data, we must be able to simultaneously match both the mean and the standard deviation of the switching current distribution as a function of temperature. However, we have not been able to get quantitative agreement with both, simultaneously, in the low temperature regime. The parameter values  $T_0 = 0.726$  K and  $T_1 = 0.4$  result in a good fit of the mean but not the standard deviation (see Fig. 5.29 and 5.28), while the values  $T_0 = 1.5$  K and  $T_1 = 0$  result in a good fit of the standard deviation (see Fig. 5.28) but not the mean (not shown).

We conclude this section by noting that our fitting seems to favor the QPS scenario where the single-slip-to-switch regime occurs at a lower temperature than  $T_0$ .

# Chapter 6

## Multiple-retrapping process in high- $T_c$ Josephson junctions

In this chapter we report measurements of switching current distribution (SWCD) from a phase diffusion branch (PDB) to a quasiparticle tunneling branch (QTB) as a function of temperature in a cuprate-based intrinsic Josephson junction. Contrary to the thermal-activation model, the width of the SWCD increases and the corresponding switching rate shows a nonlinear behavior with a negative curvature in a semi-logarithmic scale with decreasing temperature, down to 1.5 K. Based on the multiple retrapping model, we quantitatively demonstrate that the frequency-dependent junction quality factor, representing the energy dissipation in a phase diffusion regime, determines the observed temperature dependence of the SWCD and the switching rate. We also show that a retrapping process from the QTB to the PDB is related to the low-frequency limit damping.

This work was done in collaboration with Myung-Ho Bae, Hu-Jong Lee and A. Bezryadin. The results and text of this chapter were published under the title “Multiple-Retrapping Process in Phase-Diffusion Regime of High- $T_c$  Intrinsic Josephson Junction” and are repeated here. reprinted with permission from Myung-Ho Bae, M. Sahu, Hu-Jong Lee, A. Bezryadin Phys. Rev. B **79**, 104509 (2009) Copyright 2009 by the American Physical Society.

### 6.1 Introduction

The escape of a system trapped in a metastable state governs the reaction rate in various dynamical systems, where the escape is made by a noise-assisted hopping [60]. In the case of a Josephson junction (JJ), a thermal noise induces an escape of a phase particle

representing the system from a local minimum of the potential well. In an *underdamped* JJ with hysteresis in the voltage-current ( $V$ - $I$ ) characteristics a single escaping event induces a switching from a zero-voltage phase-trapped state to a finite-voltage phase-rolling state, which gives a switching current,  $I_{SW}$  [55]. In an *overdamped* JJ without hysteresis, however, the energy of an escaped phase particle is strongly dissipated during its motion so that the particle is retrapped in another local minimum of the potential. The phase particle repeats this thermally activated escape and retrapping process, *i.e.*, the multiple-retrapping process in an overdamped JJ. It results in a phase-diffusion branch (PDB) with a small but finite voltage for a bias current below the critical current [30]. A hysteretic JJ can also evolve into this multiple-retrapping regime if the temperature is sufficiently high [61]. Recently, this phase-retrapping phenomenon in JJ's with hysteresis, including cuprate-based intrinsic Josephson junctions (IJJ's), has been intensively studied in association with the temperature dependence of a switching current distribution (SWCD) [62, 63, 64]. The main finding of these studies is that the retrapping process in the hysteretic JJ modifies the switching dynamics, in such a way as to *reduce the width of SWCD with increasing temperature*. This SWCD behavior, contrasting to the usual thermal activation model, has also been suggested to be caused by the enhanced dissipation due to a frequency-dependent impedance [65]. The impedance of the measurement lines ( $Z_L = 50\sim 100 \Omega$ ) is the main source of the high-frequency dissipation. As the dissipation of a JJ is represented by its quality factor, the previous studies have focused only on the moderately damped regime of quality factor  $\sim 5$ , where the  $V$ - $I$  curves with the SWCD's do not exhibit PDB's because the rate of the phase diffusion is too low to show a finite voltage at the temperatures studied. Thus, although the PDB itself has been extensively studied in conventional JJ and IJJ systems [66, 67, 61, 68, 69], the switching dynamics between a PDB and a quasiparticle-tunneling branch (QTB) has not been clearly resolved in terms of the quality factor.

Here we report switching from the PDB to the QTB in IJJs of  $\text{Bi}_2\text{Sr}_2\text{CaCu}_2\text{O}_{8+x}$  (Bi-2212) at various temperatures below  $T = 4.2$  K. Temperature dependence of the switching

rate  $\Gamma_S$  and the corresponding SWCD in a single IJJ are in good agreement with those estimated by the multiple-retrapping model. This study clarifies, in a quantitative manner, how the shunt impedance- and temperature-related dissipations, and the corresponding frequency-dependent quality factor  $Q(\omega)$  determine the switching dynamics in a hysteretic IJJ with phase-diffusion characteristics. In the relevant frequency range the quality factor was between 1.3 and 2.4. We show that the retrapping dynamics from the QTB to the PDB is determined by the low frequency limit damping.

## 6.2 Experiments

A stack of IJJ's with the lateral size of  $2.5 \times 2.9 \mu\text{m}^2$  in Bi-2212 single crystal was defined using focused-ion-beam (FIB) process as shown in the lower inset of Fig. 6.1a [70], where the stack under measurements was the blue-colored region in the corresponding schematic in the upper inset of Fig. 6.1. High-intensity FIB irradiation on a single crystal is known to degrade the peripheral region by the scattered secondary ion beam. In the milling process, we used a relatively high ion-beam current of 3 nA, corresponding to an intensity of  $\sim 200 \text{ pA}/\mu\text{m}^2$ . This high ion-beam current reduced the interlayer tunneling critical current density down to  $\sim 8 \text{ A}/\text{cm}^2$  in  $N = 12$  junctions out of total  $\sim 100$  IJJ's in the stack, which were estimated from the number of QTB's in  $V$ - $I$  curves of the stack (not shown). Four-terminal transport measurements [see the upper inset of Fig. 6.1a ] were carried out in a pumped  $\text{He}^4$  dewar with the base temperature of 1.45 K. Room-temperature  $\pi$ -filters were employed and measurement lines were embedded in silver paste at cryogenic temperatures to suppress high-frequency noises propagating along the leads. The measurements were made by using battery-operated low-noise amplifiers (PAR-113). The ramping speed of the bias current and the threshold voltage (obtained from the maximum voltage of the resistive branch below  $I_{SW}$ ) in measuring switching current ( $I_{SW}$ ) were  $\dot{I} = 30 \mu\text{A}/\text{sec}$  and  $V_{th} = 110 \mu\text{V}$ , respectively. Measurements were made on the first jump, which connected the resistive branch to the first

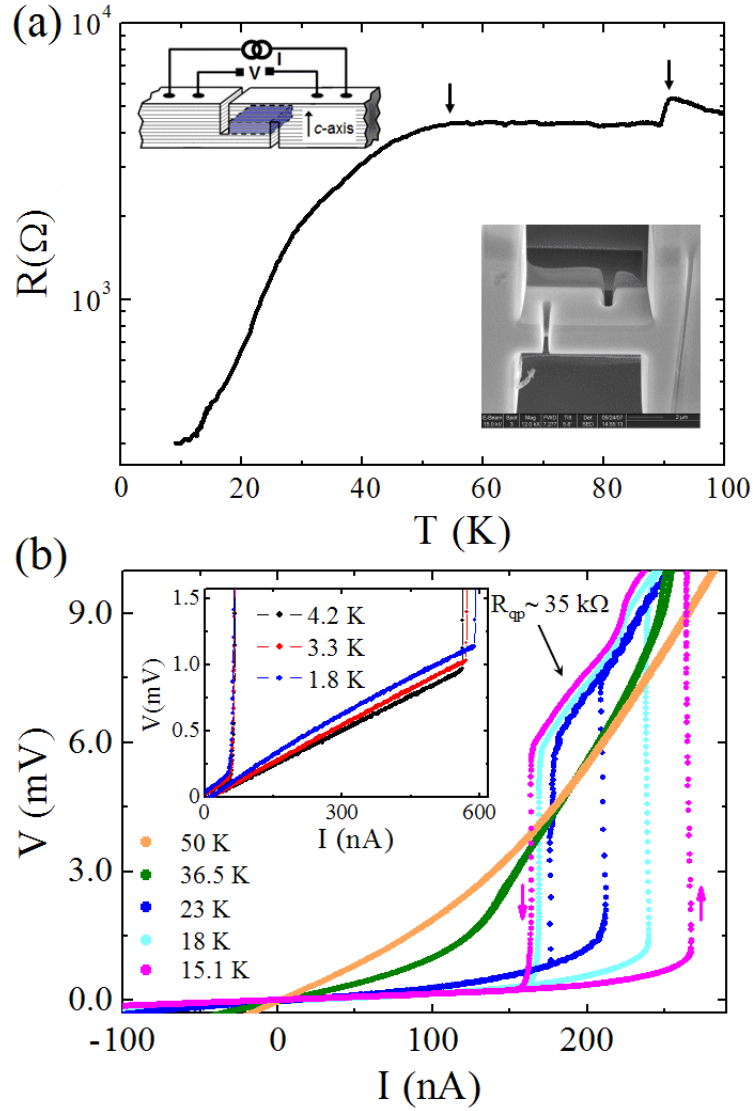


Figure 6.1: (a)  $R$  vs  $T$  curve of the sample stack, where  $T_c$  of the crystal is indicated by the right arrow. The left arrow indicates the critical temperature of the phase-diffusive junctions. Upper inset of (a): schematics for the sample and the measurement configurations. Lower inset of (a): Scanning electron microscope image of the measured sample. (b)  $V$ - $I$  characteristics at various temperatures of the Bi-2212 IJJs stack. The upward and downward arrows indicate the switching and the return currents, respectively, at  $T = 15.1$  K, where a resistance of the QTB,  $R_{qp} \sim 35$  k $\Omega$ . Inset of (b):  $V$ - $I$  curves of the sample at  $T = 1.8$  K, 3.3 K, and 4.2 K, show the resistance increase with cooling in this region of temperature, possibly due to presence of a normal segment in the stack.

QTB of the weakest junction in the stack. For each distribution, 10000 switching events were recorded with the current resolution of 90 pA.

### 6.3 Results and discussion

Fig. 6.1(a) shows the  $R$  vs  $T$  curve of our stacked junction device, which reveals a superconducting transition at  $T_c = 90$  K as indicated by the right arrow. The  $c$ -axis tunneling nature in the Bi-2212 stacked junctions is evident by the increasing resistance with decreasing temperature above  $T_c$ . The resistance in the temperature range  $54 \text{ K} < T < T_c$  originates from weakly superconducting layers [71], which have a suppressed critical temperature due to a degradation caused by the high-intensity ion beam in the FIB process. The critical temperature of these layers is about 54 K as shown by the left arrow. The resistance at  $T < 54$  K, however, does not vanish completely, even down to  $T = 10$  K, which is attributed to the phase diffusion in the weakened-superconductivity junctions and/or presence of non-superconducting junctions in the stack. Fig. 6.1(b) shows the  $V$ - $I$  curves at various temperatures below  $T = 54$  K. The nonlinear curve at  $T = 50$  K begins to show a hysteresis below  $T \sim 30$  K. At current lower than  $I_{SW}$  the resistance of the resistive branch decreases with decreasing temperature, where the finite resistance is caused by the phase diffusion [30]. The inset of Fig. 6.1(b) shows the hysteretic  $V$ - $I$  curves at  $T = 1.8$  K, 3.3 K and 4.2 K. Contrary to the  $V$ - $I$  curves in Fig. 6.1(b), which show a positive curvature below  $I_{SW}$  representing the PDB, the  $V$ - $I$  curves in the inset are characterized by small but negative curvatures. The resistance of the branch below  $I_{SW}$  even increases with decreasing temperature. We speculate that these behavior should originate from non-superconducting layers, which may be strongly damaged by FIB. A similar behavior is observed, e.g., at  $T > T_c$  in Fig. 6.1(a). In this situation, it is unclear whether the resistive branches is influenced significantly by the phase diffusion or not. On the other hand, since the energy of the phase particle helped to escape by thermal fluctuations is dissipated through the environment in the phase-diffusion regime, the switching becomes sensitive to the dissipation process. Therefore, the switching statistics could provide unambiguous information on the role of dissipation, which is not provided by the resistive branch below  $I_{SW}$  at  $T < 4.2$  K in our sample.

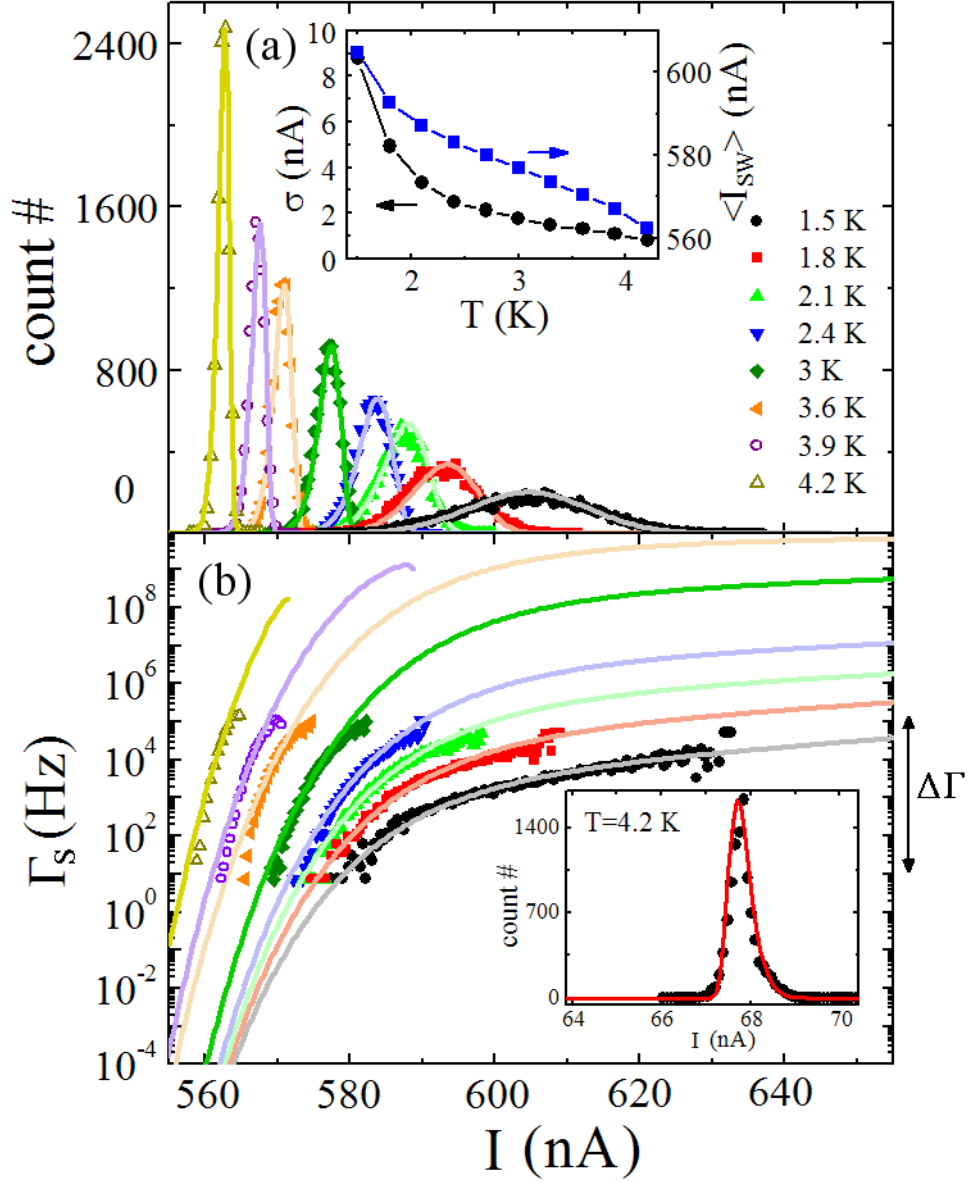


Figure 6.2: The SWCD and (b) the corresponding  $\Gamma_S$  at various  $T$  from 1.5 K to 4.2 K. The solid lines are calculated based on the multiple-retrapping model. Inset of (a) Temperature dependence of the standard deviation ( $\sigma$ ) and the mean switching current ( $\langle I_{SW} \rangle$ ).  $\Delta\Gamma$  is the range of the observable switching rate for a given  $\dot{I}_b$ . Inset of (b) the retrapping current distribution (solid circles) and the calculated behavior (solid line) at  $T = 4.2$  K.

Now, we turn to the switching event from the resistive branch for bias current below  $I_{SW}$  to the QTB. Fig. 6.2(a) shows the SWCD (scattered symbols) at various temperatures. All the observed SWCD's are almost symmetric, which is in contrast to an asymmetric distributions as predicted for the thermally activated escape [? ]. The standard deviation ( $\sigma$ ) and the mean switching currents ( $\langle I_{SW} \rangle$ ) are shown as a function of temperature in the inset of Fig. 6.2(a). The temperature dependence of  $\sigma$  contradicts that of a conventional underdamped JJ, where  $\sigma$  increases with temperature in a thermal-activation regime [55]. Furthermore,  $\sigma(T)$  shows a saturation behavior with increasing temperature. Fig. 6.2(b) shows the switching rate,  $\Gamma_S$  (scattered points) vs  $I$  calculated from the SWCD of Fig. 6.2(a) following the Fulton and Dunkleberger analysis [55]. With lowering temperature,  $\Gamma_S(I)$  shows a *pronounced change from an almost linear to a nonlinear behavior with negative curvature in bias-current dependence in a semi-logarithmic plot*. The same trend in  $\sigma(T)$  has been observed in an IJJ of the same Bi-2212 material near  $T_c$  [63]. In that case,  $I_{SW}$  was almost equal to  $I_r$  and it was assumed that the retrapping process from the QTB to the supercurrent branch affects the switching events. In our case, however, it does not appear plausible that the retrapping process directly affects the switching event, because  $I_{SW}$  and  $I_r$  are far from each other, for example,  $I_{SW} \sim 600$  nA and  $I_r \sim 60$  nA at  $T = 1.8$  K [inset of Fig. 6.1(a)].

To explain this behavior in the switching rate, we adopted the multiple-retrapping model developed in Ref. [65] including effects of junction impedance and temperature. In a phase-diffusion regime, the successive retrapping processes suppress the switching rate,  $\Gamma_S$ . The switching to the high-voltage branch (i.e. the QTB) occurs only when the phase particle is not retrapped after escaping from a local potential minimum. A phase particle escaped from a potential minimum has a probability,  $P_{RT}$ , to be retrapped in the next potential minimum. The switching rate  $\Gamma_S$ , including  $P_{RT}$ , is expressed by [65]

$$\Gamma_S = \Gamma_{TA}(1 - P_{RT}) \frac{\ln(1 - P_{RT})^{-1}}{P_{RT}}. \quad (6.1)$$

Here,  $\Gamma_{TA} = \frac{\omega_p}{2\pi} \exp(-\frac{\Delta U}{k_B T})$  is the thermally activated escape rate,  $\omega_p = \omega_{p0}(1-\gamma^2)^{1/4}$ ,  $\omega_{p0} = (2eI_c/\hbar C)^{1/2}$ ,  $\Delta U(\phi) = 2E_J((1-\gamma^2)^{1/2} - \gamma \arccos \gamma)$  is the escape energy barrier, and  $\gamma [= I/I_c]$  is a normalized bias current. The retrapping probability can be obtained by an integration (see Ref. [72]) of the retrapping rate

$$\Gamma_{RT} = \frac{1}{Z_J C} (\Delta U_{RT}/\pi k_B T)^{1/2} \exp(-\Delta U_{RT}/k_B T) \quad (6.2)$$

where  $\Delta U_{RT}(I) = Z_J^2 C (I - I_{r0})^2$  and  $I_{r0}$  is the noise-free return current from a QTB to a PDB [73]. Here,  $Z_J$  is the fitting parameter representing the total shunt impedance.

Fig. 6.3(a) shows an experimental switching distribution from Fig. 6.2(a) (red dots) at  $T = 1.5$  K with the corresponding fit (blue curve) obtained by using Eq. 6.1 with the best-fit parameters of  $Z_J = 61.9 \Omega$ ,  $I_c = 1.26 \mu\text{A}$ , and  $I_{r0} = 63$  nA. The junction capacitance, 330 fF, was estimated from the typical value of 45 fF/ $\mu\text{m}^2$  for Bi-2212 IJJ's. The corresponding switching rate (red dots) and the fit (blue curve) are shown in Fig. 6.3(b), with the same parameters. An excellent agreement is obtained in both fittings.

These results are analyzed in terms of  $Z_J$ - and  $T$ -dependence of  $P_{RT}$ . The inset of Fig. 6.3(a) shows the calculated  $P_{RT}$  vs  $I$  curves for various  $Z_J$  at  $T = 1.5$  K, with the values of  $I_c$  and  $I_{r0}$  obtained from the best fits shown in Fig. 6.3. The retrapping-probability curve shifts to higher currents as  $Z_J$  decreases, due to the  $Z_J$  dependence of  $\Delta U_{RT}$  in the exponential factor of  $\Gamma_{RT}$ . The bias-current positions of almost vanishing  $P_{RT}$ , indicated by downward arrows, approximately correspond to the maximum current allowing the retrapping. We denote this current as  $I_{PD}$ . Physically this is the same current as the one denoted  $I_m$  in Ref. [66]. The system can hardly be retrapped at a current higher than  $I_{PD}$ , because in this case the energy fed to the system by the bias current gets larger than the dissipated energy. By equating the energy fed and the energy dissipated, similar to McCumber and Stewart

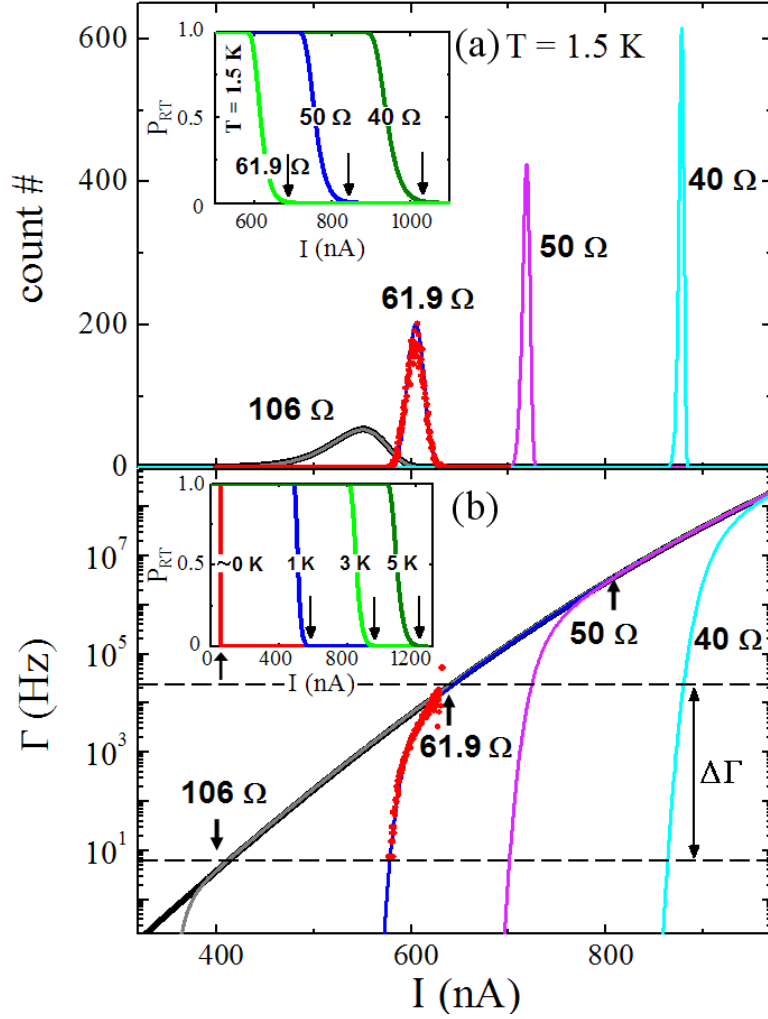


Figure 6.3: (a) The solid lines represent the calculated SWCD's for various  $Z_J$  values of 106  $\Omega$ , 61.9  $\Omega$ , 50  $\Omega$ , and 40  $\Omega$ , corresponding to  $Q_{PD} = 3.88$ , 2.37, 1.90 and 1.55, respectively. Red dots show the SWCD at  $T = 1.5$  K. Inset: Theoretical retrapping probabilities versus bias current, for various  $Z_J$  values at  $T = 1.5$  K. The downward arrows indicate the  $I_{PD}$  values. (b) Estimated switching rate versus the bias current. Red dots correspond to the experimental switching rate for  $T = 1.5$  K. Estimated  $\Gamma_S$  for various  $Z_J$  values in Eq. 6.1 are shown as solid lines. Inset: Estimated retrapping probabilities versus bias current with  $Z_J = 61.9$   $\Omega$  at various  $T$ . Thick black curves in (a) and (b) show the thermally activated SWCD and the corresponding escape rate, respectively, without multiple retrapping processes.

analysis [66, 62], one obtains the relation

$$I_{PD} = 4I_c/\pi Q_{PD}, \quad (6.3)$$

where  $Q_{PD}$  is the phase-diffusion quality factor at  $\omega \sim \omega_p$ . In fact, the noise-free retrapping

current can be written in a form similar to Eq. 6.3, namely as  $I_{r0} = 4I_c/\pi Q(\omega = 0)$  [30]. The thick black curves in Figs. 6.3(a) and 6.3(b) show theoretical SWCD and the corresponding  $\Gamma_{TA}(I)$ , respectively, predicted by the thermal activation model. Other solid curves in Fig. 6.3(b) are  $\Gamma_S(I)$  (Eq. 6.1) for varying  $Z_J$  under the multiple retrapping processes.  $\Gamma_S(I)$  with each  $Z_J$  in Fig. 6.3(b) starts to drop quickly from  $\Gamma_{TA}(I)$  at  $I = I_{PD}$ , which are denoted by arrows in the figure. We define  $I_{PD}$  as the bias-current value corresponding to  $P_{RT} = 0.01$ , where  $\Gamma_S(I_{PD})$  is nearly the same as the  $\Gamma_{TA}(I_{PD})$  as shown in Fig. 6.3(b) [65]. The impedance of  $106 \Omega$  gives the same SWCD as thermally activated SWCD without retrapping because  $\Gamma_S(I)$  overlaps with  $\Gamma_{TA}(I)$  in the observable switching rate window,  $\Delta\Gamma$  (between the two horizontal dashed lines in Fig. 6.3(b)), although  $Z_J$  is of the order of  $Z_L$ . When  $\Gamma_S(I_{PD})$  start to deviate from the  $\Gamma_{TA}$  in  $\Delta\Gamma$  while  $Z_J$  keeps decreasing, the retrapping phenomenon, which is due to the high-frequency dissipation, begins to influence the SCDW. The observable window of  $\Delta\Gamma$  for a fixed  $\dot{I}$  shifts to the steeper section with decreasing  $Z_J$  or increasing  $I_{PD}$ . This gives a decrease of the SWCD width at a constant temperature (Fig. 6.3(a)). We also note that as  $Z_J$  becomes smaller,  $I_{PD}$  becomes larger and correspondingly, according to Eq. 6.3,  $Q_{PD}$  becomes smaller. Thus, we conclude that the distribution width becomes smaller if the quality factor is reduced.

Since  $I_{PD}$  is also affected by temperature, the shape of  $\Gamma_S(I)$  also depends on temperature. The inset of Fig. 6.3(b) illustrates  $P_{RT}$  vs  $I$  at various temperatures. Here,  $Z_J$  is fixed at  $61.9 \Omega$  and other parameters, except for  $T$ , are set to be the same as for the inset of Fig. 6.3(a). The bias-current position of the zero-temperature curve, indicated by an upward arrow in the inset of Fig. 6.3(b), corresponds to the fluctuation-free return current  $I_{r0}$ . The value of  $I_{PD}$  shown by arrows increases with increasing temperature. Thus, in effect, the retrapping probability curve shifts to higher currents as temperature is raised as shown in the inset of Fig. 6.3(b), due to the presence of a Boltzmann-type exponential factor in the expression of  $\Gamma_{RT}$ . To explain the observed SWCD and the corresponding switching rate at different temperatures, therefore, one should consider both effects of the junction shunt

impedance and the temperature on the switching events.

Fig. 6.2 illustrates the calculated SWCD and  $\Gamma_S(I)$  as solid curves at various temperatures with the best-fit parameters listed in Table 6.1. The fitting curves agree well with the data. Here, since temperature is already fixed at the independently measured bath temperature, the main fit-parameter becomes  $Z_J$  as in Figure 6.3(a). As shown in Fig. 6.2(b), with increasing temperature, the calculated  $\Gamma_S(I)$  in the window of  $\Delta\Gamma$  shows steeper regions at higher temperature, which explain the observation of narrower distributions at higher temperatures. Table 6.1 shows that the ratio of  $I_c$  and  $I_{PD}$  becomes smaller with increasing temperature. This behavior leads to the conclusion that  $Q_{PD}$  decreases with increasing temperature following Eq. (2) despite the increase of  $Z_J$  with temperature. This is due to the fact that  $Q_{PD}$  depends on the  $I_c$ , which is decreased with increasing temperature.  $I_{PD}$  even equals to  $I_c$  at  $T = 4.2$  K. This situation is physically the same to an overdamped junction, where  $I_c$  is equal to  $I_{r0}$ . The slope of the calculated  $\Gamma_S(I)$  in the window of  $\Delta\Gamma$  at  $T > 4.2$  K is weakly sensitive to temperature variations. This causes the apparent saturation of  $\sigma$  with increasing temperature near  $T = 4.2$  K (the inset of Fig. 6.2(a)). It should be noticed that, at  $T > 4.2$  K, the thermal activation causes the escape of the phase particle at the rate of  $\sim 10^7$  Hz for a near-zero bias current. According to the purely thermal-activation model the junction is supposed to be in the phase-run-away state even for zero bias current for this temperature region. The multiple retrapping process, however, prevents this situation and makes the junction remain in the superconducting state for  $I < I_c$ , accompanied by the PDB as shown in Fig. 6.2(b). Thermal activation model shows that this strong phase diffusion regime exists down to  $T \sim 3$  K. Therefore, we believe that the resistance of the resistive branch below  $I_{SW}$  in this temperature region of the inset of Fig. 6.1(b) is partially due to the phase diffusion with multiple retrapping processes.

Finally, we comment on the retrapping dynamics from the QTB to the PDB while reducing the bias-current in the quasiparticle tunneling branch. It is well known that the zero-frequency dissipation plays a significant role in this retrapping process [66]. To explore

$T(\text{K})$	$I_c(\mu\text{A})$	$I_{r0}(\text{nA})$	$Z_J(\Omega)$	$I_{PD}(\text{nA})$	$Q_{PD}$
1.5	1.263	63.00	61.9	678	2.37
2.4	1.209	65.10	77.6	683	2.25
3.0	1.006	63.44	86.0	685	1.87
3.6	0.735	65.22	94.7	682	1.37
4.2	0.572	63.79	101.5	572	1.27

Table 6.1: Fitting parameters for the switching events for selected temperatures

this zero-frequency damping effect on this system, we obtained the retrapping current distribution from the QTB-PDB switching at  $T = 4.2$  K. The inset of Fig. 6.1(b) shows the stochastic nature of the retrapping current as shown by solid circles at  $T = 4.2$  K. The shape of the current distribution shows an asymmetry, *i.e.*, the current region lower than the mean value gives sharper distribution because the noise-free  $I_{r0}$  is a lower bound for the distribution. [64]. The calculated retrapping distribution (solid line) by the retrapping rate,  $\Gamma_{RT}$ , is consistent with the experimental result. The best-fit parameters are  $I_{r0} = 63.8$  nA and  $Z_J = 10$  k $\Omega$  ( $\sim R_{qp}$ ), where the estimated noise-free  $I_{r0}$  matches with the value used for  $\Gamma_S$  fitting. The values of  $I_{r0}$  for various temperatures are listed in Table I. The junction shunt impedance  $Z_J$  estimated from the return currents is significantly larger than that found for the switching events. It indicates that the retrapping phenomena from QTB to PDB are mainly determined by a low-frequency limit damping with  $Q(\omega \sim 0) = 11.4$  with  $I_c = 572$  nA and  $I_{r0} = 63.8$  nA at  $T = 4.2$  K as shown in Table 6.1.

## 6.4 Summary

In this report, we study high- $T_c$  IJJ's, which have suppressed critical currents due to FIB treatment. We show that the multiple-retrapping processes in a hysteretic IJJ with a high tunneling resistance govern the switching from a resistive state in phase-diffusion regime into the quasiparticle tunneling state. The predicted SWCD and  $\Gamma_S$  in the multiple-retrapping model are in good agreement with the observed broadening of the distribution of switching

currents with decreasing temperature. We also demonstrate that the change of the shapes of the observed SWCD and  $\Gamma_S$  in various temperatures can be understood by the junction shunt impedance and temperature dependence of the retrapping rate, in terms of junction quality factor in the phase diffusion regime. As the macroscopic quantum tunneling has recently been observed in IJJ's of Bi-2212 single crystals [7], this study provides useful information about the dissipative environment.

# Appendix A

## MQT in high- $T_C$ intrinsic Josephson junctions

In order to verify that we can observe MQT in our  $^3\text{He}$  setup, we measured two high- $T_C$  crystal samples with intrinsic Josephson junctions (IJJ), using the same measurement scheme that was used for the nanowire sample measurements. The general idea in doing this was that the MQT in high- $T_C$  stacked junctions is well known and well understood. By observing the results seen by other groups we hope to gain extra confidence in the correctness of our setup. Indeed, the results obtained in such test confirm that the setup is working properly, as is explained in more details below.

Fig. A.1 shows the standard deviation of the switching current distributions as a function of temperature obtained from the two samples, IJJ1 and IJJ2. The samples were fabricated from  $\text{Bi}_2\text{Sr}_2\text{CaCu}_2\text{O}_{8+x}$  crystal shaped using focused ion beam (FIB) to the lateral dimensions of  $1.6 \times 2.4 \mu\text{m}^2$  (IJJ1). The bias current in these measurements was injected parallel to the  $c$ -axis (i.e., perpendicular to the weakly coupled superconducting planes of the crystal). In Fig. A.1, we observe a crossover from a thermal activated escape regime to MQT regime near  $T^* = 0.65$  K for IJJ1 and near  $T^* = 0.35$  K for IJJ2, which is manifested by a saturation behavior of the standard deviation at lowering temperatures [7]. We also find that, in the high temperature range,  $\sigma$  is proportional to  $T^{2/3}$  which is expected for a thermally activated escape model [6]. To validate this further, we estimated the escape temperature,  $T_{esc}$ , from the escape rates, (obtained from switching current distributions) at different temperatures (see Fig. A.2). For this, we used the usual expression,

$$\Gamma = (\omega_p/2\pi) \exp(-\Delta U/k_B T_{esc}) \quad (\text{A.1})$$

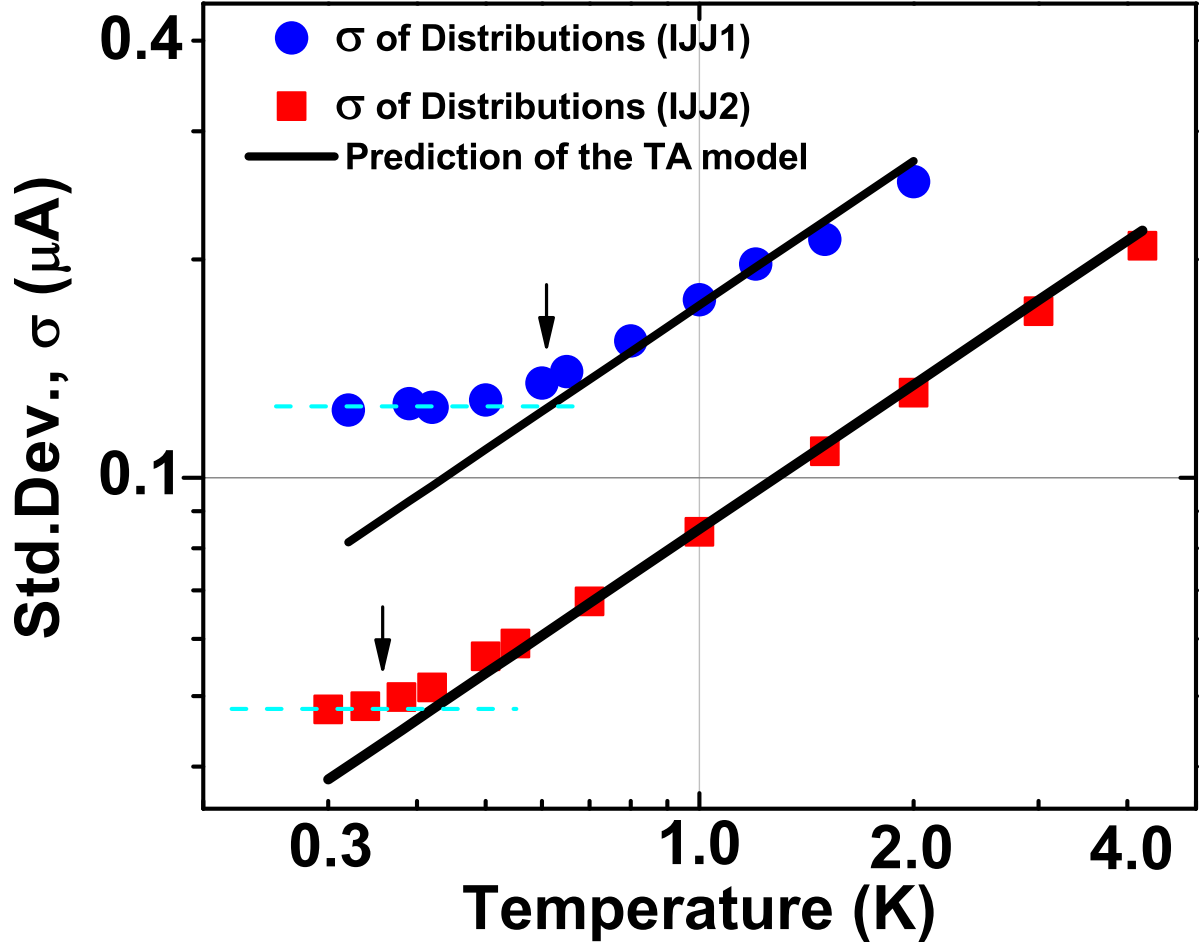


Figure A.1: Standard deviation ( $\sigma$ ) of switching current distributions vs. temperature for two high- $T_c$  crystal with intrinsic Josephson junction samples (IJJ1 and IJJ2), measured in the same  $^3\text{He}$  system in which all the nanowire samples were measured. We clearly see the MQT regime (denoted by the saturation of the distribution width) below a crossover temperature  $T^* = 0.65$  K for IJJ1 and  $T^* = 0.35$  K for IJJ2 (indicated by the two arrows). In the high temperature range, as predicted by the thermal activation model,  $\sigma$  is proportional to  $T^{2/3}$  (solid black line). The fluctuation free critical currents for the samples are  $170.2 \mu\text{A}$  (IJJ1) and  $17.6 \mu\text{A}$  (IJJ2).

where  $\Omega_p$  is the plasma frequency and  $\Delta U = (4\sqrt{2}I_0\Phi_0/6\pi)(1 - I/I_0)^{3/2}$  ( $I_0$  is the fluctuation free critical current) is the barrier energy for the escape of the “phase particle” [5]. The obtained  $T_{esc}$  is plotted versus the bath temperature,  $T_{bath}$  in Fig. A.3. We find that, for, high temperatures,  $T_{esc} = T_{bath}$ , indicating the escape process is dominated by thermal activation. For  $T_{bath} < 0.65$  K,  $T_{esc}$  saturated to a value of 0.73 K, indicating a region where escape process is dominated by MQT [5].

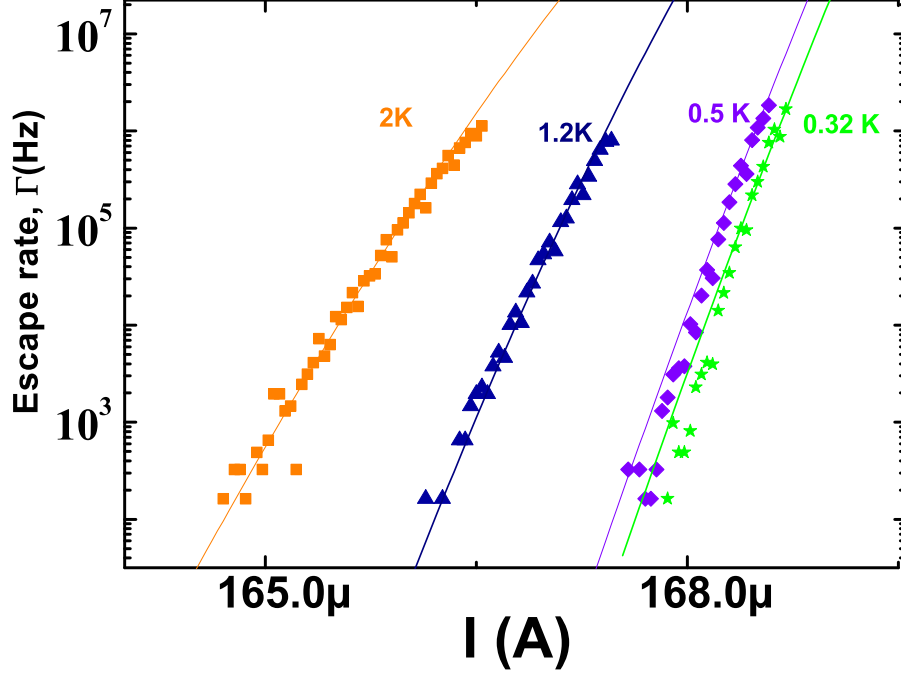


Figure A.2: Switching rates obtained from the switching current distributions (symbols) and the fits obtained (solid lines) using the expression for sample IJJ1 (see text).

Furthermore, to verify that the saturation in  $\sigma$  is not due to noise (i.e., the electronic temperature not decreasing below 0.6 K), we measured another sample (IJJ2) with a critical current  $\sim 10$  times smaller than IJJ1 ( $I_C(0)$  for IJJ1  $\sim 170.2 \mu\text{A}$ ,  $I_C(0)$  for IJJ2  $\sim 17.6 \mu\text{A}$ ). As shown in Fig. S4, the  $\sigma$  follows the prediction of the thermal activation to a lower crossover temperature of  $\sim 0.35$  K, as is expected for a sample with a lower critical current (since the crossover temperature is proportional to  $\sqrt{I_C/C}$  where  $I_C$  is the critical current and  $C$  is the junction capacitance) [7]. Also, for both the samples, the most probable switching current increases with temperature decreasing, indicating that the sample temperature decreases with the bath temperature, down to the lowest attainable temperature (see the inset of Fig. A.3). The observation of crossover temperature (i.e., the observation of MQT) in high- $T_c$  crystals with weakly coupled superconducting planes indicates that the unexpected behavior in  $\sigma(T)$  of a superconducting nanowire is not due to some uncontrolled environmental noise but originates from an intrinsic quantum fluctuations in these samples.

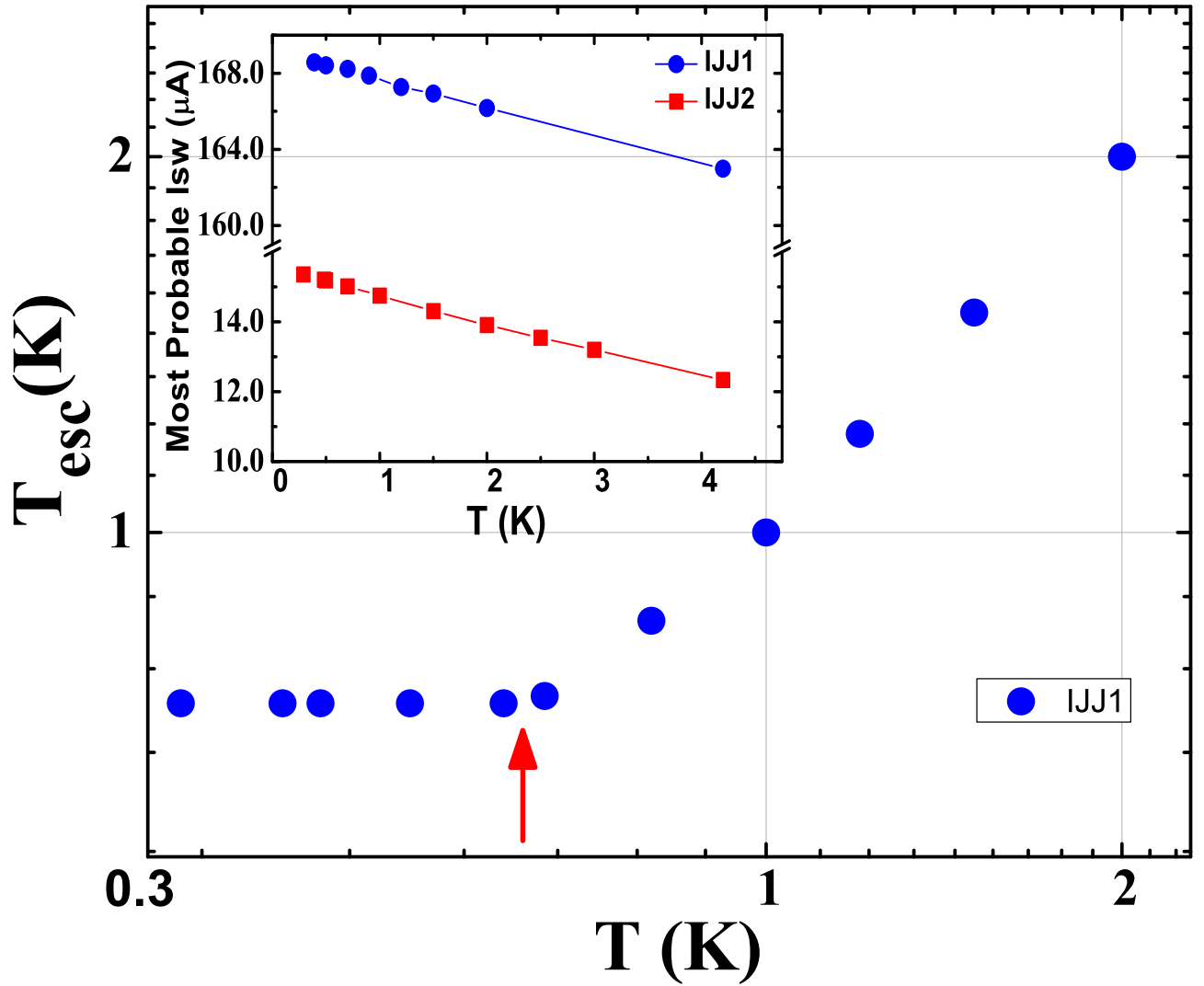


Figure A.3: The escape temperature  $T_{esc}$  obtained at various bath temperatures.  $T_{esc}$  saturates below  $\sim 0.65$  K (indicated by the arrow). The inset shows the most probable switching currents for the two samples obtained from switching current distributions. The critical current for IJJ1 is  $\sim 10$  times larger than IJJ2.

# References

- [1] AO Caldeira and AJ Leggett. Influence of dissipation on quantum tunneling in macroscopic systems. *Physical Review Letters*, 46(4):211–214, 1981.
- [2] A. J. Leggett, S. Chakravarty, A. T. Dorsey, Matthew P. A. Fisher, Anupam Garg, and W. Zwerger. Dynamics of the dissipative two-state system. *Rev. Mod. Phys.*, 59(1):1–85, Jan 1987.
- [3] S. Takagi. *Macroscopic quantum tunneling*. Cambridge University Press, 2002.
- [4] Richard F. Voss and Richard A. Webb. Macroscopic Quantum Tunneling in 1- $\mu$ m Nb Josephson Junctions. *Phys. Rev. Lett.*, 47(4):265–268, Jul 1981.
- [5] J.M. Martinis, M.H. Devoret, and J. Clarke. Experimental tests for the quantum behavior of a macroscopic degree of freedom: The phase difference across a Josephson junction. *Physical Review B*, 35(10):4682–4698, 1987.
- [6] A. Wallraff, A. Lukashenko, J. Lisenfeld, A. Kemp, MV Fistul, Y. Koval, and AV Ustinov. Quantum dynamics of a single vortex. *Nature*, 425(6954):155–158, 2003.
- [7] K. Inomata, S. Sato, K. Nakajima, A. Tanaka, Y. Takano, HB Wang, M. Nagao, H. Hatano, and S. Kawabata. Macroscopic quantum tunneling in a d-wave high-TC Bi2Sr2CaCu2O8+  $\delta$  superconductor. *Phys Rev Lett*, 95(10):107005, 2005.
- [8] W. Wernsdorfer, EB Orozco, K. Hasselbach, A. Benoit, D. Mailly, O. Kubo, H. Nakano, and B. Barbara. Macroscopic quantum tunneling of magnetization of single ferrimagnetic nanoparticles of barium ferrite. *Physical Review Letters*, 79(20):4014–4017, 1997.
- [9] JE Mooij and C. Harmans. Phase-slip flux qubits. *New Journal of Physics*, 7(1):219, 2005.
- [10] N. Giordano and E. R. Schuler. Macroscopic quantum tunneling and related effects in a one-dimensional superconductor. *Phys. Rev. Lett.*, 63(21):2417–2420, Nov 1989.
- [11] W.A. Little. Decay of persistent currents in small superconductors. *Physical Review*, 156(2):396–403, 1967.
- [12] JE Mooij and Y.V. Nazarov. Superconducting nanowires as quantum phase-slip junctions. *Nature Physics*, 2(3):169–172, 2006.

- [13] A. Bezryadin, C. N. Lau, and M. Tinkham. Quantum suppression of superconductivity in ultrathin nanowires. *Nature (London)*, 404:971, 2000.
- [14] AT Bollinger, RC Dinsmore III, A. Rogachev, and A. Bezryadin. Determination of the Superconductor-Insulator Phase Diagram for One-Dimensional Wires. *Physical Review Letters*, 9(1):227003, 2008.
- [15] A.D. Zaikin, D.S. Golubev, A. van Otterlo, and G.T. Zimanyi. Quantum phase slips and transport in ultrathin superconducting wires. *Physical Review Letters*, 78(8):1552–1555, 1997.
- [16] D. Meidan, Y. Oreg, G. Refael, and R.A. Smith. Sharp superconductor–insulator transition in short wires. *Physical Review Letters*, 98(18):187001, 2007.
- [17] S. Khlebnikov and L.P. Pryadko. Quantum phase slips in the presence of finite-range disorder. *Physical review letters*, 95(10):107007, 2005.
- [18] C. N. Lau, N. Markovic, M. Bockrath, A. Bezryadin, and M. Tinkham. Quantum phase slips in superconducting nanowires. *Phys. Rev. Lett.*, 87(21):217003, Nov 2001.
- [19] A. Rogachev and A. Bezryadin. Superconducting properties of polycrystalline Nb nanowires templated by carbon nanotubes. *Applied Physics Letters*, 83:512, 2003.
- [20] AT Bollinger, A. Rogachev, and A. Bezryadin. Dichotomy in short superconducting nanowires: Thermal phase slippage vs. Coulomb blockade. *Europhysics Letters*, 76(3):505–511, 2006.
- [21] A. Rogachev, AT Bollinger, and A. Bezryadin. Influence of High Magnetic Fields on the Superconducting Transition of One-Dimensional Nb and MoGe Nanowires. *Physical Review Letters*, 94(1):17004, 2005.
- [22] M. Sahu, M.H. Bae, A. Rogachev, D. Pekker, T.C. Wei, N. Shah, P.M. Goldbart, and A. Bezryadin. Probing individual topological tunnelling events of a quantum field via their macroscopic consequences . *Arxiv preprint arXiv:0804.2251v2*, 2008.
- [23] N. Shah, D. Pekker, and P.M. Goldbart. Inherent Stochasticity of Superconductor-Resistor Switching Behavior in Nanowires. *Physical Review Letters*, 101:207001, 2007.
- [24] M. Tinkham, J. U. Free, C. N. Lau, and N. Markovic. Hysteretic  $i - v$  curves of superconducting nanowires. *Phys. Rev. B*, 68.
- [25] J.S. Langer and V. Ambegaokar. Intrinsic resistive transition in narrow superconducting channels. *Physical Review*, 164(2):498–510, 1967.
- [26] DE McCumber and BI Halperin. Time scale of intrinsic resistive fluctuations in thin superconducting wires. *Physical Review B*, 1(3):1054–1070, 1970.
- [27] WA Little. Possibility of synthesizing an organic superconductor. *Phys. Rev.*, 134:1416–1424, 1964.

- [28] A. Bezryadin. Quantum suppression of superconductivity in nanowires. *JOURNAL OF PHYSICS CONDENSED MATTER*, 20(4):43202, 2008.
- [29] AT Bollinger. PhD thesis, University of Illinois at Urbana-Champaign, 2005.
- [30] M. Tinkham. *Introduction to superconductivity*. Courier Dover Publications, 2004.
- [31] PG Gennes. Superconductivity of metals and alloys. 1966, 274 P. W. A. BENJAMIN, INC., NEW YORK, N. Y, 1966.
- [32] JE Lukens, RJ Warburton, and WW Webb. Onset of quantized thermal fluctuations in one-dimensional superconductors. *Phys Rev Lett*, 25(17):1180–1184, 1970.
- [33] RS Newbower, MR Beasley, and M. Tinkham. Fluctuation effects on the superconducting transition of tin whisker crystals. *Physical Review B*, 5(3):864–868, 1972.
- [34] Sang L. Chu, A. T. Bollinger, and A. Bezryadin. Phase slips in superconducting films with constrictions. *Phys. Rev. B*, 70(21):214506, Dec 2004.
- [35] N. Giordano. Evidence for Macroscopic Quantum Tunneling in One-Dimensional Superconductors. *Physical Review Letters*, 61(18):2137–2140, 1988.
- [36] CN Lau, N. Markovic, M. Bockrath, A. Bezryadin, and M. Tinkham. Quantum Phase Slips in Superconducting Nanowires. *Physical Review Letters*, 87(21):217003, 2001.
- [37] Dmitri S. Golubev and Andrei D. Zaikin. Quantum tunneling of the order parameter in superconducting nanowires. *Phys. Rev. B*, 64(1):014504, Jun 2001.
- [38] M. Zgirski, KP Riikonen, V. Touboltsev, and K.Y. Arutyunov. Quantum fluctuations in ultranarrow superconducting aluminum nanowires. *Physical Review B*, 77(5), 2008.
- [39] Maciek Zgirski, Karri-Pekka Riikonen, Vladimir Touboltsev, and Konstantin Arutyunov. Size dependent breakdown of superconductivity in ultranarrow nanowires. *Nano Letters*, 5(6):1029–1033, 2005.
- [40] F. Altomare, A.M. Chang, M.R. Melloch, Y. Hong, and C.W. Tu. Evidence for macroscopic quantum tunneling of phase slips in long one-dimensional superconducting Al wires. *Physical Review Letters*, 97(1):17001, 2006.
- [41] F. Sharifi, AV Herzog, and RC Dynes. Crossover from two to one dimension in in situ grown wires of Pb. *Physical Review Letters*, 71(3):428–431, 1993.
- [42] D.S. Hopkins, D. Pekker, P.M. Goldbart, and A. Bezryadin. Quantum Interference Device Made by DNA Templating of Superconducting Nanowires, 2005.
- [43] AT Bollinger, A. Rogachev, M. Remeika, and A. Bezryadin. Effect of morphology on the superconductor-insulator transition in one-dimensional nanowires. *Physical Review B*, 69(18):180503, 2004.

- [44] KF Kelly, IW Chiang, ET Mickelson, RH Hauge, JL Margrave, X. Wang, GE Scuseria, C. Radloff, and NJ Halas. Insight into the mechanism of sidewall functionalization of single-walled nanotubes: an STM study. *Chemical Physics Letters*, 313(3-4):445–450, 1999.
- [45] D.S. Hopkins, D. Pekker, T.C. Wei, P.M. Goldbart, and A. Bezryadin. Local superfluid densities probed via current-induced superconducting phase gradients. *Physical Review B*, 76(22):220506, 2007.
- [46] A. Johansson, G. Sambandamurthy, D. Shahar, N. Jacobson, and R. Tenne. Nanowire Acting as a Superconducting Quantum Interference Device. *Physical Review Letters*, 95(11):116805, 2005.
- [47] Y. Zhang and H. Dai. Formation of metal nanowires on suspended single-walled carbon nanotubes. *Applied Physics Letters*, 77:3015, 2000.
- [48] ET Mickelson, CB Huffman, AG Rinzler, RE Smalley, RH Hauge, and JL Margrave. Fluorination of single-wall carbon nanotubes. *Chemical Physics Letters*, 296(1-2):188–194, 1998.
- [49] A. Rogachev, T.C. Wei, D. Pekker, AT Bollinger, PM Goldbart, and A. Bezryadin. Magnetic-Field Enhancement of Superconductivity in Ultranarrow Wires. *Physical Review Letters*, 97(13):137001, 2006.
- [50] JM Graybeal and MR Beasley. Localization and interaction effects in ultrathin amorphous superconducting films. *Physical Review B*, 29(7):4167–4169, 1984.
- [51] JM Graybeal. PhD thesis, Stanford University, 1985.
- [52] UC Coskun. PhD thesis, University of Illinois at Urbana-Champaign, 2005.
- [53] B. Mühlischlegel. Die thermodynamischen funktionen des supraleiters. *Zeitschrift für Physik A Hadrons and Nuclei*, 155(3):313–327, 1959.
- [54] W.J. Skocpol, M.R. Beasley, and M. Tinkham. Self-heating hotspots in superconducting thin-film microbridges. *Journal of Applied*, 45:4054, 1974.
- [55] T. A. Fulton and L. N. Dunkleberger. Lifetime of the zero-voltage state in josephson tunnel junctions. *Phys. Rev. B*, 9(11):4760–4768, Jun 1974.
- [56] KK Likharev. Superconducting weak links. *Reviews of Modern Physics*, 51(1):101–161, 1979.
- [57] J. Bardeen. Critical fields and currents in superconductors. *Reviews of Modern Physics*, 34(4):667–681, 1962.
- [58] M. Tinkham and CN Lau. Quantum limit to phase coherence in thin superconducting wires. *Applied Physics Letters*, 80:2946, 2002.

- [59] NB Kopnin. *Theory of nonequilibrium superconductivity*. Oxford University Press, 2001.
- [60] P. Hanggi, P. Talkner, and M. Borkovec. Reaction rate theory: fifty years after Kramers *Rev. Mod. Phys*, 62:251–342, 1990.
- [61] D. Vion, M. Götz, P. Joyez, D. Esteve, and M. H. Devoret. Thermal activation above a dissipation barrier: Switching of a small josephson junction. *Phys. Rev. Lett.*, 77(16):3435–3438, Oct 1996.
- [62] JM Kivioja, TE Nieminen, J. Claudon, O. Buisson, FW Hekking, and JP Pekola. Observation of transition from escape dynamics to underdamped phase diffusion in a Josephson junction. *Physical Review Letters*, 94(24):247002, 2005.
- [63] V. M. Krasnov, T. Bauch, S. Intiso, E. Hürfeld, T. Akazaki, H. Takayanagi, and P. Delsing. Collapse of thermal activation in moderately damped josephson junctions. *Phys. Rev. Lett.*, 95(15):157002, Oct 2005.
- [64] JC Fenton and PA Warburton. Monte Carlo simulations of thermal fluctuations in moderately damped Josephson junctions: Multiple escape and retrapping, switching-and return current distributions, and hysteresis. *Physica C Phys Rev B*, 78(462):054526, 2008.
- [65] J. Mannik, S. Li, W. Qiu, W. Chen, V. Patel, S. Han, and JE Lukens. Crossover from Kramers to phase-diffusion switching in moderately damped Josephson junctions (4 pages). *PHYSICAL REVIEW-SERIES B-*, 71(22):220509, 2005.
- [66] John M. Martinis and R. L. Kautz. Classical phase diffusion in small hysteretic josephson junctions. *Phys. Rev. Lett.*, 63(14):1507–1510, Oct 1989.
- [67] A. T. Johnson, C. J. Lobb, and M. Tinkham. Effect of leads and energy gap upon the retrapping current of josephson junctions. *Phys. Rev. Lett.*, 65(10):1263–1266, Sep 1990.
- [68] A. Franz, Y. Koval, D. Vasyukov, P. Müller, H. Schneidewind, D. A. Ryndyk, J. Keller, and C. Helm. Thermal fluctuations in ultrasmall intrinsic josephson junctions. *Phys. Rev. B*, 69(1):014506, Jan 2004.
- [69] P. A. Warburton, A. R. Kuzhakhmetov, G. Burnell, M. G. Blamire, and H. Schneidewind. Decoupling of a current-biased intrinsic josephson junction from its environment. *Phys. Rev. B*, 67(18):184513, May 2003.
- [70] S.J. Kim, Y.I. Latyshev, and T. Yamashita. Submicron stacked-junction fabrication from BiSrCaCuO whiskers by focused-ion-beam etching. *Applied Physics Letters*, 74:1156, 1999.
- [71] N. Kim, Y.J. Doh, H.S. Chang, and H.J. Lee. Suppressed superconductivity of the surface conduction layer in Bi<sub>2</sub>Sr<sub>2</sub>CaCu<sub>2</sub>O<sub>8</sub> single crystals probed by c-axis tunneling measurements. *Phys Rev B*, 59:14639, 1999.

- [72] Anupam Garg. Escape-field distribution for escape from a metastable potential well subject to a steadily increasing bias field. *Phys. Rev. B*, 51(21):15592–15595, Jun 1995.
- [73] E. Ben-Jacob, D. J. Bergman, B. J. Matkowsky, and Z. Schuss. Lifetime of oscillatory steady states. *Phys. Rev. A*, 26(5):2805–2816, Nov 1982.

# Author's Biography

Mitrabhanu Sahu was born on June 7<sup>th</sup> 1980 in Cuttack, India. He graduated from the Indian Institute of Technology, Kharagpur in April of 2003 with a B.Sc. majoring in Physics. He spent the summer of 2002 at the Indian Institute of Science, Bangalore as an intern where he studied surface defect characterization of Si/SiO<sub>2</sub> through wet etching and optical imaging. He was awarded a gold medal as one of the top five physics students in an all India level examination conducted by the India Physics Teachers' Association in 2002.

In the fall of 2003 Mitrabhanu enrolled at the University of Illinois at Urbana-Champaign to begin his doctoral studies. Being always fascinated by low-temperature Physics, and especially nano-devices he joined the group of his advisor, Alexey Bezryadin in January of 2004. In the Bezryadin group, he learned to fabricate superconducting nanowires using single walled carbon nanotubes as templates. He used these wires to study the effects of quantum fluctuations *quasi*-one-dimensional systems. From his measurements of switching current distributions, previously unexplored in nanowires, evidence for quantum phase slips in nanowires was found. Most importantly it was found that at low enough temperatures every quantum phase slip causes switching in the wire from the superconducting state to the resistive state. After completion of his Ph.D, Mitrabhanu will begin his work for Intel Corporation as Process Technology Development Engineer.